Winter 12-15-2019

Contemporary Problems in Aerosol Aggregation and Gelation

Pai Liu
Washington University in St. Louis

WASHINGTON UNIVERSITY IN ST. LOUIS

McKelvey School of Engineering
Department of Energy, Environmental and Chemical Engineering

Dissertation Examination Committee:
Rajan Chakrabarty, Chair
Richard Axelbaum
Pratim Biswas
Milorad Dudukovic
Fangqiong Ling
Christopher Sorensen

Contemporary Problems in Aerosol Aggregation and Gelation

by
Pai Liu

A dissertation presented to
The Graduate School
of Washington University in
partial fulfillment of the
requirements for the degree
of Doctor of Philosophy

December 2019
St. Louis, Missouri

Table of Contents

List of Figures

List of Tables

Acknowledgments

I would like to express my deepest and most sincere gratitude to Dr. Rajan Chakrabarty, my Ph.D. advisor, for taking a chance on me and for helping me develop as a scientist. Dr. Chakrabarty taught me every fundamental facet of research – from designing an experiment to composing a manuscript – when my research career was at the infant stage. As I gradually matured, he provided me a lot of freedom and encouraged me to develop ideas by myself, so that I could gain confidence and eventually become independent. Besides science, Dr. Chakrabarty emphasizes the importance of good communication, and always sets a good example on caring about other people. It was his leadership and personality that have fostered the great atmosphere in our research group, where I spent the most meaningful and productive years of my life.

I am equally grateful to my dissertation committee members for the guidance they have given me throughout my Ph.D. studies. It was from their classroom teaching and seminar talks that I found the spark of interest in scientific research. I would like to especially thank Dr. Pratim Biswas for encouraging me to pursue a Ph.D. degree, and for bringing me into the marvelous world of aerosol science. I am very much thankful to Dr. Christopher Sorensen for teaching me how to approach a problem like a theorist, and for introducing me to the topic of aerosol gelation. I would like to thank Dr. Richard Axelbaum for his teaching on combustion physics, and for helping me understand the distinct phenomenon taking place in the buoyancy-opposed flame. I would like to thank Dr. Milorad Dudukovic for his teaching on kinetics and reaction engineering, and for providing valuable suggestions on my research plans. I would like to thank Dr. Fangqiong Ling for her teaching on data-driven modelling, and for many suggestions on my career development.

Besides my dissertation committee, I also want to thank the people who have helped me tremendously during my stay at Washington University. I thank Dr. William Heinson for his teaching on programming and various numerical methods. The discussion with him has inspired countless creative ideas that were instrumental to many works presented in this dissertation. I thank Ian Arnold for his teaching on various hands-on laboratory basis, from cutting a copper tube to building a flame reactor. Shadowing him allowed me to realize that nothing is very hard once I know how to do it properly. I thank Dr. Yang Wang for his teaching on aerosol instruments. His professionalism and diligence have set a role model for me since my day one in graduate school. I thank the Professors at the Engineering Communication Center for their teaching on technical writing. Especially I would like to thank Professor James Ballard, from whom I have learned so much, not only the subtleties in grammar, but also the words-of-wisdom regarding work and life.

I would like to thank everyone in the Aerosol Impacts and Research Laboratory, current members and alumni. It's been a privilege of mine to work with this group of brilliant and motivated people. I especially thank Dr. Apoorva Pandey, Dr. Yuli Heinson, Benjamin Sumlin, Nishit Shetty, and Chenchong Zhang. Many times, they have saved me from my "tunnel vision" and helped me think out of the box. I would like to thank the faculty and staff in Department of Energy, Environmental and Chemical Engineering (EECE). Especially I would like to thank Ms. Rose Baxter, Ms. Patricia Kofron, Ms. Trisha Sutton, and Ms. Monique Spears for their help ranging from academic events coordinating to equipment purchasing. I thank friends in EECE with whom I have crossed paths.

I would like to thank Dr. Remya Nair at the Nano Research Facility and Dr. Huafang Li at the Institute of Material Science and Engineering for their training on various surface characterization instruments. I would like to thank my statistician friend Kaifeng Xia for sharing his knowledge on math and algorithms.

Finally, I want to give my very special thanks to my parents, Lixin Xu and Hongjun Liu, and many other family members for their unconditional love and tremendous support throughout the past five years. I thank Ms. Wen-Ting Li for putting up with my peculiarities and making me a better person.

Pai Liu

Washington University in St. Louis

December 2019

ABSTRACT OF THE DISSERTATION

Contemporary Problems in Aerosol Aggregation and Gelation

by

Pai Liu

Doctor of Philosophy in Energy, Environmental & Chemical Engineering

Washington University in St. Louis, 2019

Assistant Professor Rajan K. Chakrabarty, Chair

Aggregation of nanoparticles in aerosols is a fundamental phenomenon with important implications to diverse fields ranging from material synthesis to pollutant control. The past few decades have witnessed extensive research on investigating the structure and growth mechanism of aerosol aggregates with sizes spanning across several orders of magnitude. This dissertation focuses on some contemporary problems that remain unaddressed in this topical area. Aerosol aggregates in sub-micron regimes, which are formed via the irreversible collision and aggregation of solid nanoparticle monomers, are fractal-like in their morphology. A mathematical description of this seemingly random structure dates to the seminal works by Forest and Witten (1979). In their work, the aggregate mass and characteristic length were related with a power-law relationship parameterized with a fractal dimension (D_f), which quantifies aggregates' dimensionality, and a prefactor (k_f), which is recently shown to be related to their shape anisotropy. With the advent of mass-based aerosol particle classifiers, aggregates morphology can be alternatively characterized with a power-law relationship connecting their mass and mobility diameter, which is parameterized with a pair of mass-mobility exponent (D_{fm}) and prefactor (k_{fm}). Knowledge of the exact empirical relationships between these pairs of parameters (D_f - D_{fm} and k_f - k_{fm}) is essential for accurate characterization of aggregate physical properties. In this dissertation, comprehensive

empirical relationships were established between these parameters for aggregates produced with a diffusion-limited cluster-cluster aggregation (DLCA) mechanism. The influence of aggregates' shape anisotropy on their mass-mobility relationship was evaluated using the concept of apparent monomer screening.

Prolonged aggregation leads to the phenomenon of gelation at a micrometer level, in which the submicron DLCA aggregates with a characteristic $D_f \approx 1.8$ jam together to form volume spanning gels with a characteristic $D_f \approx 2.5$. These aerosol gel particles, sometimes called superaggregates, have been observed in laboratory-scale diffusion flames, as well as in the naturally occurring large-scale combustions such as wildfires. Toward explaining the morphology and growth mechanism of superaggregates, Sorensen and Chakrabarti (2011) established the theoretical framework of aerosol gelation, which details the dynamic process by which gels are produced from their precursor sols. Part of this dissertation focuses on investigating the kinetics of aerosol gelation with emphasis placed on the previously understudied late-stage regimes in which the mean-field Smoluchowski Equation fails. This late stage kinetics of gelation was probed using a high temporal resolution Monte Carlo DLCA simulation, and system independent kinetic formulations were established along with improved parametrization on the characteristic gelation times.

The morphology and growth mechanism of aerosol gels in the super-micron regime can be largely system dependent and poorly understudied. Part of this dissertation studies the growth of soot gel particles toward millimeter size in a novel buoyancy-opposed flame (BOF) aerosol reactor. Characterizations on the packing density of these particles revealed an inflection in their fractal scaling law within the super-micron regime, parameterized with a decrease of D_f from 2.5 to 1.7. A late-stage growth mechanism, which involves the cluster-cluster aggregation of monomeric gel

particles, was introduced to account for the reappearance of the small D_f values in super-micron regime.

Lastly, our BOF reactor could be harnessed as an enabling technology for scalable production of gel materials. As a proof-of-concept of this technology, we performed flame synthesis of titanium dioxide (TiO_2) aerosol gels using a methane-oxygen BOF reactor with titanium tetraisopropoxide precursor. The in-flame aerosol trapping effect was reproduced in the BOF reactor at a variety of operating conditions. Control of flame temperature was established in the range between c.a. 600 and 1300 °C with the application of nitrogen dilution at variable flow rates. Control of the morphology and crystal phase of the TiO_2 was achieved by exploiting the dependencies of monomer sintering and crystal phase transformation on temperature.

Chapter 1: Introduction

1.1 Fractals

The morphology of aerosol aggregates determines many of their physical and chemical properties. Before mathematician Mandelbrot in 1975 coined the term *fractal* and developed the concept of fractal geometry, the morphology of non-coalescent aerosol aggregates, produced from random collisions between dispersed nanoparticles, is at best described as "fluffy" or "random". Thus, perhaps fractal geometry is one of the most important concepts fundamental to the works presented in this dissertation. Given its importance, the introduction chapter starts out with a brief recap on the concept of fractal geometry and its statistical representations.

1.1.1 Fractal geometry

Fractal-like patterns are almost everywhere in Nature. Trees on campus, broccoli flowers in the markets, rivers branching on landscapes, the coastline of Britain, trajectories of animal foraging, a spark of electric discharge, soot emitted from vehicular exhausts, and last but not least, our brains, which perceive all these incredible shapes. It is counterintuitive to notice that fractal-like objects are more commonly found than the regular ones fitting into the category of Euclidean geometry (Mandelbrot 1977).

Fractal geometry comprises repeating sub-elements and manifests self-similarity over changing length-scale. Statistically, this quality is called scale invariance. For example, in Figure 1.1 we construct a fractal Sierpinski triangle by cloning and arranging equilateral triangles in a recursive manner. The resulting geometry (rightmost, after eight times iteration) is scale invariant. Upon taking a closer look at a subset of the geometry, we immediately notice that the subset looks exactly the same as the whole. Figure 1.2 shows the fractal pattern in Nature through a series of pictures taken on a tree standing on the ground of St. Louis Forest Park in a bleak early spring morning.

Progressively zooming out, we observe scale invariance in the twigs, which look nearly the same as the larger branches, and the larger branches, which in turn look nearly the same as the entire tree.

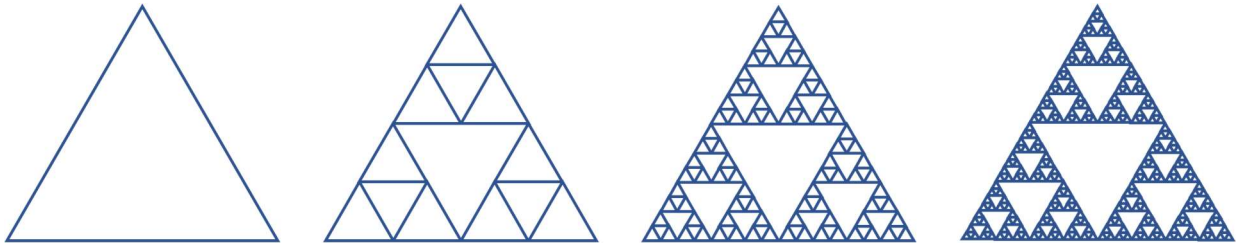

Figure 1.1. Construction of a fractal Sierpinski triangle

Figure 1.2. Scale invariance in a tree.

1.1.2 Scaling law and fractal dimension

Fractal objects can reach a large length-scale without filling much of the space. As Figure 1.3 shows, a Sierpinski triangle reaches the characteristic length of its Euclidean counterpart but filling significantly less amount of space. This space-filling characteristic can be more rigorously discussed using scaling laws, which describe how quantities related to an object will change as a function of its size (West 2017). For example, the scaling relationship between the space (S) that a Euclidean object occupies and its characteristic length (L) can be written as a power law:

$$S \propto L^d \tag{1.1}$$

where the exponent d represents the spatial dimension values of the objects (for example $d = 2$ and 3 for two- and three-dimensional objects, respectively). On the other hand, a fractal object, which fills up a smaller S while attaining the same L, must have a dimensionality taking values smaller than d. Such a dimensionality, which often takes non-integer values, is defined as a fractal dimension (D_f). Therefore, the S taken up by the fractal object, can be described with a power law of L parameterized with D_f, that is:

$$S \propto L^{D_f} \quad \text{with } D_f < d \tag{1.2}$$

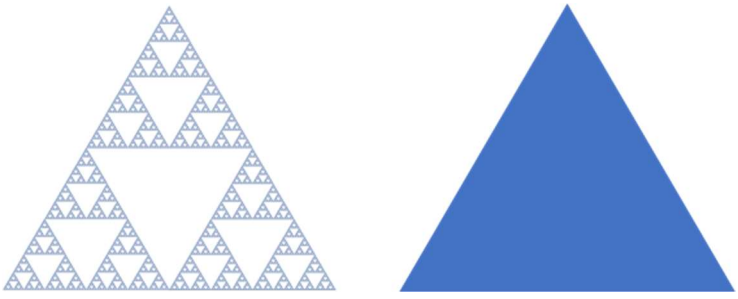

Figure 1.3. A fractal Sierpinski triangle is compared with its Euclidean counterpart having the same characteristic length.

1.2 Aerosol Aggregation

An aerosol aggregation process starts with a dispersion of solid particles (monomers), which are nearly spheres with a radius of several tens of nanometers. When monomers collide, they are assumed to be joined together irreversibly, forming a cluster. Clusters in turn collide with other clusters in the system, forming clusters with bigger sizes, and so forth. When particles grow in such a manner, they are said to be produced via a cluster-cluster aggregation mechanism (Meakin 1985; 1999). Furthermore, if the clusters move in a diffusional manner between their collisions, the process is called diffusion-limited cluster-cluster aggregation (DLCA) (Meakin 1985; 1999). The resulting clusters, if non-coalescent in their nature, are best described with fractal morphology, as shown in Figure 1.4.

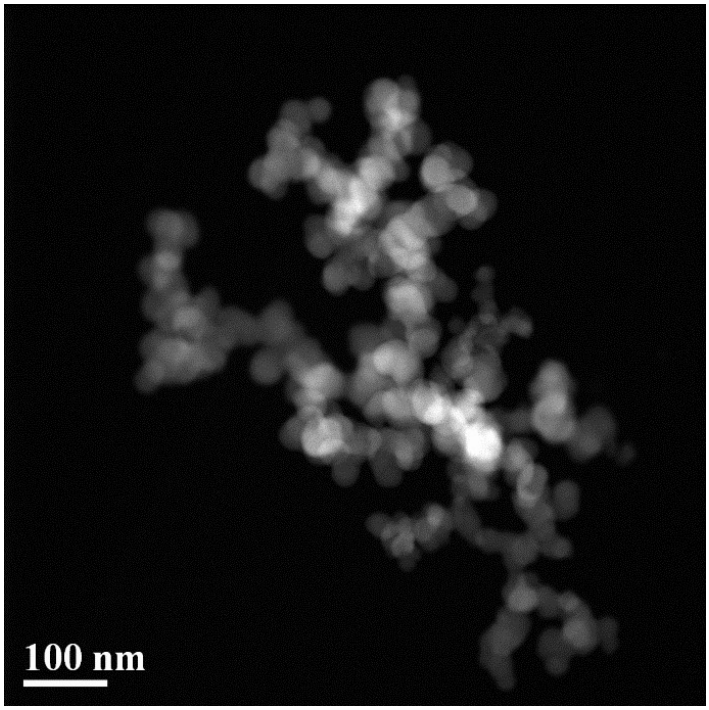

Figure 1.4. Electron microscope image of a soot DLCA aggregate

This section begins with an introduction of the mass scaling law for fractal aggregates, along with the important fractal scaling parameters and their shape descripting roles. The experimental methods for the determination of these scaling parameters are also reviewed. This is immediately followed by a brief discussion on the power-law mass-mobility relationship of aggregates. This section concludes with Smoluchowski Equation and the kinetics of particle growth via a cluster-cluster aggregation mechanism.

1.2.1 Fractal morphology of aerosol aggregates

The mass and characteristic size of fractal aggregates obey a power-law scaling relationship that connects the total number of constituent monomers (N) with aggregate radius of gyration (R_g):

$$N = k_f\left(R_g/a\right)^{D_f} \tag{1.3}$$

where a is the radius of monomers that are commonly assumed to be monodispersed and point-contacting spheres; k_f is a scaling prefactor (Sorensen and Roberts 1997; Sorensen 2001; 2011). For DLCA aggregates, many experiments conducted over the past several decades have led to the consensus that D_f takes a constant value ≈ 1.8 and k_f takes values ranging between 1.0 and 2.5 (Sorensen and Roberts 1997; Sorensen 2001; 2011).

Throughout history D_f has been considered as one of the most important parameters for the aggregate morphology. For example, D_f represents the space filling capability of the aggregates (Mandelbrot 1977; Forrest and Witten 1979). A D_f with a larger value (approaching d) indicates that monomers will be packed in a more compacted manner, and vice versa. The determination of D_f for aggregates dates to the seminal work by Forest and Witten (1979) who first observed the long-range correlations in the morphology of smoke particle aggregates produced from a

combustion process. Experimentally, D_f of aggregates is most commonly determined in an *ex situ* manner, which involves digitalizing and analyzing the electron microscope images of these aggregates (Forest and Witten 1979; Chakrabarty et al. 2011a; McDonald and Biswas 2004). For example, the nested square method (NSM), which counts the monomers in the boundaries drawn with increasing distance to the aggregate geometric center (Xiong and Friedlander 2001; Katrinak et al. 1993), and the perimeter grid method (PGM), which counts the incrementally shrinking lattice boxes that overlap the aggregate perimeter (Dye et al. 2000). Alternatively, analysis can be performed in an ensemble manner on a large number of aggregates, which is called the ensemble method (EM) (Friedlander 2000; Samson et al. 1987; Park et al. 2004). For example, the total number of constituent monomers (N) and the radius of gyration (R_g) are determined for every individual aggregate, and next, D_f can be calculated via a linear regression on $\log N$ and $\log R_g$. Note that the three methods – NSM, PGM, and EM – essentially attempt to extract D_f for aggregates in three-dimensional (3-d) space, from their two-dimensional (2-d) electron microscope images. Bias is unavoidable because of the information loss related to the projection, and empirical correction factors are needed to convert the D_f determined in 2-d images to its 3-d values (Brasil et al. 1999, 2000; Lee and Kramer 2004). Chakrabarty et al. (2011) systematically evaluated the reliability of those three methods through a set of numerical simulation studies. Their results demonstrated that only the EM yields consistent values of D_f from the 2-d projections for aggregates, and hence is the most reliable (Chakrabarty et al. 2011a). This superior reliability of EM is because it accounts for a statistically significant amount of aggregates whose resting angles are uncorrelated. When an ensemble analysis is performed, the influence of projecting angles is averaged out. The *in situ* measurement of D_f can be performed using light-scattering and q-space analysis (Sorensen 2001;

Heinson et al. 2018), which is considered to be an accurate way to directly measure the D_f of aggregates in 3-d space.

The shape descripting role of k_f started to attract increasing awareness in the last decade (Chakrabarty et al. 2009; Heinson et al. 2010; Melas et al. 2014; Goudeli et al. 2016; Heinson et al. 2017). This is because adopting D_f as a sole descriptor of aggregates shape is inadequate. For example, D_f taking a constant value does not address the diversity in aggregate shape anisotropy. Chakrabarty et al. (2009) observed that a minor population of soot produced from a premixed flame have a quasi-one-dimensional shape. Such "stringiness" seems to contradict with the well-recognized constant $D_f \approx 1.8$ for aggregates produced via DLCA mechanism (Chakrabarty et al. 2009). This observation raised two important questions: First, does the D_f of DLCA aggregates have a distribution instead of being a constant? and second, does the shape anisotropy of aggregates control D_f? These questions were answered by Heinson et al. (2010) who systematically studied the fractal scaling of DLCA aggregates that were classified into different bins per their aspect ratio. Their results suggest that DLCA aggregates with a wide range of aspect ratio all have a $D_f \approx 1.8$, and that the shape anistropy of aggregates is in fact related to k_f. A stringier-looking aggregate has a k_f taking a smaller value towards unity, and when k_f is as large as two, the aggregate appears to be more collapsed and isotropic (Heinson et al. 2010). This observation agrees with the math in Eq. (1.3), because an aggregate with a higher degree of anisotropy has a larger R_g, and since N, a, and D_f are fixed, Eq. (1.3) requires a decrease in k_f to balance the increase in R_g (Heinson et al. 2010). More recent studies in this topical area explored other aspects of k_f as a morphology indicator. Melas et al. (2014) related k_f to the distribution of three-monomer angles in DLCA aggregates, and observed a substantial increase in the probability of sharp three-monomer angles when k_f is greater than 1.6. Goudeli et al. (2016) reported a positive correlation between the value

of k_f and the degree of monomer polydispersity. Heinson et al. (2017) quantified the dependence of k_f on the thickness of homogenous coatings applied on the surface of DLCA aggregates.

1.2.2 Mass-mobility relationship of aerosol aggregates

The advent of mass-based aerosol classifiers, such as aerosol particle mass analyzer (APM) and centrifugal particle mass analyzer (CPMA), facilitated an *in situ* method to determine the mass scaling law for aerosol aggregates (McMurry et al. 2002; Park et al. 2004; Scheckman et al. 2009; Cross et al. 2010; Zangmeister et al. 2014). An example is the application of the tandem differential mobility analyzer (DMA) – CPMA – condensational particle counter (CPC) setup. First, an ensemble of aerosol aggregates is passed through the DMA, where the aggregates are classified per their mobility diameter (d_m). These size-selected aggregates are then scanned using the CPMA – CPC and their mass (M) distribution profile is obtained. This technique allows aerosol experimentalists to correlate the M and d_m of aggregates, generating a power-law mass-mobility relationship:

$$M = k_{fm}(d_m/2a)^{D_{fm}} \tag{1.4}$$

where k_{fm} and D_{fm} are respectively called mass-mobility prefactor and exponent (Sorensen 2011). Due to the similarity in the formulation of Eq. (1.3) and (1.4), some experimentalists have wrongly addressed D_{fm} to be the D_f of aggregates. Since d_m is not necessarily related to aggregate R_g in a linear manner, treating these two parameters as interchangeable is not correct. For example, DLCA aggregates with $D_f \approx 1.8$ are shown to have a $D_{fm} \approx 2.2$ (Sorensen 2011). Sorensen (2011) targeted this issue in his review article, however explicit relationships between the two pairs of parameters – D_f and D_{fm}, and k_f and k_{fm} – were yet to be established for DLCA aggregates having variable degree of shape anisotropy.

1.2.3 Kinetics of cluster-cluster aggregation growth

The kinetics of aerosol growth by cluster-cluster aggregation mechanism is described by the Smoluchowski Equation (SE) (Friedlander 2000). The SE which tracks the change in the number density of the aggregates composed of *k* monomers:

$$V\frac{dn_k}{dt} = \frac{1}{2}\sum_{i+j=k} K_{ij} n_i n_j - \sum_{i=1}^{\infty} K_{ik} n_i n_k \tag{1.5}$$

where *V* represents the system volume; *n* represents number of aggregates and the subscripts (*i*, *j*, and *k*) denotes the number of monomers that constitute the aggregates; *K* represents the aggregation kernel measuring the collision efficiency between the two clusters identified by the subscripts; and *t* represents time (Friedlander 2000). Note that SE takes the formulation of Eq. (1.5) when the following important assumptions are satisfied. First, the mean-field assumption requires no spatial correlation between aggregates, so that the probability of cluster *i* meeting cluster *j* is simply proportional to the product of their number densities (Friedlander 2000; Sorensen and Chakrabarti 2011). Second, all collisions between aggregates are assumed to take place in a binary manner, which further guarantees a 100% probability that the colliding particles stick with each other (Friedlander 2000).

The solution to SE with homogeneous *K*, yields the expression for the i^{th} moments (M_i) of cluster size distribution:

$$M_i(t) = M_i(0)\left(1 + \frac{t}{t_c}\right)^{(i-1)z} \tag{1.6}$$

where *z* is a kinetic exponent and t_c is a characteristic time for cluster-cluster aggregation (Sorensen and Chakrabarti 2011; Fry et al. 2002). In the case of DLCA *z* takes a value of one (Sorensen and Chakrabarti 2011; Fry et al. 2002), and correspondingly, the t_c for Brownian aggregation is:

$$t_c = \frac{2V}{Kn_{tot,0}} \tag{1.7}$$

where $n_{tot,0}$ is the number of particles at $t = 0$, which is equal to the conserved total number of monomers in the system (or $M_0(0)$). The Brownian aggregation kernel K is written as follows in Eq. (1.8), invoking the Stokes-Einstein type of diffusion:

$$K = \frac{8k_B T}{3\mu} \tag{1.8}$$

where k_B, T, and μ respectively represent the Boltzmann constant, temperature, and viscosity of the surrounding gas (Friedlander 2000).

1.3 Aerosol Gelation

Prolonged aggregation leads to gelation, a process in which the dispersed fractal aggregates jam together, forming a volume spanning network with a $D_f \approx 2.5$ (Sorensen and Chakrabarti 2011). For a long time, gelation was believed to be a phenomenon only taking place in liquids, for example, the wet sol-gel process (Brinker and Scherer 1990). That changed when Sorensen et al. (1998) observed the formation of soot gel particles in an acetylene flame and introduced the concept of *aerosol gelation*. Figure 1.5 shows the typical size and morphology of aerosol gel produced from flame soot. This section starts with a revisit on the fundamental concepts in the theory of aerosol gelation, along with a review on the important characteristic length and time scales for the gelation in DLCA systems. This is followed by a subsection detailing the flame systems – both in laboratory and in nature – that facilitate aerosol gelation. This section concludes with the application of aerosol gelation to material synthesis.

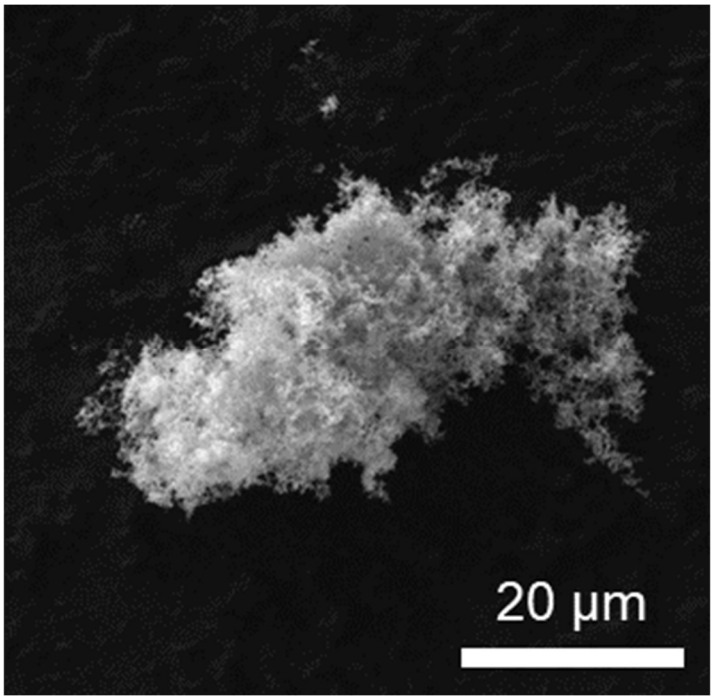

Figure 1.5. Electron microscope image of a soot aerosol gel.

1.3.1 Theoretical foundation

Gelation in sol systems was traditionally described with percolation theory (Stauffer and Aharony 2018). For example, a percolation model (Stauffer 1976; Degennes 1976; Stauffer et al. 1982) operates by filling system space with a point lattice, and then randomly occupying each lattice site with monomers having a diameter equal to the lattice space. Monomers that are placed in adjacent lattice points will be regarded as joined into the same aggregate. If some critical monomer concentration Φ_C is reached, a volume spanning gel with $D_f \approx 2.5$ will emerge. Although percolation model succeeds in describing the emergence of gel, it does not involve any timescale and hence is a static model (Sorensen and Chakrabarti 2011; Heinson et al. 2017).

A dynamic description of gelation accounts for the entire process by which a gel is produced from its precursor sol (Sorensen and Chakrabarti 2011; Heinson et al. 2017). For example, Figure 1.6

shows the evolution a DLCA system starting out with solid monomers (picture on the left), which come together and form fractal aggregates (picture in the middle). If the system is allowed to evolve for a long time, DLCA aggregates eventually jam together, producing gels which have a large-scale connectivity spanning the system (picture on the right). Those gel particles are interchangeably called "superaggregates" to highlight the fact that they are composed by DLCA "supermonomers". The hybrid morphology of superaggregates – with $D_f \approx 2.5$ over large length scales and $D_f \approx 1.8$ over small length scales – has been repeatedly verified in many theoretical and experimental findings (Sorensen and Chakrabarti 2011). The latest study on this topical area shows that gels produced from a DLCA share identical morphologies with those produced from a percolation model (Heinson et al. 2017). Therefore, the dynamic description of gelation is unified with static percolation.

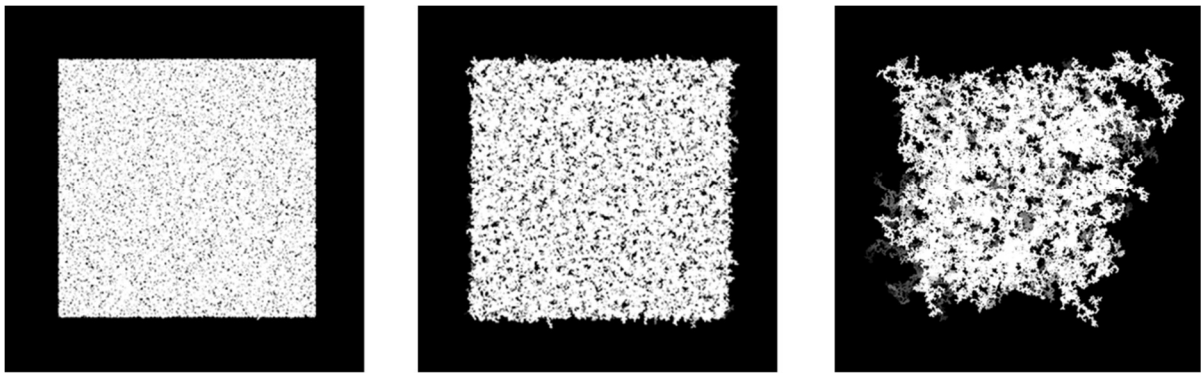

Figure 1.6. From left to right, snapshots taken on a simulated DLCA system with increasing time.

The dynamic description recognizes the tendency of gelation from the simple fact that the D_f of a fractal aggregate is always smaller that the spatial dimension d (Sorensen and Chakrabarti 2011). As a result, free spaces in the system are progressively occupied as aggregates grow until none is left. This system crowding effect can be illustrated with a comparison between two primary length

scales: the average aggregate size $\langle R_g \rangle$ and the average aggregate nearest neighbor separation $\langle R_{nn} \rangle$. The fractal scaling law in Eq. (1.3) provides:

$$\langle R_g \rangle \propto \langle N \rangle^{1/D_f} \tag{1.9}$$

where $\langle N \rangle$ represents the mean aggregate mass (mean number of monomers per aggregates).

The $\langle R_{nn} \rangle$ is related to spatial dimension d by assuming the system space to be uniformly allocated per each aggregate:

$$\langle R_{nn} \rangle \propto (n_{tot}/V)^{-1/d} \tag{1.10}$$

where n_{tot} is the total number of aggregates. Conservation of total number of monomers provides $n_{tot} = n_{tot,0} / \langle N \rangle$, and thus Eq. (1.10) yields to

$$\langle R_{nn} \rangle \propto \langle N \rangle^{1/d} \tag{1.11}$$

Figure 1.7 plots Eq. (1.9) and (1.11) in a log-log space. The system starts out with $\langle R_{nn} \rangle \gg \langle R_g \rangle$, which is called a cluster-dilute condition. As aggregate grow, $\langle R_g \rangle$ always increases faster than $\langle R_{nn} \rangle$ because of $D_f < d$, driving the system to a cluster-dense condition, at which $\langle R_{nn} \rangle / \langle R_g \rangle \approx 10$. These increasing trends ultimately lead to the condition $\langle R_g \rangle \approx \langle R_{nn} \rangle$, defined as an ideal gel point (IGP), at which the sol system is about to gel (Sorensen and Chakrabarti 2011; Kolb et al. 1983; Vicsek 1989). Beyond the IGP, $\langle R_g \rangle$ is greater than $\langle R_{nn} \rangle$ indicating that aggregates start to interdigitate, and the subsequent physical occurrence of gel is called a physical gel point (PGP). At last, when all aggregates in the system are incorporated in a single gel particle, the system is said to reach a final gel stage (FGS) (Sorensen and Chakrabarti 2011).

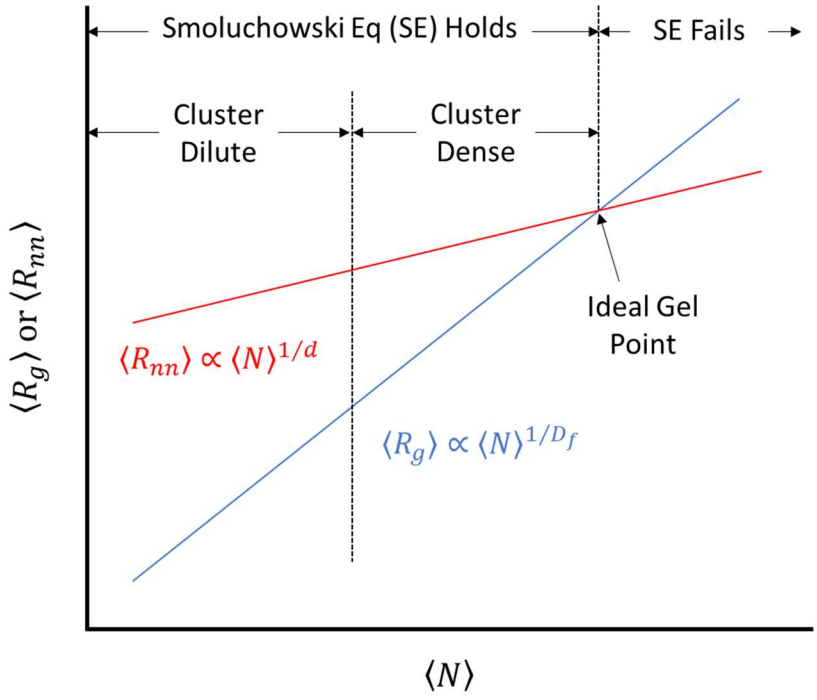

Figure 1.7. (Adapted from Sorensen and Chakrabarti 2011, Soft Matter 7, 2284-2296) Sketch of the evolution of the two primary length scales $<R_g>$ and $<R_{nn}>$ as a function of mean number of monomers per aggregates $<N>$.

The condition $<R_g> \approx <R_{nn}>$ only provides a rough evaluation on the characteristic aggregate size at IGP ($R_{g,IGP}$). An accurate estimation on $R_{g,IGP}$ requires the use of cluster volume fraction (f_{vc}), which is defined as the ratio of volume occupied by aggregates to the system volume. Volume occupied by an aggregate, including both connected monomers and the space between them, is best described using the volume of a sphere with aggregate perimeter radius $R_p = [(D_f + 2)/D_f]^{1/2} R_g$ (Sorensen and Chakrabarti 2011; Fry et al. 2002; Oh and Sorensen 1997). If all aggregates in the system are assumed to maintain same size and isotropic shape, the total f_{vc} can be written as:

$$f_{vc} = \frac{4\pi n_{tot}}{3V} \left(\frac{D_f + 2}{D_f} \right)^{3/2} R_g^3 \tag{1.12}$$

Solving $f_{vc}(R_{g,IGP}) = 1$ with the combination of Eq. (1.12), (1.3) and $n_{tot} = n_{tot,0} / \langle N \rangle$ provides analytical expressions for $R_{g,IGP}$, and the corresponding average aggregate mass (N_{IGP}):

$$R_{g,IGP} = a\left[f_{vm}^{-1} k_f \left(\frac{D_f}{D_f+2}\right)^{3/2}\right]^{1/(3-D_f)} \tag{1.13a}$$

$$N_{IGP} = f_{vm}^{D_f/(D_f-3)} k_f^{3/(3-D_f)} \left(\frac{D_f}{D_f+2}\right)^{3D_f/(6-2D_f)} \tag{1.13b}$$

where f_{vm} represents monomer volume fraction which is a conserved parameter. Its expression can be written as:

$$\text{with } f_{vm} = \frac{4}{3}\pi a^3 \frac{n_{tot,0}}{V} \tag{1.14}$$

Eq. (1.13a) and (1.13b) indicate that a denser aggregation system (higher f_{vm}) reaches IGP with a smaller characteristic aggregates size and mass, which can also be qualitatively observed in Figure 1.7.

The kinetics of gelation should be discussed in two separate regimes according to the IGP (Sorensen and Chakrabarti, 2011). In the pre-IGP regime, the system evolves with mean-field cluster-cluster aggregation mechanism, and the aggregate growth can be described using the solution of SE (discussed in Section 1.2.3). For example, the average aggregate mass $\langle N \rangle = n_{tot} / n_{tot,0}$ can be written in the form of moments, $\langle N(t) \rangle = M_0(t = 0) / M_0(t)$, and Eq. (1.6) with $i = 0$ and $z = 1$ provides:

$$\langle N(t) \rangle = 1 + t/t_c \tag{1.15}$$

Furthermore, combination of Eq. (1.7) and (1.14) provides:

$$t_c = \frac{8\pi}{3} K^{-1} f_{vm}^{-1} a^3 \tag{1.16}$$

These equations lead to the characteristic timescale for a system to reach IGP (t_{IGP}) (Dhaubhadel et al. 2007;). For example, solving $<N(t_{IGP})> = N_{IGP}$ with the combination of Eq. (1.15), (1.16), and (1.13b) provides an analytical expression for t_{IGP}, which reads:

$$t_{IGP} \approx K^{-1} a^3 f_{vm}^{-3/(3-D_f)} \tag{1.17}$$

Eq. (1.17) may in fact overestimate t_{IGP} because it does not account for the enhancement in aggregation kinetics as the system evolves from cluster-dilute to dense conditions (Sorensen and Chakrabarti 2011). Theoretical study by Fry et al. (2002) has identified that the kinetics of aggregation tend to speed up in DLCA system as f_{vc} increases to unity (the IGP). Specifically, when a system starts out in cluster-dilute regime, Brownian aggregation mechanism holds, and the kinetics is parameterized with $z = 1$ (Fry et al. 2002). Subsequently, when cluster-dense condition sets in, aggregates no longer have enough free space to move by a diffusional manner, and the aggregation mechanism becomes ballistic-limited near the IGP (Fry et al. 2002; Sorensen and Chakrabarti 2011). The enhanced kinetics due to this system crowding effect manifests as an increase in z toward a value of two, when the system reaches IGP (Fry et al. 2002; Sorensen and Chakrabarti 2011).

In the post-IGP regime, the mean-field assumption no longer holds valid because aggregates start to interdigitate, and consequentially the SE fails (Sorensen and Chakrabarti 2011). Note that the transition of monomers from sol to gel phase actually takes place in this regime. How to describe the kinetics of the post-IGP regime remains an open research topic. Fry et al. (2002) empirically

mapped the values of z for DLCA starting out with various f_{vm} and observed the increasing trends to persist till FGS at which the terminal value of z is as large as six. Rottereau et al. (2004) modelled the post-IGP regimes using the concept of connectivity among clusters. Purely mathematical based analysis disregarded the breaking-down of mean-field assumption and applied SE in the late-stage post-IGP regime (Van Dongen and Ernst 1985). Such a model has led to the advent of "mathematical gelation", which has been shown to deviate significantly from that occurred in real-world colloid systems (Sandkühler et al. 2004). Lushnikov (2006) described the gelation in coagulating system using a truncated model, in which gel particles with mass greater than a cut-off value were immediately removed. Such a model reconciled the paradoxical behavior of SE at a cost of violating mass conservation. The characteristic timescale for post-IGP regime was yet to be formulated in the traditional theoretical framework. It worth to note that t_{IGP} only marks the starting point of gelation. Another timescale parameter predicting the completeness of gelation is needed so as to provide a comprehensive description of the full transition process.

1.3.2 Aerosol gelation in flames

Spontaneous aerosol gelation was first observed in the sooting layer of a laminar acetylene diffusion flame (Sorensen et al. 1998). Many subsequent works by Sorensen's group have focused on this flame system to understand the growth mechanism of large soot superaggregates (reaching 1mm) which form gel-like networks in the thin layer of the cylindrical annular flame front (Sorensen and Hageman 2001; Sorensen et al. 2003; Kim et al. 2004). Kim et al. (2006) identified four distinct stages in the growth of soot particles from several tens of nanometer to millimeter. The size delimited D_f values were reported to evolve from 1.8 to 2.5, and then from 1.4 to 1.9, revealing a possible 2-d DLCA – gelation (in the size range $1\mu m < R_g < 100\mu m$) to take over the particle growth immediately after the classical 3-d DLCA – gelation (in the size range $R_g < 1\mu m$)

(Kim et al. 2006). This observation indicates that 3-d soot superaggregates with $D_f \approx 2.5$ and $R_g \approx$ 1μm in turn serve as "supermonomers" for a late-stage large-scale cluster-cluster aggregation. Such a large-scale cluster-cluster aggregation (and subsequent gelation) is confined in a 2-d space because the cylindrical annular sooting layer of the acetylene diffusion flame appears thin when compared with the size of these large soot particles (Sorensen and Hageman 2001; Kim et al. 2006).

Another laboratory-scale combustion system facilitating aerosol gelation is buoyancy-opposed flame (BOF) aerosol reactor (reversed gravity or negative gravity flame as termed in Chakrabarty et al. 2012; 2014a). The BOF reactor consists of a Burke-Schumann type two-stage burner, which is operated in a down-fired configuration (Chakrabarty et al. 2012; 2014a). The opposing effects between buoyancy force and the reactor inflow triggers a recirculation in the flame body. Particles trapped in the recirculation attain a sufficiently long residence time and transition to gel phase. More detailed description on the schematic diagram of a BOF reactor is included in section 6.3.1 of Chapter 6. Figure 1.8 shows the operation of an ethylene BOF reactor. Soot particles with a millimeter size are observed in the flame recirculation zone. The flame takes up a non-flickering "U-shape" geometry, preventing the shear-driven fragmentations of the gel particles. Chakrabarty et al. (2014a) performed off-line characterization on the millimeter-sized soot particles produced in an acetylene BOF reactor. Gel-like networks have been observed in configuration of monomers constituting these soot particles. However, the macroscopic morphology and D_f of these particles remained understudied in those preliminary works. More investigation should be directed to understanding the detailed, size-delimited growth mechanism for these particles.

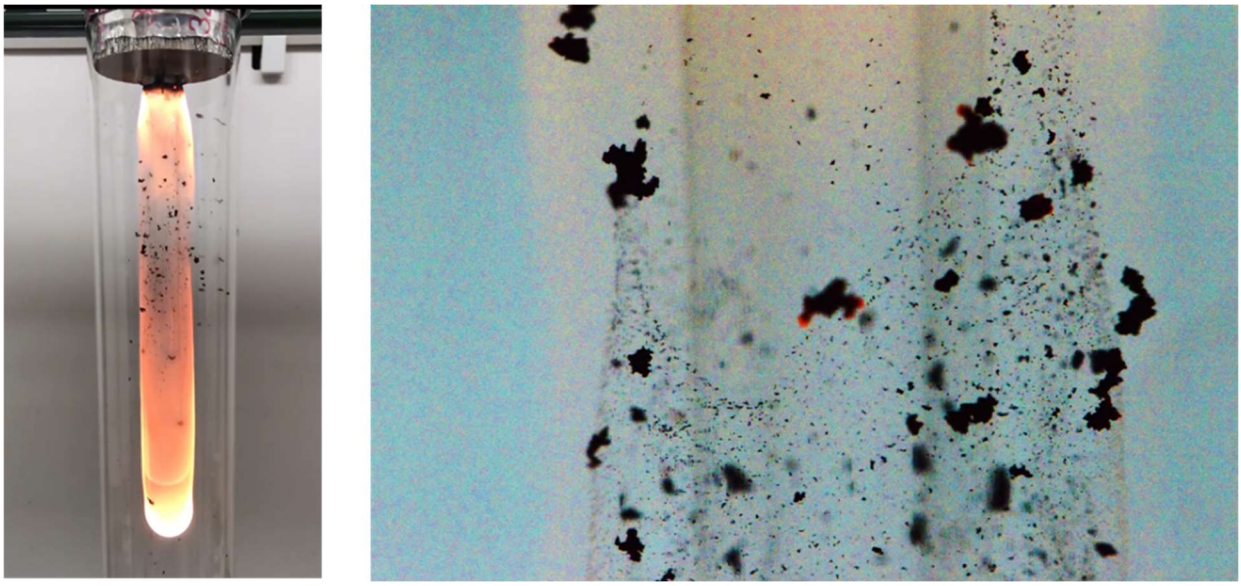

Figure 1.8. Photograph of an ethylene buoyancy-opposed flame (left). Soot particles trapped in the flame recirculation (right).

Aerosol gelation also takes place in large scale combustion in nature, such as wildfires. Field researches have identified soot superaggregates with a $D_f \approx 2.6$ and a super-micron size from the major wildfires in India, Northern California, New Mexico, and Mexico City (Chakrabarty et al. 2014b). The estimated radiative forcing efficiencies of these soot superaggregates have been shown to deviate significantly from that of the freshly emitted DLCA aggregates and the spherical soot particles employed in climate models (Chakrabarty et al. 2014b; Bond et al. 2013; Cappa et al. 2012). The influence of these previously unrecognized pollutant on climate and human health remains an open research topic (Heinson et al. 2016).

1.3.3 Applying aerosol gelation to material synthesis

Aerogels are meso-porous materials with ultra-low density and high surface area, which have a great potential in serving many energy and environmental applications, such as catalyst, water and air purification, space dust catching, and thermal insulations (Brinker and Scherer 2013; Dhaubhadel et al. 2007; Dhaubhadel 2008; Dhaubhadel et al. 2012; Chakrabarty et al. 2014a). Traditionally aerogel materials are synthesized with the liquid phase sol-gel technique, which involves a subsequent super critical point drying process (Brinker and Scherer 2013). Such a two-step process is time-consuming and expensive. The advent of aerosol gelation has opened a new avenue for the synthesis of gel materials in gas-phase, which is a rapid single-step process and cost-effective (Dhaubhadel et al. 2007; Dhaubhadel 2008; Dhaubhadel et al. 2012; Chakrabarty et al. 2014a). The gel materials synthesized via aerosol route, were called *aerosol gel*, so as to be distinguished from the *aerogel* synthesized via liquid phase sol-gel route (Dhaubhadel et al. 2007).

Laboratory synthesis of aerosol gel was first realized in the pioneer work by Dhaubhadel et al. (2007) with the technique of controlled detonation. In their study, precursor of aerosol gel materials (i.e. combustible gases, such as methane and silane) and oxygen are mixed in a closed chamber and subsequently denotated (Dhaubhadel et al. 2007; Dhaubhadel et al. 2012). The explosive reaction produces nanometer-sized monomers which rapidly aggregate and form the gel. Carbon and silica aerosol gels synthesized via controlled detonation were reported to have effective densities as low as 2.5 and 4 mg/cm^3, respectively, and specific surface areas as high as 350 and 500 m^2/g, respectively (Dhaubhadel et al. 2007; Dhaubhadel et al. 2012).

Flame synthesis of aerosol gel can be achieved using a BOF aerosol reactor. Chakrabarty et al. (2014a) demonstrated the synthesis of carbon aerosol gel using an acetylene-oxygen BOF aerosol

reactor. Millimeter-sized carbon aerosol gel particles were reported to have an effective density of about 4.5 mg/cm^3 and a specific surface area of about 208 m^2/g (Chakrabarty et al. 2014a). Figure 1.9 shows the bulk morphology of carbon aerosol gel produced using flame synthesis. Unlike controlled detonation, flame synthesis of aerosol gel with BOF reactor is a continuous process and less hazardous, which opens new possibility for the synthesis of aerosol gel materials on an industrial scale (Chakrabarty et al. 2014a).

The possibility of using BOF reactor to synthesize non-carbonaceous nanoparticles in gel forms was not explored in Chakrabarty's preliminary works. Another open research topic is to establish control on the flame conditions, toward a controlled synthesis of materials with tailorable properties, such as monomer size, crystal phase, and morphology (Jiang et al. 2007; Thimsen and Biswas 2007; Kammler et al. 2001).

Figure 1.9. Carbon aerosol gels produced with a buoyancy-opposed flame aerosol reactor.

1.4 Numerical Methods

This section reviews two numerical methods used in this dissertation: FracMAP and off-lattice diffusion-limited cluster-cluster aggregation model.

1.4.1 FracMAP

FracMAP is a patented computer package designed to simulate fractal aggregates in 3-d space (Chakrabarty et al. 2009). It has been extensively used to establish the empirical relationships between the 3-d and 2-d projected properties of aerosol aggregates (Chakrabarty et al. 2011a; 2011b; Pandey et al. 2015). FracMAP takes a set of user specified fractal parameters $\{D_f, k_f, a, N\}$ as an input and generate aggregate with a Monte Carlo particle-cluster aggregation method. The algorithm starts out with two point-contact monomers, and sequentially attaches new monomers to the aggregates at random position until the designated N is reached. For each random addition of monomer, R_g is calculated from the resulting monomer configuration and compared to what Eq. (1.3) predicts with the designated $\{D_f, k_f, a, N\}$. The monomer configuration that provides the best fit is kept (Chakrabarty et al. 2009). Doing so, FracMAP generates 3-d aggregates precisely according to the input morphological parameters, which may take any arbitrary values within a physically reasonable range. FracMAP is also a static model, in which the monomer addition is not related to any timescale associated in the real-world aerosol systems. Thus, it is not suitable to study the kinetics of aggregate growth.

1.4.2 Off-lattice DLCA model

Off-lattice DLCA is a Monte Carlo model that closely mimics the real-world mechanism producing fractal aggregates via a diffusion-limited cluster-cluster aggregation growth (Meakin 1984; Heinson 2015). The model simulates the dynamics of the entire sol system and takes user

specified inputs such as system volume V, total number of monomers $n_{tot,0}$, and monomer radius a. The algorithm starts out by generating a rectangular box with V, which houses the aggregating sol system. Initially, $n_{tot,0}$ monomers are placed at non-overlapping locations that are randomly chosen in the box. The algorithm proceeds by picking a particle (either cluster or monomer) with a probability that is inversely related to the particle mass N, and the particle that is picked will be moved along a random direction with a constant distance $2a$. Once every n_{tot} particles in the system are picked and moved, time increments a constant interval corresponding to the duration by which monomers move a root-mean-squared-displacement of $2a$. Doing so, the algorithm drives the movements of particles per the Stokes-Einstein type of diffusion (Friedlander 2000; Heinson 2015). During the entire process, if two clusters collide, they will be joined together forming a new cluster. The algorithm iterates untill any user specified time, and aggregates produced in the system are studied for their morphologies in 3-d (Heinson et al. 2010; 2012). The time evolution of aggregate size distribution could also be tracked using the DLCA model, which can be used to study the kinetics of aggregate growth in cluster-dense condition and beyond gel point (Fry et al. 2002; Heinson et al. 2017).

1.5 Contemporary Problems and Dissertation Outline

The following dissertation comprises five self-contained chapters, each of which addresses one contemporary problem in the topical area of aerosol aggregation and gelation. Each chapter is structured with subsections in the following order: *abstract*, *introduction*, *methods*, *results and discussion*, *conclusion*, and the end-of-chapter *references*. A concluding chapter is provided at last, which summarizes the major findings in this dissertation.

Chapter 2 presents a mathematical study on the ballistic-to-diffusive (BD) transition in random walks. The BD transition, which has been ubiquitously observed from the random walkers from various stochastic systems (Pusey 2011; Solomon et al. 1993) and has been shown to influence the aggregation kinetics in DLCA system near the gelling condition (Sorensen and Chakrabarti 2011). In this mathematical study, the BD transition problem was approached with a novel method based on directional statistics. Generic mathematical expressions for the transition kinetics were derived and a method to estimate the full development of diffusion was introduced. This study is presented at the beginning of the dissertation to highlight that an accurate characterization of particle motion is always a prerequisite to study the kinetics of aggregation.

Chapter 3 targets on the cluster-dilute aerosol aggregates with a characteristic length < 1μm. The fractal morphology parameters (D_f and k_f) and mass-mobility parameters (D_{fm} and k_{fm}) had been misused by aerosol experimentalists in an interchangeable manner. This problem was reiterated here with empirical relationships among D_f, k_f, D_{fm}, and k_{fm} established based on computer simulated aggregates of changing shape anisotropy. The influences of aggregate shape on the apparent monomer screening, and therefore on the mass-mobility relationships were discussed.

Chapter 4 targets on the aerosol-to-gel transition occurring at the characteristic length ≈ 1μm. Our understanding on the kinetics of aerosol gelation remained incomplete due to the breaking down of Smoluchowski Equation, when the cluster volume fraction in the system reaches unity (the IGP). Yet the transition of monomers from aerosol phase to gel phase takes place in the post-IGP regime. This kinetic problem was approached with high temporal-resolution Monte Carlo simulations on the irreversible aggregation systems. System-independent power-law relationships were established to describe the transition kinetics in the pre- and post-IGP regimes. A new characteristic timescale parameter predicting the completeness of gelation was introduced.

Chapter 5 targets on the growth aerosol gel particles with a characteristic length > 1μm. Many previous studies (Sorensen and Hageman 2001; Sorensen et al. 2003; Kim et al. 2004; 2006) have exemplified that the growth mechanism of soot in the size range between 1μm and 100μm is highly system dependent. However, the millimeter-sized soot gel particles produced in the BOF aerosol reactor remained understudied, in terms of their macroscopic level fractal morphology and late-stage growth mechanism. This problem was approached with a series of off-line characterizations on the packing density of soot produced in an ethylene-oxygen BOF. The fractal scaling law of packing density was established in a broad range across five-order-of-magnitude length. The late-stage growth mechanisms of these particles were inferred with their D_f values in each size-delimited regime.

Chapter 6 explores the possibility of using a BOF aerosol reactor to synthesize non-carbonaceous aerosol gels with tailorable material properties. Flame synthesis has been demonstrated as a versatile technology to produce various nanomaterials with well-defined material properties (Jiang et al. 2007; Thimsen and Biswas 2007; Kammler et al. 2001). Non-carbonaceous nanoparticles, such as titanium dioxide (TiO_2) with potential applications in many energy and environmental settings, have yet been synthesized in a gel form using flame aerosol reactors. This chapter provides a proof of concept demonstrating that flame synthesis of TiO_2 aerosol gels with controlled monomer size and crystal phase is feasible.

1.6 References

Bond, T. C., Doherty, S. J., Fahey, D. W., Forster, P. M., Berntsen, T., DeAngelo, B. J., ... & Kinne, S. (2013). Bounding the role of black carbon in the climate system: A scientific assessment. Journal of Geophysical Research: Atmospheres, 118(11), 5380-5552.

Brasil, A. M., Farias, T. L., and Carvalho, M. G. (2000). Evaluation of the Fractal Properties of Cluster-Cluster Aggregates. Aerosol Sci. Technol. 33:440–454.

Brasil, A. M., Farias, T. L., and Carvalho, M. G. (1999). A Recipe for Image Characterization of Fractal-Like Aggregates. J. Aerosol Sci. 30:1379–1389.

Brinker, C. J., & Scherer, G. W. (2013). Sol-gel science: the physics and chemistry of sol-gel processing. Academic press.

Cappa, C. D., Onasch, T. B., Massoli, P., Worsnop, D. R., Bates, T. S., Cross, E. S., ... & Kolesar, K. R. (2012). Radiative absorption enhancements due to the mixing state of atmospheric black carbon. Science, 337(6098), 1078-1081.

Chakrabarty, R. K., Beres, N. D., Moosmüller, H., et al. (2014). Soot superaggregates from flaming wildfires and their direct radiative forcing. Scientific reports, 4, 5508.

Chakrabarty, R. K., Garro, M. A., Chancellor, S., Herald, C., & Moosmüller, H. (2009). FracMAP: A user-interactive package for performing simulation and orientation-specific morphology analysis of fractal-like solid nano-agglomerates. Computer Physics Communications, 180(8), 1376-1381.

Chakrabarty, R. K., Garro, M. A., Garro, B. A., Chancellor, S., Moosmüller, H., & Herald, C. M. (2011a). Simulation of aggregates with point-contacting monomers in the cluster–dilute regime. Part 1: Determining the most reliable technique for obtaining three-dimensional fractal dimension from two-dimensional images. Aerosol Science and Technology, 45(1), 75-80.

Chakrabarty, R. K., Garro, M. A., Garro, B. A., Chancellor, S., Moosmüller, H., & Herald, C. M. (2011b). Simulation of aggregates with point-contacting monomers in the cluster–dilute regime. part 2: Comparison of two-and three-dimensional structural properties as a function of fractal dimension. Aerosol Science and Technology, 45(8), 903-908.

Chakrabarty, R. K., Moosmüller, H., Arnott, W. P., et al. (2009). Low fractal dimension cluster-dilute soot aggregates from a premixed flame. Physical review letters, 102(23), 235504.

Chakrabarty, R. K., Moosmüller, H., Garro, M. A., & Stipe, C. B. (2012). Observation of superaggregates from a reversed gravity low-sooting flame. Aerosol Science and Technology, 46(1), i-iii.

Chakrabarty, R. K., Novosselov, I. V., Beres, N. D., Moosmüller, H., Sorensen, C. M., & Stipe, C. B. (2014a). Trapping and aerogelation of nanoparticles in negative gravity hydrocarbon flames. Applied Physics Letters, 104(24), 243103.

Cross, E. S., Onasch, T. B., Ahern, A., et al. (2010). Soot Particle Studies—Instrument Inter-Comparison—Project Overview. Aerosol Sci. Technol., 44:592–611.

Dhaubhadel, R. (2008). An experimental study of dense aerosol aggregations (Doctoral dissertation, Kansas State University).

Dhaubhadel, R., Gerving, C. S., Chakrabarti, A., & Sorensen, C. M. (2007). Aerosol gelation: Synthesis of a novel, lightweight, high specific surface area material. Aerosol science and technology, 41(8), 804-810.

Dhaubhadel, R., Rieker, T. P., Chakrabarti, A., & Sorensen, C. M. (2012). Synthesis of silica aerosol gels via controlled detonation. Aerosol Science and Technology, 46(5), 596-600.

Dye, A. L., Rhead, M. M., and Trier, C. J. (2000). The Quantitative Morphology of Roadside and Background Urban Aerosol in Plymouth, UK. Atmos. Environ. 34:3139–3148.

Forrest, S. R., & Witten Jr, T. A. (1979). Long-range correlations in smoke-particle aggregates. Journal of Physics A: Mathematical and General, 12(5), L109.

Fry, D., Sintes, T., Chakrabarti, A., & Sorensen, C. M. (2002). Enhanced kinetics and free-volume universality in dense aggregating systems. Physical review letters, 89(14), 148301.

Friedlander, S. K. (2000). Smoke, Dust, and Haze: Fundamentals of Aerosol Dynamics. Oxford University Press, New York.

Goudeli, E., Eggersdorfer, M. L., & Pratsinis, S. E. (2016). Coagulation of agglomerates consisting of polydisperse primary particles. Langmuir, 32(36), 9276-9285.

Heinson, W. R. (2015). Simulation studies on shape and growth kinetics for fractal aggregates in aerosol and colloidal systems (Doctoral dissertation, Kansas State University).

Heinson, W. R., & Chakrabarty, R. K. (2016). Fractal morphology of black carbon aerosol enhances absorption in the thermal infrared wavelengths. Optics letters, 41(4), 808-811.

Heinson, W. R., Chakrabarti, A., & Sorensen, C. M. (2017). Kinetic percolation. Physical Review E, 95(5), 052109.

Heinson, W. R., Heinson, Y. W., Liu, P., & Chakrabarty, R. K. (2018). Breakdown of fractal dimension invariance in high monomer-volume-fraction aerosol gels. Aerosol Science and Technology, 52(9), 953-956.

Heinson, W. R., Liu, P., & Chakrabarty, R. K. (2017). Fractal scaling of coated soot aggregates. Aerosol Science and Technology, 51(1), 12-19.

Heinson, W. R., Sorensen, C. M., & Chakrabarti, A. (2010). Does shape anisotropy control the fractal dimension in diffusion-limited cluster-cluster aggregation?. Aerosol Science and Technology, 44(12), i-iv.

Heinson, W. R., Sorensen, C. M., & Chakrabarti, A. (2012). A three parameter description of the structure of diffusion limited cluster fractal aggregates. Journal of colloid and interface science, 375(1), 65-69.

Jiang, J., Chen, D. R., & Biswas, P. (2007). Synthesis of nanoparticles in a flame aerosol reactor with independent and strict control of their size, crystal phase and morphology. Nanotechnology, 18(28), 285603.

Kammler, H. K., Mädler, L., & Pratsinis, S. E. (2001). Flame synthesis of nanoparticles. Chemical Engineering & Technology: Industrial Chemistry‐Plant Equipment‐Process Engineering‐Biotechnology, 24(6), 583-596.

Katrinak, K. A., Rez, P., Perkes, P. R., and Buseck, P. R. (1993). Fractal Geometry of Carbonaceous Aggregates from an Urban Aerosol. Environ. Sci. Technol. 27:539–547.

Kim, W., Sorensen, C. M., Fry, D., & Chakrabarti, A. (2006). Soot aggregates, superaggregates and gel-like networks in laminar diffusion flames. Journal of aerosol science, 37(3), 386-401.

Kim, W., Sorensen, C. M., & Chakrabarti, A. (2004). Universal occurrence of soot superaggregates with a fractal dimension of 2.6 in heavily sooting laminar diffusion flames. Langmuir, 20(10), 3969-3973.

Kolb, M., Botet, R., & Jullien, R. (1983). Scaling of kinetically growing clusters. Physical Review Letters, 51(13), 1123.

Lee, C., and Kramer, T. A. (2004). Prediction of Three-Dimensional Fractal Dimensions using the Two-Dimensional Properties of Fractal Aggregates. Adv. Colloid Interface Sci. 112:49–57.

Lushnikov, A. A. (2006). Gelation in coagulating systems. Physica D: Nonlinear Phenomena, 222(1-2), 37-53.

Mandelbrot, B. B. (1977). Fractals: form, chance, and dimension (Vol. 706). San Francisco: WH Freeman.

McDonald, R., and Biswas, P. (2004). A Methodology to Establish the Morphology of Ambient Aerosols. J. Air Waste Manage. Assoc. 54:1069–1078.

McMurry, P. H., Wang, X., Park, K., and Ehara, K. (2002). The Relationship between Mass and Mobility for Atmospheric Particles: A New Technique for Measuring Particle Density. Aerosol Sci. Tech., 36:227–238.

Meakin, P. (1984). Computer simulation of cluster-cluster aggregation using linear trajectories: Results from three-dimensional simulations and a comparison with aggregates formed using brownian trajectories. Journal of colloid and interface science, 102(2), 505-512.

Meakin, P. (1985). Off lattice simulations of cluster-cluster aggregation in dimensions 2–6. Physics Letters A, 107(6), 269-272.

Meakin, P. (1999). A historical introduction to computer models for fractal aggregates. Journal of Sol-Gel Science and Technology, 15(2), 97-117.

Melas, A. D., Isella, L., Konstandopoulos, A. G., & Drossinos, Y. (2014). Morphology and mobility of synthetic colloidal aggregates. Journal of colloid and interface science, 417, 27-36.

Oh, C., & Sorensen, C. M. (1997). The effect of overlap between monomers on the determination of fractal cluster morphology. Journal of Colloid and Interface Science, 193(1), 17-25.

Pandey, A., Chakrabarty, R. K., Liu, L., & Mishchenko, M. I. (2015). Empirical relationships between optical properties and equivalent diameters of fractal soot aggregates at 550 nm wavelength. Optics express, 23(24), A1354-A1362.

Park, K., Kittelson, D., and McMurry, P. (2004). Structural Properties of Diesel Exhaust Particles Measured by Transmission Electron Microscopy (TEM): Relationships to Particle Mass and Mobility. Aerosol Sci. Technol. 38:881–889.

Pusey, P. N. (2011). Brownian Motion Goes Ballistic. *Science*, 332:802-803.

Rottereau, M., Gimel, J. C., Nicolai, T., & Durand, D. (2004). Monte Carlo simulation of particle aggregation and gelation: I. Growth, structure and size distribution of the clusters. The European Physical Journal E, 15(2), 133-140.

Sandkühler, P., Sefcik, J., & Morbidelli, M. (2004). Kinetics of gel formation in dilute dispersions with strong attractive particle interactions. Advances in colloid and interface science, 108, 133-143.

Samson, R. J.,Mulholland, G.W., and Gentry, J.W. (1987). Structural Analysis of Soot Agglomerates. Langmuir 3:272–281.

Scheckman, J. H., McMurry, P. H., and Pratsinis, S. E. (2009). Rapid Characterization of Agglomerate Aerosols by In Situ Mass-Mobility Measurements. Langmuir, 25:8248–8254.

Solomon, T. H., Weeks, E. R., and Swinney, H. L. (1993). Observation of Anomalous Diffusion and Lévy Flights in a Two-Dimensional Rotating Flow. *Phys. Rev. Lett.,* 71:3975-3978.

Sorensen, C. M. (2001). Light scattering by fractal aggregates: a review. Aerosol Science & Technology, 35(2), 648-687.

Sorensen, C. M. (2011). The mobility of fractal aggregates: a review. Aerosol Science and Technology, 45(7), 765-779.

Sorensen, C. M., & Chakrabarti, A. (2011). The sol to gel transition in irreversible particulate systems. Soft Matter, 7(6), 2284-2296.

Sorensen, C. M., & Hageman, W. B. (2001). Two-dimensional soot. Langmuir, 17(18), 5431-5434.

Sorensen, C. M., Hageman, W. B., Rush, T. J., Huang, H., & Oh, C. (1998). Aerogelation in a flame soot aerosol. Physical Review Letters, 80(8), 1782.

Sorensen, C. M., Kim, W., Fry, D., Shi, D., & Chakrabarti, A. (2003). Observation of soot superaggregates with a fractal dimension of 2.6 in laminar acetylene/air diffusion flames. Langmuir, 19(18), 7560-7563.

Sorensen, C. M., & Roberts, G. C. (1997). The prefactor of fractal aggregates. Journal of colloid and interface science, 186(2), 447-452.

Stauffer, D., & Aharony, A. (2018). Introduction to percolation theory. Taylor & Francis.

Thimsen, E., & Biswas, P. (2007). Nanostructured photoactive films synthesized by a flame aerosol reactor. AIChE Journal, 53(7), 1727-1735.

Van Dongen, P. G. J., & Ernst, M. H. (1985). Dynamic scaling in the kinetics of clustering. Physical review letters, 54(13), 1396.

Vicsek, T. Fractal growth phenomena, 1989, World Scientific, Singapore.

West, G. B. (2017). Scale: the universal laws of growth, innovation, sustainability, and the pace of life in organisms, cities, economies, and companies. Penguin.

Xiong, C., and Friedlander, S. K. (2001). Morphological Properties of Atmospheric Aerosol Aggregates. Proc. Natl. Acad. Sci. U. S. A. 98:11851–11856.

Zangmeister, C. D., Radney, J. G., Dockery, L. T., Young, J. T., Ma, X., You, R., and Zachariah, M. R. (2014). Packing Density of Rigid Aggregates is Independent of Scale. Proc. Natl. Acad. Sci. U.S.A., 111:9037–9041

Chapter 2: Establishing the Kinetics of Ballistic-to-Diffusive Transition using Directional Statistics

The results of this chapter have been published in Liu, P., Heinson, W. R., Sumlin, B. J., Shen, K.-Y., Chakrabarty, R. K. (2018). Establishing the kinetics of ballistic-to-diffusive transition using directional statistics. Physical Review E, 97(4), 042102.

Abstract

We establish the kinetics of ballistic-to-diffusive (BD) transition observed in two-dimensional random walk using directional statistics. Directional correlation is parameterized using the walker's turning angle distribution, which follows the commonly adopted wrapped Cauchy distribution (WCD) function. During the BD transition, the concentration factor (ρ) governing the WCD shape is observed to decrease from its initial value. We next analytically derive the relationship between effective ρ and time, which essentially quantifies the BD transition rate. The prediction of our kinetic expression agrees well with the empirical datasets obtained from correlated random walk simulation. We further connect our formulation with the conventionally used scaling relationship between the walker's mean-square displacement and time.

2.1 Introduction

A century ago, Einstein theorized the existence of a ballistic regime in Brownian motion at infinitesimally small timescales (Pusey 2011; Huang et al. 2011). This prediction was recently validated in experiments involving high temporal-resolution particle-tracking techniques (Huang et al. 2011; Li et al. 2010) or conducted in rarefied surrounding environment (Blum et al. 2006; Blum et al. 2000). The ballistic-to-diffusive (BD) transition, however, is not limited to Brownian systems driven by thermal fluctuation. A vast body of multidisciplinary research findings have witnessed a transient ballistic regime before the full development of diffusive motions. Examples include the random walk of atom clusters (Luedtke and Landman 1999; Maruyama and Murakami 2003), particle advection in weak turbulence (Solomon et al. 1993; Solomon et al. 1994), bacterial migration (Zhang et al. 2009), and animal foraging activities (Bartumeus et al. 2005; Getz and Saltz 2008). The kinetics of BD transition determines the critical timescale corresponding to the onset of diffusion and subsequent applicability of the diffusive approximation. Despite its wide practical significance, a generalized mathematical formulation of the transition kinetics remains elusive. When formulating a generalized kinetic expression, difficulty arises from the multitude of system-specific driving mechanisms, as well as the order-of-magnitude variances in system length scales (Maruyama and Murakami 2003; Solomon et al. 1993; Zhang et al. 2009; Bartumeus et al. 2005). One viable approach is to interpret the BD transition from a statistical perspective, and past attempts have been made on this front using the central limit theorem (CLT) (Maruyama and Murakami 2003; Mantegna and Stanley 1994). Although it can satisfactorily explain the diffusive tendency of the random walk at large timescale, CLT ultimately fails to capture and parameterize the transition kinetics.

Here we interpret the BD transition in two-dimensional (2D) space using directional statistics (Mardia and Jupp 2009; Lee 2010; Batschelet 1981). More specifically, the subject of investigation is the probability distribution (P) of the walker's turning angle (θ), which describes the correlation between the successive steps of motion. Experimentally, the acquisition of $P(\theta)$ is typically done using single-particle tracking techniques. If the motion is strictly ballistic, angle θ only takes value of 0 and the probability density of $\theta = 0$ is infinitely large; thus, $P(\theta)$ is a Dirac δ function written as $\delta(0)$ (Bartumeus et al. 2005; Mardia and Jupp 2009; Lee 2010; Batschelet 1981). The 2D diffusion, on the other hand, is random walk manifesting an equiprobability of θ within the complete range between $-\pi$ to π, and therefore, $P(\theta)$ is a circular uniform function of $1/(2\pi)$ (Bartumeus et al. 2005; Mardia and Jupp 2009; Lee 2010; Batschelet 1981). During the BD transition, the dissipation in the correlation of the random walk could be captured by the evolution of $P(\theta)$ from $\delta(0)$ to $1/(2\pi)$ when the timescale increases by order-of-magnitude. In directional statistics, one of the mathematical expressions that could capture this evolution is the wrapped Cauchy distribution (WCD) function (Bartumeus et al. 2005; Mardia and Jupp 2009; Lee 2010; Batschelet 1981).

Equation (2.1) shows the formulation of WCD function centered at $\theta = 0$,

$$P(\theta, \rho) = \frac{1 - \rho^2}{2\pi[1 + \rho^2 - 2\rho\cos(\theta)]};\ \theta \in (-\pi, \pi] \tag{2.1}$$

where $\rho \in [0, 1]$ is the concentration factor that governs the shape of the distribution (Bartumeus et al. 2005; Mardia and Jupp 2009; Lee 2010; Batschelet 1981). When ρ approaches 1 and 0, the WCD function asymptotes to the two extremities, $\delta(0)$ and $1/(2\pi)$, respectively. The kinetics of

BD transition could therefore be established by relating the decrease in ρ from 1 to 0 with a timescale parameter.

We show in the subsequent paragraphs the BD transition observed in the 2D stochastic motion which was numerically simulated using the correlated random walk (CRW) model. The transition is tracked using the time-evolution of the random walker's reorientation statistics, as well as the inflection observed in the spatiotemporal scaling relationship of the motion. Next, we formulate the kinetics of BD transition by establishing the mathematical relationship between the effective value of ρ and timescale. We conclude this paper by connecting our kinetic formulation with the spatiotemporal scaling relationship which has been commonly adopted in previous works (Pusey 2011; Huang et al. 2011; Luedtke and Landman 1999; Maruyama and Murakami 2003; Solomon *et al*. 1993; Solomon *et al*. 1994; Zhang *et al*. 2009; Bartumeus *et al*. 2005; Getz and Saltz 2008).

2.2 Methods

The CRW simulation follows the procedure introduced in Refs. (Bartumeus *et al*. 2005; Haefner 2005). A 2D unbounded, Cartesian space was created and the random walker was initially placed at the origin O ($x = 0$, $y = 0$, $t = 0$), where x and y represent the 2D coordinates. The parameter t represents simulation time which increments by unit timescale τ_1. At the beginning of each timestep, a turning angle θ is randomly generated per the WCD function governed by a fixed shape factor ρ_1 corresponding to the unit timescale τ_1. The random generation of θ follows the cumulative inversion method outlined in Ref. (Haefner 2005). Next, the random walker moves according to the direction designated by θ with a constant step-length δ_1. The algorithm repeats this procedure

until the last timestep $t_n = 10^6\tau_1$ is reached and the trajectory of the random walker is recorded as an array $[x(t), y(t)]$.

From the trajectory $[x(t), y(t)]$, the walker's time-averaged mean-square displacement $\langle\delta^2\rangle$ was calculated in a manner similar to that introduced in Refs. (Metzler *et al*. 2014; Andreanov and Grebenkov 2012):

$$\langle\delta^2(\tau)\rangle = \frac{\tau_1}{t_n - \tau}\sum_{t=\tau_1}^{t_n-\tau}\left[\big(x(t+\tau) - x(t)\big)^2 + \big(y(t+\tau) - y(t)\big)^2\right] \tag{2.2}$$

where τ represents a finite time interval divisible by τ_1. The walker's turning angle θ corresponding to timescale $\tau > \tau_1$ was calculated from its trajectory, specifically every three successive positions written as $[x(t), y(t)]$, $[x(t + \tau), y(t + \tau)]$, and $[x(t + 2\tau), y(t + 2\tau)]$. The detailed numerical method for this calculation is included in Appendix I, Section A1.1. We next divided the complete range of θ from $-\pi$ to π equally into 500 bins and obtained $P(\theta)$ by counting the frequency of θ within each bin. The effective value of ρ at τ was determined by performing the least square fit to the corresponding $P(\theta)$ datasets per Eq. (2.1).

2.3 Results and Discussion

Figure 2.1 shows the random walk generated using a WCD function with $\rho_1 = 0.95$. The walker's trajectories observed under different timescales are colored in gray ($\tau = \tau_1$) and black ($\tau = 10^2\tau_1$). When τ increases by order-of-magnitude, the correlation between successive steps of the motion becomes elusive and a Brownian-like random walk behavior manifests.

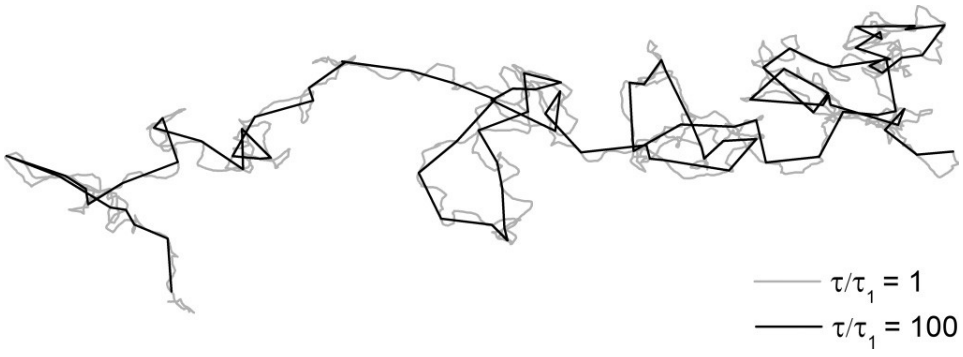

Figure 2.1. Examples of the random walk simulated using a WCD function with $\rho_1 = 0.95$. The walker's trajectories observed under normalized timescale $\tau/\tau_1 = 1$ and 10^2 are colored in gray and black, respectively.

Figure 2.2(a) shows the scaling relationship between the walker's normalized mean-square displacement and timescale $\langle\delta^2\rangle/\delta_1^2 \propto (\tau/\tau_1)^\gamma$. The BD transition could be inferred from the inflection in the power-law relationship, which is signified by the decrease in the exponent γ from 2 to 1 (Pusey 2011; Huang *et al.* 2011). Corresponding to the regime in which the inflection takes place, we show the evolution of the walker's $P(\theta)$ in Fig. 2.2(b). When timescale of observation is small, *e.g.*, $\tau/\tau_1 = 4$, $P(\theta)$ is centralized at $\theta = 0$ and manifests a sharp peak. With increase in τ/τ_1 by two orders of magnitude, $P(\theta)$ broadens and approaches uniformity. Qualitatively, one could predict the onset of normal diffusion based on the increase in the width at half minimum of $P(\theta)$. Quantitatively, we performed least-square fitting on the measured $P(\theta)$ datasets (circles) per the WCD function (red lines) and good agreement was observed. The effective value of ρ is seen to decrease from ρ_1 as τ/τ_1 increases, and those values are labeled in the subpanels of Fig. 2.2(b).

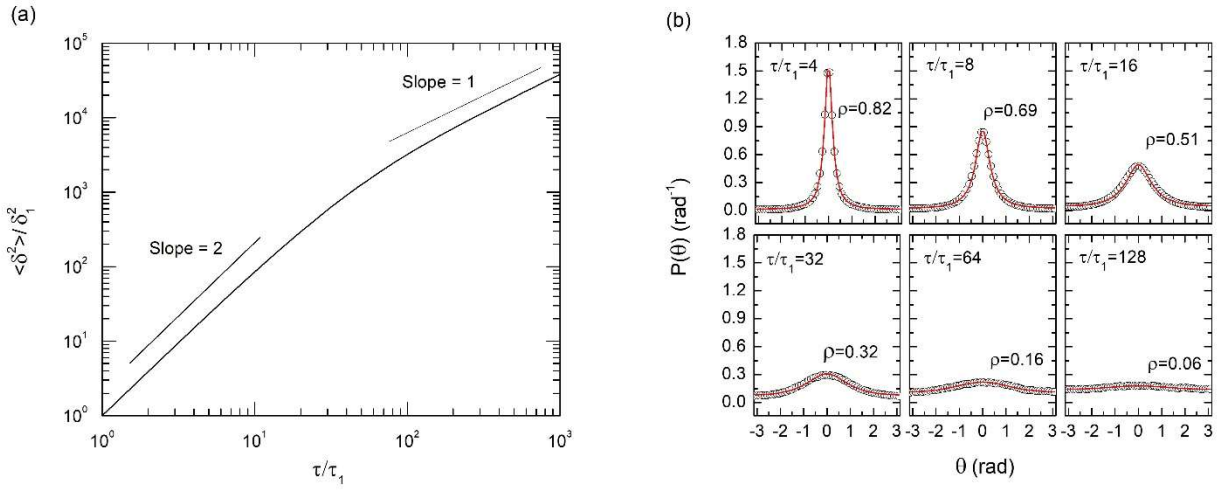

Figure 2.2. (a) Normalized time-averaged mean-square displacement $<\delta^2>/\delta_1^2$ as a function of normalized timescale τ/τ_1 for the random walk simulated with $\rho_1 = 0.95$. Straight lines in the log-log plot have slopes of 2 and 1, corresponding to the values of scaling exponent γ for ballistic motion and diffusion, respectively. (b) Evolution of the walker's turning angle distribution $P(\theta)$ with τ/τ_1 increasing from 4 to 128. Circles represent the $P(\theta)$ datasets empirically obtained from the CRW simulation. Red lines follow the WCD function (Eq. (2.1)) parameterized by the ρ values shown in each subpanel.

The WCD function is not only limited to parameterizing the shape of $P(\theta)$ at unit timescale, it also accurately predicts the evolution of distribution shape with increasing τ. We next analytically derive the mathematical relationship between the effective ρ value and τ. Our derivation is based on correlating the probability density of turning angles observed with increasing timescales as:

$$\tau_{2i} = 2\tau_i \tag{2.3}$$

where τ_i represents any arbitrary timescale and τ_{2i} represents the timescale twice larger than τ_i. Our goal here is to establish the relationship between the corresponding ρ_{2i} and ρ_i.

Figure 2.3(a) shows that when the motion is observed with timescale τ_i, the random walker is seen at five successive locations (black dots). From these five locations, three successive turning angles could be identified, and they are written as $\theta_{i,1}$, $\theta_{i,2}$, and $\theta_{i,3}$. When the timescale increases by two

(that is τ_{2i}), the walker could only be seen at three locations (blue dots in Fig. 2.3(b)), giving rise to one turning angle written as θ_{2i}. This geometric presentation in Figure 2.3 implies that once three successive turning angles $\{\theta_{i,1}, \theta_{i,2}, \theta_{i,3}\}$ are observed at any timescale, one definite turning angle θ_{2i} will be conceived at the timescale twice larger.

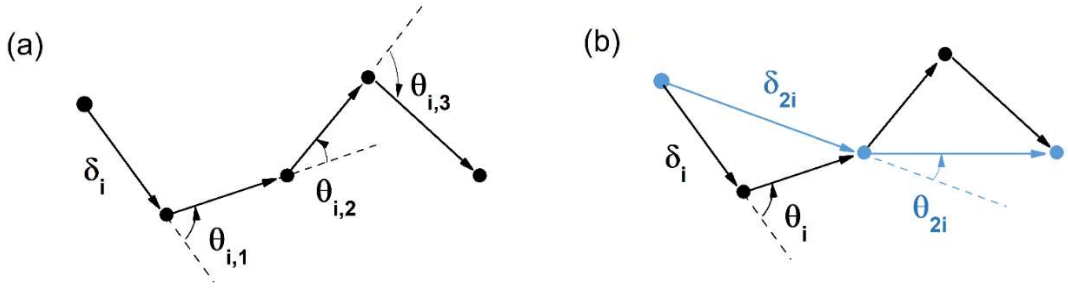

Figure 2.3. (a) The random walker is seen at five locations (black dots) when the motion is observed with timescale τ_i, which gives rise to three successive turning angles $\theta_{i,1}$, $\theta_{i,2}$, and $\theta_{i,3}$. (b) When the timescale increases by two, that is τ_{2i} , the walker could only be seen at three locations (blue dots). Correspondingly one turning angle θ_{2i} is conceived. Vectors shown in black δ_i and blue δ_{2i} represent the net displacements of the walker during τ_i and τ_{2i}, respectively. The magnitude of δ_i is assumed to be constant.

Assuming the magnitude of displacement δ_i during τ_i to be constant, those turning angles shown in Fig. 2.3 could be related per the following relationship:

$$\theta_{2i} = \theta_{i,2} + \frac{1}{2}(\theta_{i,1} + \theta_{i,3}) \tag{2.4}$$

Angles in Eq. (2.4) are vector quantities and they take positive values along counterclockwise direction. Noting the probabilities for the onset of $\theta_{i,1}$, $\theta_{i,2}$, and $\theta_{i,3}$ to be $P(\theta_{i,1})$, $P(\theta_{i,2})$, and $P(\theta_{i,3})$, respectively, we write the probability for the successive occurrence of $\{\theta_{i,1}$, $\theta_{i,2}$, and $\theta_{i,3}\}$ as the product $P(\theta_{i,1})P(\theta_{i,2})P(\theta_{i,3})$. Note that here we have assumed the onset of successive turning angles to be independent events, which differs fundamentally from the persistent random walk model introduced and adopted elsewhere (Masoliver et al. 1989). The probability $P(\theta_{2i})$ then could be

calculated by summing the values of $P(\theta_{i,1})P(\theta_{i,2})P(\theta_{i,3})$ for all exclusive combinations of $\{\theta_{i,1}, \theta_{i,2}, \theta_{i,3}\}$ that satisfies Eq. (2.4). This relationship could be written as:

$$P(\theta_{2i}, \rho_{2i}) = \sum_{\theta_{i,2}+\frac{1}{2}(\theta_{i,1}+\theta_{i,3})=\theta_{2i}} P(\theta_{i,1}, \rho_i)P(\theta_{i,2}, \rho_i)P(\theta_{i,3}, \rho_i) \quad (2.5)$$

Solving Eq. (2.5) with any arbitrary θ_{2i} yields the relationship between ρ_{2i} and ρ_i.

We demonstrate the solution to Eq. (2.5) with $\theta_{2i} = 0$ as an example (and note that solving the equation with other θ_{2i} values should yield the same result). The first independent variable $\theta_{i,1}$ takes value freely within the complete range between π to π; however, it takes value from the complete range twice until all exclusive outcomes are exhausted. The second independent variable $\theta_{i,2}$ takes value in the range defined by $\theta_{i,1}$, specifically, $\theta_{i,2,min} = -\frac{1}{2}(\theta_{i,1} + \pi)$ and $\theta_{i,2,max} = -\frac{1}{2}(\theta_{i,1} - \pi)$ (more detailed discussions on the ranges for $\theta_{i,1}$ and $\theta_{i,2}$ are respectively included in Appendix I, Section A1.2 and A1.3). Once both $\theta_{i,1}$ and $\theta_{i,2}$ have been specified, there exists a unique $\theta_{i,3} = -\theta_{i,1} - 2\theta_{i,2}$ which satisfies our premise $\theta_{2i} = 0$. Therefore, the Eq. (2.5) yields to the following continuous form:

$$P(\theta_{2i} = 0, \rho_{2i}) =$$

$$2\int_{\theta_{i,1}=-\pi}^{\pi}\int_{\theta_{i,2}=-\frac{1}{2}(\theta_{i,1}+\pi)}^{-\frac{1}{2}(\theta_{i,1}-\pi)} P(\theta_{i,1}, \rho_i)\, P(\theta_{i,2}, \rho_i)P(-(\theta_{i,1} + 2\theta_{i,2}), \rho_i)d\theta_{i,2}d\theta_{i,1} \quad (2.6)$$

The right-hand side of Eq. (2.6) was solved using Monte Carlo integration (Robert 2014) and the resultant relationship between ρ_{2i} and ρ_i is plotted in Fig. 2.4 as the solid line. The empirical

datasets of $\rho_{2i}(\rho_i)$ determined from CRW simulation (shown as circles) agrees with the solution to Eq. (2.6).

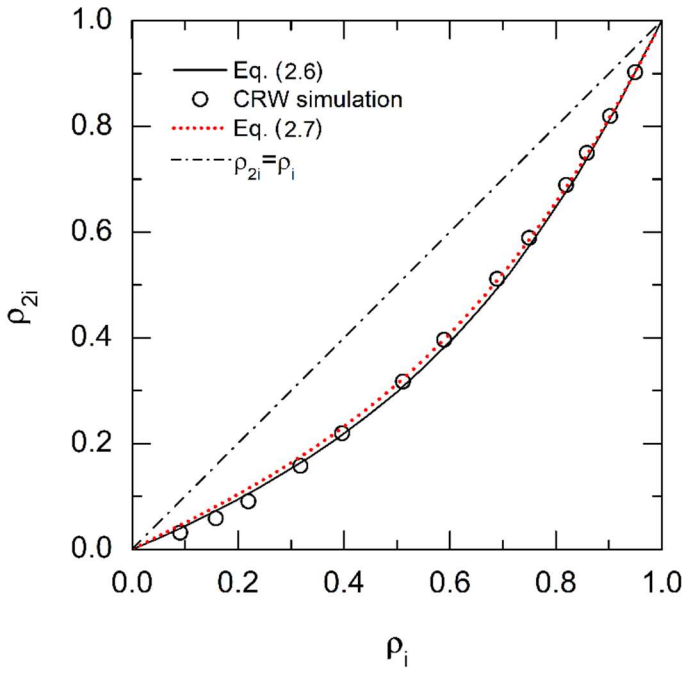

Figure 2.4. Relationship between ρ_{2i} and ρ_i. Solid line follows the solution to the analytical equation (2.6). Circles represent empirical datasets obtained from CRW simulation by performing least square fitting to the measured $P(\theta)$ at changing τ. Dotted line follow Eq. (2.7). The dash-dot line represents a hypothetical relationship $\rho_{2i} = \rho_i$.

The dash-dot line in Figure 2.4 follows a hypothetical relationship $\rho_{2i} = \rho_i$ and it connects with the solution of Eq. (2.6) only at the two extremities: $\rho_{2i} = \rho_i = 1$ and $\rho_{2i} = \rho_i = 0$. These two connections imply that strict ballistic motion and fully developed diffusion will remain so, independent of the changing timescale. On the other hand, when $0 < \rho_i < 1$, the solution to Eq. (2.6) always resides below the hypothetical $\rho_{2i} = \rho_i$ line. This dictates that ρ will always decrease with increasing τ, or in other words, the correlated random walk appearing ballistic will eventually manifest as diffusive upon prolonged observation, regardless of how close ρ_1 is to unity. To

conclude this part of discussion, we put forth the simpler expression in Eq. (2.7) which is obtained by performing a least square fit on the numerical solution to Eq. (2.6):

$$\frac{\rho_{2i}}{\rho_i} = \frac{1}{2}(\rho_i^2 + 1) \tag{2.7}$$

Note that the aforementioned deductions based on Eq. (2.6) is also captured by Eq. (2.7). Figure 2.5 (a), (b) and (c) show the decrease in the effective value of ρ as a function of normalized timescale τ/τ_1 for random walkers starting with ρ_1 = 0.99, 0.95 and 0.50, respectively. The ρ values calculated using Eq. (2.6) and (2.7) are compared with that determined from CRW simulation.

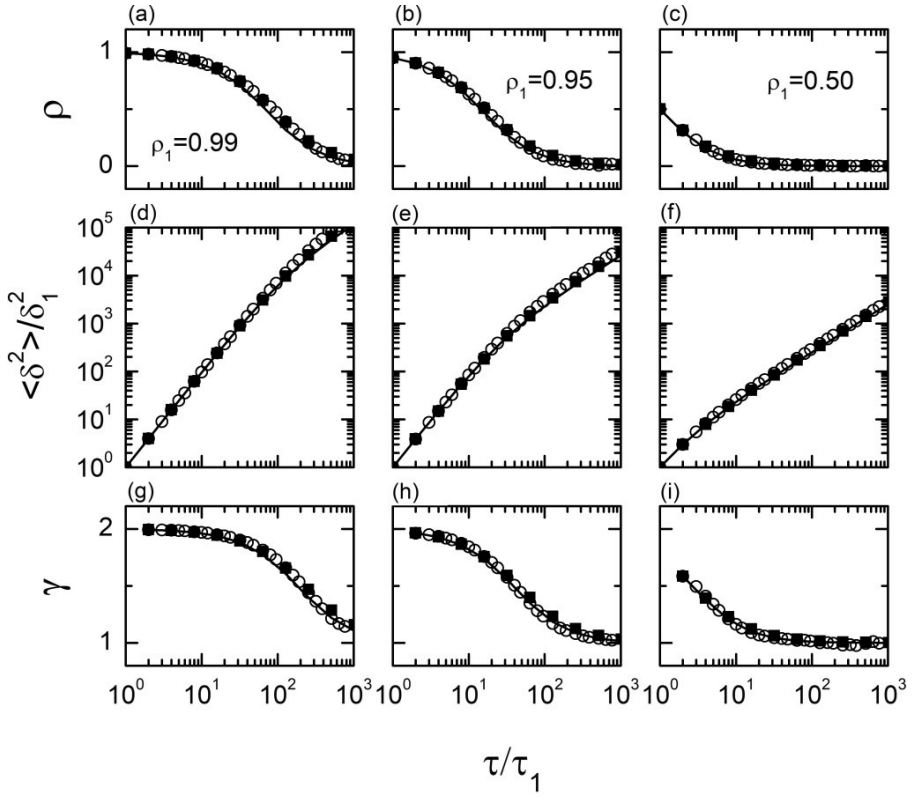

Figure 2.5. (a), (b) and (c) show the decrease in the effective value of ρ for random walker starting with ρ_1 = 0.99, 0.95 and 0.50, respectively. (d)-(f) show the corresponding normalized $<\delta^2>/\delta_1^2 \sim (\tau/\tau_1)^{\gamma}$ scaling relationship. (g)-(i) show the evolution of the scaling exponent γ. In (a)-(c) solid lines represent solutions to equation Eq. (2.6). Circles represent empirical datasets obtained from CRW simulation. Squares follow Eq. (2.7). In (d)-(i) solid line represents solution to equation sets (2.6) and (2.10). Circles represent empirical datasets calculated from CRW simulation using Eq. (2.2). Squares represent solution to equation sets (2.7) and (2.10).

We next connect the directional statistic interpretation of BD transition with the conventional spatio-temporal scaling relationship $\langle \delta^2 \rangle \propto \tau^{\gamma}$ of the random walker. Per Figure 2.3(b) the walker's net displacement δ_{2i} during τ_{2i} could be related to the turning angle θ_i observed with τ_i (assuming constant net displacement δ_i during τ_i), that is $\delta_{2i}(\theta_i) = 2\delta_i \cos(\theta_i/2)$. Substitute the constant δ_i by $\langle \delta_i^2 \rangle^{1/2}$ and the relationship yields to $\delta_{2i}(\theta_i) = 2\langle \delta_i^2 \rangle^{1/2} \cos(\theta_i/2)$. Next, the ratio $\langle \delta_{2i}^2 \rangle / \langle \delta_i^2 \rangle$ equals to the trigonometric moment of the WCD function parameterized by ρ_i:

$$\langle \delta_{2i}^2 \rangle / \langle \delta_i^2 \rangle = 4 \int_{-\pi}^{\pi} \cos^2(\theta_i/2) P(\theta_i, \rho_i) \, \mathrm{d}\theta_i \tag{2.8}$$

The exact analytical solution to Eq. (2.8) is:

$$\langle \delta_{2i}^2 \rangle / \langle \delta_i^2 \rangle = 2(\rho_i + 1) \tag{2.9}$$

Generalization of Eq. (2.9) yields the expression for the walker's normalized mean-square displacement $\langle \delta_{2^n}^2 \rangle / \delta_1^2$ corresponding to timescale τ_{2^n}/τ_1 (where n is positive integer):

$$\langle \delta_{2^n}^2 \rangle / \delta_1^2 = 2^n \prod_{m=1}^{n} (\rho_{2^{m-1}} + 1) \tag{2.10}$$

The solutions to equation sets (2.10) and (2.6) with ρ_1 = 0.99, 0.95 and 0.50 are plotted in Figure 2.5 (d)-(i) as the solid lines. Circles represent the empirical dataset obtained from the simulated random walk ($\langle \delta^2 \rangle / \delta_1^2$ is calculated using Eq. (2.2) for simulation). The comparison shows that our analytical solution gives accurate prediction to magnitude of the walkers $\langle \delta^2 \rangle$ as well as the earliness of BD transition. Eq. (2.10) could be also solved along with the simple expression of Eq. (2.7), which gives reasonably accurate results (squares). Figure 2.5 also shows that although the diffusive regime manifests earlier in the case of smaller ρ_1, the shape of the decreasing trends of γ

and ρ appears invariant. This is because it always takes a fixed amount of time for ρ to decrease from one specific value to another per Eqs. (2.6) or (2.7).

Rearranging Eq. (2.9) yields the relationship between γ_{2i} and ρ_i:

$$\gamma_{2i} = 1 + \log_2(\rho_i + 1) \tag{2.11}$$

which when solved with Eq. (2.6) or (2.7) provides the relationship between γ and ρ at a given τ. Figure 2.6 shows the relationship between γ and ρ obtained using our analytical formulations (solid and dotted lines) and from CRW simulation (circles). Good agreement is observed between the datasets.

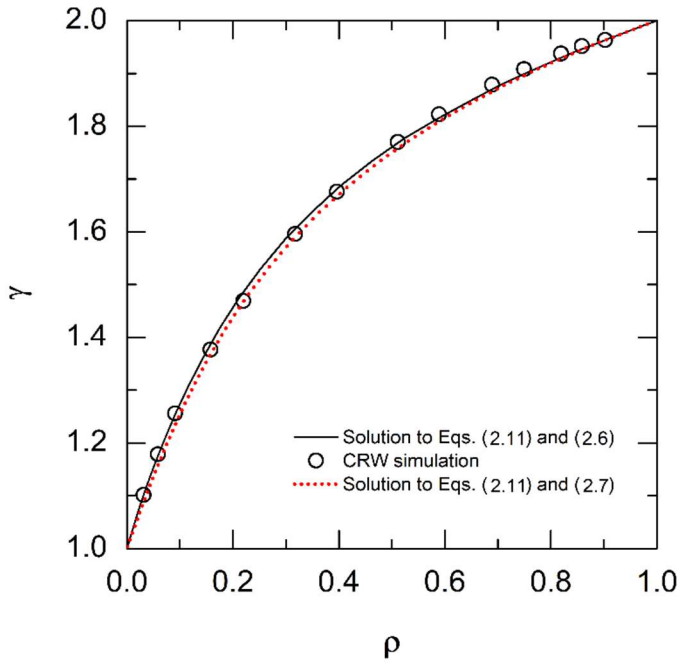

Figure 2.6. Relationship between γ and ρ. Solid line represents the solution to the equation set (2.11) and (2.6). Circles represent empirical datasets obtained from CRW simulation. Dotted line represents the solution to equation set (2.11) and (2.7).

2.4 Conclusion

We now bring together our major findings and conclude this chapter. Relationship between the two parameters ρ and τ is formulated using Eq. (2.6) (or Eq. (2.7)), and therefore the kinetics of BD transition is quantified. The one-to-one correspondence between ρ and γ is established using Eq. (2.11), such that our kinetic expression is tied to the conventionally used spatial-temporal scaling relationship. Figure 2.7 shows the contour plots for γ as a function of ρ_1 and τ/τ_1. Using this figure, one could roughly estimate the value of γ corresponding to a particular timescale. Use of the contour lines, however, is not recommended if an exact solution is desired. An accurate estimation of γ still requires solving of Eq. (2.6) (or Eq. (2.7) and Eq. (2.11). In addition, we emphasize that the robustness of WCD function in describing the walker's turning angle distribution remains to be tested experimentally for more complicated random walk processes, for example, particle motion in three-dimensional space with or without geometric confinements. The evolution of reorientation statistics for the random walk modulated with changing step-length distribution also requires further investigations (Bartumeus et al. 2005). We also point out that WCD is not the only function that finds applications in parametrizing random walk observed experimentally; future work will be directed toward generalizing the formulation presented in this work to the family of wrapped distribution functions (Mardia and Jupp 2009; Lee 2010; Batschelet 1981).

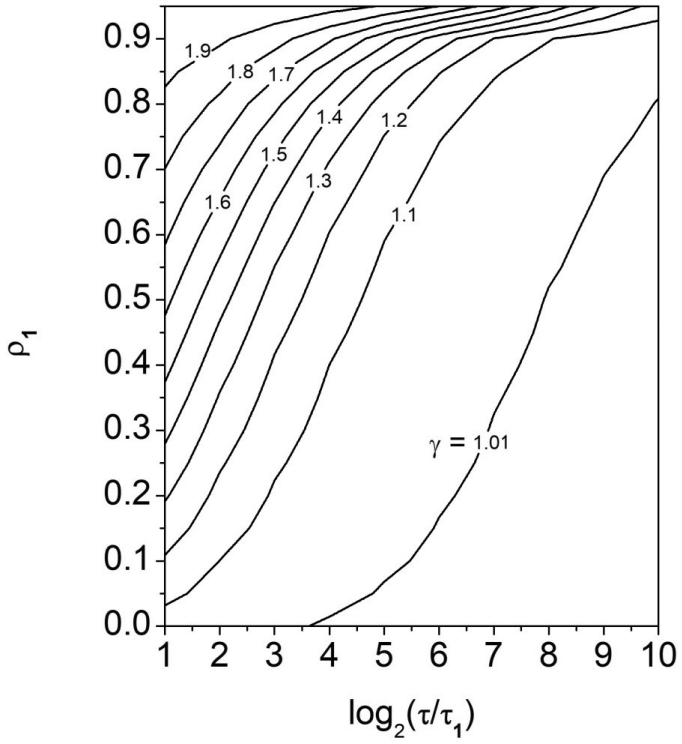

Figure 2.7. Contour plots of γ as a function of ρ_1 and normalized timescale τ/τ_1.

2.5 References

Andreanov, A., and Grebenkov, D. S. (2012). Time-Averaged MSD of Brownian Motion. *J. Stat. Mech.*, P07001.

Bartumeus, F., da Luz, M. G. E., Viswanathan, G. M., and Catalan, J. (2005). Animal Search Strategies: A Quantitative Random-Walk Analysis. *Ecology,* 86:3078-3087.

Batschelet, E. Circular Statistics in Biology, Academic Press, New York, USA, 1981.

Blum, J., Wurm, G., Kempf, S., *et al.*, (2000). Growth and Form of Planetary Seedlings: Results from a Microgravity Aggregation Experiment. *Phys. Rev. Lett.*, 85:2426.

Blum, J., Bruns, S., Rademacher, D., Voss, A., Willenberg, B., and Krause, M. (2006). Measurement of the Translational and Rotational Brownian Motion of Individual Particles in a Rarefied Gas. *Phys. Rev. Lett.*, 97:23060.

Getz, W. M., and Saltz, D. (2008). A Framework for Generating and Analyzing Movement Paths on Ecological Landscapes. *Proc. Natl. Acad. Sci. USA*, 105:19066-19071.

Haefner, J. W., Modeling Biological Systems: Principles and Applications, Springer Science and Business Media, Berlin, 2005.

Huang, R., Chavez, I., Taute, K. M., Lukić, B., Jeney, S., Raizen, M. G., and Florin, E. L. (2011). Direct Observation of the Full Transition from Ballistic to Diffusive Brownian Motion in a Liquid. *Nat. Phys.*, 7:576-580.

Lee, A. (2010). Circular Data. *Wiley Interdiscip. Rev. Comput. Stat.*, 2:477–486.

Li, T., Kheifets, S., Medellin, D., and Raizen, M. G. (2010). Measurement of the Instantaneous Velocity of a Brownian Particle. *Science*, 328:1673–1675.

Luedtke, W. D., and Landman, U. (1999). Slip Diffusion and Levy Flights of an Adsorbed Gold Nanocluster. *Phys. Rev. Lett.,* 82:3835-3838.

Mantegna, R. N., and Stanley, H. E. (1994). Stochastic Process with Ultraslow Convergence to a Gaussian: The Truncated Lévy Flight. *Phys. Rev. Lett.*, 73:2946-2949.

Mardia, K. V., and Jupp, P. E. Directional Statistics, John Wiley and Sons, New York, USA, 2009.

Maruyama, Y., and Murakami, J. (2003). Truncated Levy Walk of a Nanocluster Bound Weakly to an Atomically Flat Surface: Crossover from Superdiffusion to Normal Diffusion. *Phys. Rev. B*, 67:085406.

Masoliver, J., Lindenberg, K., and Weiss, G. H. (1989). A Continuous-Time Generalization of the Persistent Random Walk. *Physica A*, 157:891-898.

Metzler, R., Jeon, J. H., Cherstvy, A. G., and Barkai, E. (2014). Anomalous Diffusion Models and Their Properties: Non-Stationarity, Non-Ergodicity, and Ageing at the Centenary of Single Particle Tracking. *Phys. Chem. Chem. Phys.*, 16:24128-24164.

Pusey, P. N. (2011). Brownian Motion Goes Ballistic. *Science*, 332:802-803.

Robert, C. P., Monte Carlo Methods, John Wiley and Sons, New York, USA, 2014.

Solomon, T. H., Weeks, E. R., and Swinney, H. L. (1993). Observation of Anomalous Diffusion and Lévy Flights in a Two-Dimensional Rotating Flow. *Phys. Rev. Lett.,* 71:3975-3978.

Solomon, T. H., Weeks, E. R., and Swinney, H. L. (1994). Chaotic Advection in a Two-Dimensional Flow: Lévy Flights and Anomalous Aiffusion. *Physica D,* 76:70-84.

Zhang, H. P., Be'Er, A., Smith, R. S., Florin, E. L., and Swinney, H. L. (2009). Swarming Dynamics in Bacterial Colonies. *EPL,* 87:48011.

Chapter 3: Sensitivity Analysis of Aggregate Morphology on Mass-Mobility Relationship and Improved Parameterizations

The results of this chapter have been published in Liu, P., Chakrabarty, R. K. (2016). Sensitivity analysis of aggregate morphology on mass-mobility relationship and improved parameterizations. Aerosol Science and Technology, 50(1), 63-70.

Abstract

Past studies have shown that the diffusion-limited cluster aggregation mechanism yields aggregate with a mass fractal dimension (D_f) of around 1.8 and power-law prefactor (k_f) ranging between 1.2 and 2.5. For a fixed D_f, an increasing k_f physically manifests as decreasing shape anisotropy or the degree of "stringiness" of an aggregate. In this work, we investigate the effects of changing k_f, monomer size (d), and number of monomers (N) of computer-simulated aggregates on their mass-mobility scaling exponent (D_{fm}) and prefactor (k_{fm}). Our simulation results for a statistically significant number of $D_f = 1.78 \pm 0.10$ aggregates yield D_{fm} values of 2.20 ± 0.05. These values are in excellent agreement with previous experimental observations. While variations in D_{fm} were predominantly influenced by D_f, k_{fm} showed sensitivity to fluctuations in k_f. The validity and accuracy of the empirical power-law exponent 1.08 used for estimating N in three dimensions from two-dimensional projection images was also evaluated. It was found that the exponent was only valid for aggregates with k_f close to unity. A correction has been proposed to account for the enhanced apparent screening effects at large k_f.

3.1 Introduction

Random collision and irreversible aggregation of non-coalesced solid nanoparticles (hereafter called monomers) in gas phase, described by the mechanism of diffusion-limited cluster aggregation (DLCA), are ubiquitous in various natural and industrial scenarios ranging from soot formation in flames to nanomaterial synthesis in high-temperature reactors (Hyeon-Lee et al. 1998; Sorensen 2011; Chakrabarty et al. 2014). The resulting aggregate morphology is self-similar in nature over a finite length scale (i.e., monomer size), which facilitates fractal mathematics to describe its morphology. A power-law correlation, shown in Equation (3.1), between the total number of monomers (N) constituting an aggregate and the ratio of aggregate radius of gyration (R_g) to monomer radius (a) has been used to quantify the structure of aggregates (Sorensen 2001, 2011):

$$N = k_f \left(\frac{R_g}{a}\right)^{D_f} \tag{3.1}$$

where D_f is the fractal dimension of an aggregate and k_f is the scaling prefactor. Past few decades have seen a number of studies conducted to investigate the D_f of aggregates formed via DLCA in different combustion systems (Friedlander 2000; Sorensen 2001, 2011). However, k_f has been an understudied parameter, and has only recently been shown to be related to the shape anisotropy of aggregates (Heinson et al. 2010; Melas et al. 2014a). With decreasing k_f, an aggregate with a fixed D_f would turn "stringier-looking" as depicted in Figure 3.1. This change in aspect ratio represents the shape-governing role of k_f from a macro-scale perspective, which helped reconcile the contradiction between the predictions of classical DLCA theory and the experimental observation of quasi-one-dimensional aggregates from premixed flames (Chakrabarty et al. 2009; Heinson et al. 2010). From a micro-scale perspective, Melas et al. (2014 a, b) reported that k_f is related to the

local structural compactness of an aggregate. With increasing k_f, the number density of three-monomer angles increased significantly for ≤80°, indicating that monomers get packed more compactly (Melas et al. 2014a).

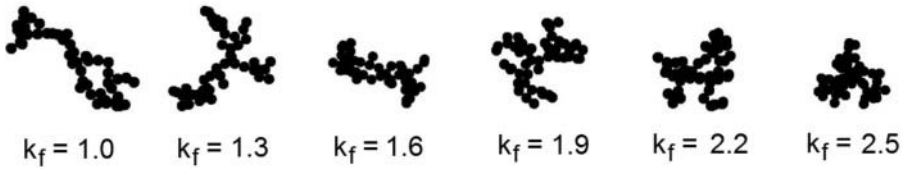

Figure 3.1. Snapshots of fractal aggregate morphologies (generated using *FracMAP*) with D_f = 1.78, N = 50, and k_f ranging between 1.0 to 2.5. Increase in the aspect ratio or shape anisotropy of aggregates is evident with decreasing k_f.

In spite of these recent advances in the physical characterization of fractal aggregates, there still lies an apparent gap in relating aggregate morphology to its mass-mobility characteristics (Sorensen 2011). With the advent of the particle mass-based classifier (McMurry et al. 2002; Park et al. 2004; Scheckman et al. 2009), there have been numerous studies conducted on characterizing aggregate morphology using the knowledge of particle mobility in the transition flow regime (0.1 < Kn < 10 as defined in Sorensen 2011). These studies have used a power-law relationship between the aggregate mobility diameter and mass in the form of standard "fractal" equation, as shown in Equations (3.2a) and (3.2b):

$$M = k_{fm}\left(\frac{d_m}{d}\right)^{D_{fm}} \tag{3.2a}$$

$$N = K_{fm}\left(\frac{d_m}{d}\right)^{D_{fm}} \text{ and } K_{fm} = \frac{6k_{fm}}{\rho\pi d^3} \tag{3.2b}$$

where M is the aggregate mass; k_{fm} is the aggregate mass-mobility prefactor; D_{fm} is the aggregate mass-mobility exponent; d_m is the aggregate mobility diameter; and d is the monomer diameter. It is noteworthy that many of these studies have wrongly addressed D_{fm} as the true aggregate fractal dimension (Sorensen 2011, and references therein). Some studies have also remarked that freshly emitted aggregates, which according to the DLCA theory should possess $D_f \sim 1.78$, have fractal dimensions of around 2.2. Melas and co-workers (2014b) recently investigated variations in D_{fm} and k_{fm} with different pairs of D_f and k_f in the transition regime; however, there is still much work to be done in establishing empirical relationships between D_f, D_{fm}, k_f, and k_{fm} for aiding experimental research using the mass-mobility technique. In this work, an effort is made to establish these relationships for aggregates with D_f, N, and k_f respectively ranging between 1.68 and 1.88, 5 and 500, and 1.0 and 2.5. Please note that the mass-mobility relationship in Equation (3.2a) could be rearranged in the form of Equation (3.2b) to better fit the purposes of this study. We normalized aggregate k_{fm} with respect to single monomer mass and termed the resulting parameter as the universal mass-mobility prefactor, K_{fm}, because it is independent of both the material type and aggregate monomer size. Henceforth, K_{fm} will be used instead of k_{fm} in the ensuing sections of this article. The scope of this study pertains to real-world, "unaged" combustion-generated aggregates occurring in the free molecular ($Kn > 10$) and the transition flow regimes. This chapter starts with a description of the numerical approach and concepts used for generating aggregates with known fractal morphologies and subsequently calculating their dm. Next, a section detailing our findings and the empirical relationships between the mass-mobility and structural parameters of aggregates follows. The article concludes with directions to future research needed on this topic.

3.2 Methods

Generation of three-dimensional (3D) fractal aggregates was done using *FracMAP*, a patented aerosol simulation package, which applies the particle-cluster aggregation technique. Detailed description of this package can be found in recent publications (Chakrabarty et al. 2009, 2011a,b). In brief, values of N, D_f, and k_f are specified by the user prior to generating an aggregate. The algorithm proceeds by randomly attaching two monomers in point-contact. Next, it adds new monomers sequentially to the dimer such that the resulting R_g of the new aggregate always satisfies Equation (3.1) for the user-specified values of D_f, and k_f. This process of monomer addition continues until the user specified N is generated. The algorithm next identifies all possible stable resting orientations of the aggregate by randomly rotating it in 3D space and checking whether for each orientation, the aggregate center of mass rests above the area projected by three or more contact points of the fractal aggregate (Chakrabarty et al. 2009). If the center of mass lies within the defined projected area, the particular orientation is deemed as "stable," and the algorithm proceeds to generate a pixelated two-dimensional (2D) projection image of the aggregate in that orientation. As a final step, the package analyzes the aggregate projected image for its 2D structural properties using various image-processing recipes. In this manner, *FracMAP* mimics the entire procedure from image generation to 2D structural characterization of aggregates as performed by aerosol experimentalists on electron micrographs of real-world particles using various image processing techniques (Chakrabarty et al. 2009). The d_m of a simulated aggregate can be determined from its projected area (A_{proj}) equivalent diameter using the following equation:

$$d_m = 2\sqrt{\frac{A_{proj}}{\pi}} \tag{3.3}$$

This approach is also known as the projected area approximation, which has been validated theoretically in the free-molecular regime (Sorensen 2011). The drag applied on an aggregate can be regarded as the collective effect of ballistic collision of gas molecules on it. Therefore, the probability of collision is proportional to the cross-sectional (projected) area of an aggregate in the direction of flow. In the transition regime, the accuracy of this approximation has also been repeatedly verified in various experimental studies (Rogak et al. 1993; Chakrabarty et al. 2007; Sorensen 2011; Eggersdorfer et al. 2012). Recently, Melas et al. (2015) reported the range of validity of this approximation in the transition regime using the concept of monomer Knudsen number ($Kn_a = \lambda/a$; not to be confused with Kn). They showed that for $Kn_a > 2$, the projected area approximation held reasonably accurate.

The simulation plan of this study is outlined in Table 3.1. Sets A, B, and C were run to investigate the influence of N, k_f, and d on d_m. For these three sets, D_f was fixed at 1.78 and d was varied from 10 to 40 nm. Each set comprised of seven subsets (A-1 to A-7) of simulation with N varying from 5 to 500. For each subset, k_f was varied from 1.0 to 2.5 in 0.3 increments, representative of the experimentally observed range of prefactor values for DLCA aggregates (projected) area (Koylu and Faeth 1995; Sorensen and Roberts 1997; Sorensen 2011). Sets D, E, and F were run with D_f varying from 1.68 to 1.88 in 0.5 increments. These sets were specifically designed to investigate the effect of D_f on D_{fm}. For each set, at least 1750 3D aggregates were generated with N chosen randomly between 5 and 500 for each aggregate. For each 3D aggregate generated, all possible stable orientations of the aggregate on a 2D plane were determined. Approximately 17,500 pixilated images of aggregates for each set were analyzed for 2D structural properties. The results of our statistical analysis are plotted using mean values and one standard deviation.

Table 3.1 Simulation plan

Set	Sub-set	Number of monomer, N	Monomer diameter, d (nm)	Fractal dimension, D_f	Fractal prefactor, k_f
A	A-1	5	10	1.78	1.0 - 2.5 (increment with 0.3)
	A-2	10			
	A-3	50			
	A-4	100			
	A-5	200			
	A-6	300			
	A-7	500			
B	B-1	5	20	1.78	1.0 - 2.5 increment with 0.3)
	B-2	10			
	B-3	50			
	B-4	100			
	B-5	200			
	B-6	300			
	B-7	500			
C	C-1	5	40	1.78	1.0 - 2.5 (increment with 0.3)
	C-2	10			
	C-3	50			
	C-4	100			
	C-5	200			
	C-6	300			
	C-7	500			

Set	Sub-set	Number of monomer, N	Monomer diameter, d (nm)	Fractal dimension, D_f	Fractal prefactor, k_f
D	D-1	5	10	1.68 - 1.88 (increment with 0.50)	1.3
	D-2	10			
	D-3	50			
	D-4	100			
	D-5	200			
	D-6	300			
	D-7	500			
E	E-1	5	20	1.68 - 1.88 (increment with 0.50)	1.3
	E-2	10			
	E-3	50			
	E-4	100			
	E-5	200			
	E-6	300			
	E-7	500			
F	F-1	5	40	1.68 - 1.88 (increment with 0.50)	1.3
	F-2	10			
	F-3	50			
	F-4	100			
	F-5	200			
	F-6	300			
	F-7	500			

3.3 Results and Discussion

3.3.1 Influence of monomer screening and fractal morphology

Apparent screening between monomers in a 3D aggregate is an important concept relating fractal aggregate morphology and mobility. Let us consider an imaginary 3D aggregate comprising N monomers of diameter d. If monomers were to be aligned in point-contact on a planar surface, the resulting aggregate would assume a 2D structure (similar to graphene). The projected area of this aggregate would reach its maximum possible value in this 2D planar configuration with zero apparent screening between monomers. The aggregate dm in this case would simply be $\sqrt{N}d$. Deviating from this ideal configuration, which is usually the case for real-world aerosols, an aggregate would always assume a d_m value smaller than $\sqrt{N}d$ In other words, non-zero screening between monomers would always ensure that the d_m of an aggregate does not reach its theoretical maximum limit ($\sqrt{N}d$). A convenient way to parameterize the monomer screening effect is to normalize the dm of an aggregate to its theoretical maximum, as shown in Equation (3.4):

$$\Phi = \frac{d_m}{\sqrt{N}d} \tag{3.4}$$

We denote Φ as the *apparent monomer screening factor*. The lesser the degree of monomer screening, the closer the value of Φ gets to unity (or, in other words, d_m approaches its theoretical maximum). The simple formulation in Equation (3.4) also reveals the collective influence of both the physical length scale an aggregate ($\sqrt{N}d$) and apparent screening between monomers (Φ) on the values of d_m. Once the value of Φ at a specified morphology (with fixed D_f, k_f, N, and d) is known, d_m could be readily calculated with the knowledge of their physical length scale represented by $\sqrt{N}d$.

Figure 3.2 shows the influence N and k_f on Φ for aggregates with values of d: (a) 10 nm, (b) 20 nm, and (c) 40 nm. The invariance of Φ with changing d is observed, because d_m is linearly proportional to d as per Equation (3.4). Increases in k_f and N were observed to influence Φ negatively. With increasing k_f, the shape of an aggregate becomes more isotropic or compact, thereby increasing the degree of screening between monomers. On the other hand, increasing N dictates more monomers being packed in a certain configuration governed by D_f. The probability of inter-monomer screen increases simply because more monomers are packed there. These long-range and small-scale effects of N and k_f, respectively, on the degree of apparent screening agree with previous observations (Sontag and Russel 1987; Melas et al. 2014a). At fixed N, the k_f of aggregates negatively correlates with d_m, which can be attributed to enhancement in monomer screening while the aggregate physical scale remains unchanged. At fixed k_f, N was observed to positively correlate with d_m. The effect of increasing physical scale due to increasing N outweighs the increasing monomer screening effects in an aggregate, resulting in the observed positive correlation. The empirical equations connecting Φ, d_m, N, k_f, and d (as predicted by our simulation results in Figure 3.2) are listed below in Equations (3.5a) and (3.5b):

$$\Phi = 1.046(\pm 0.012) k_f^{-0.083(\pm 0.013)} N^{-0.047(\pm 0.002)} \tag{3.5a}$$

$$d_m = 1.05 k_f^{-0.08} N^{0.45} d \tag{3.5b}$$

The uncertainty in the coefficients represents 95% confidence bound. One should note that Equations (3.5a) and (3.5b) are applicable for aggregates with D_f = 1.78.

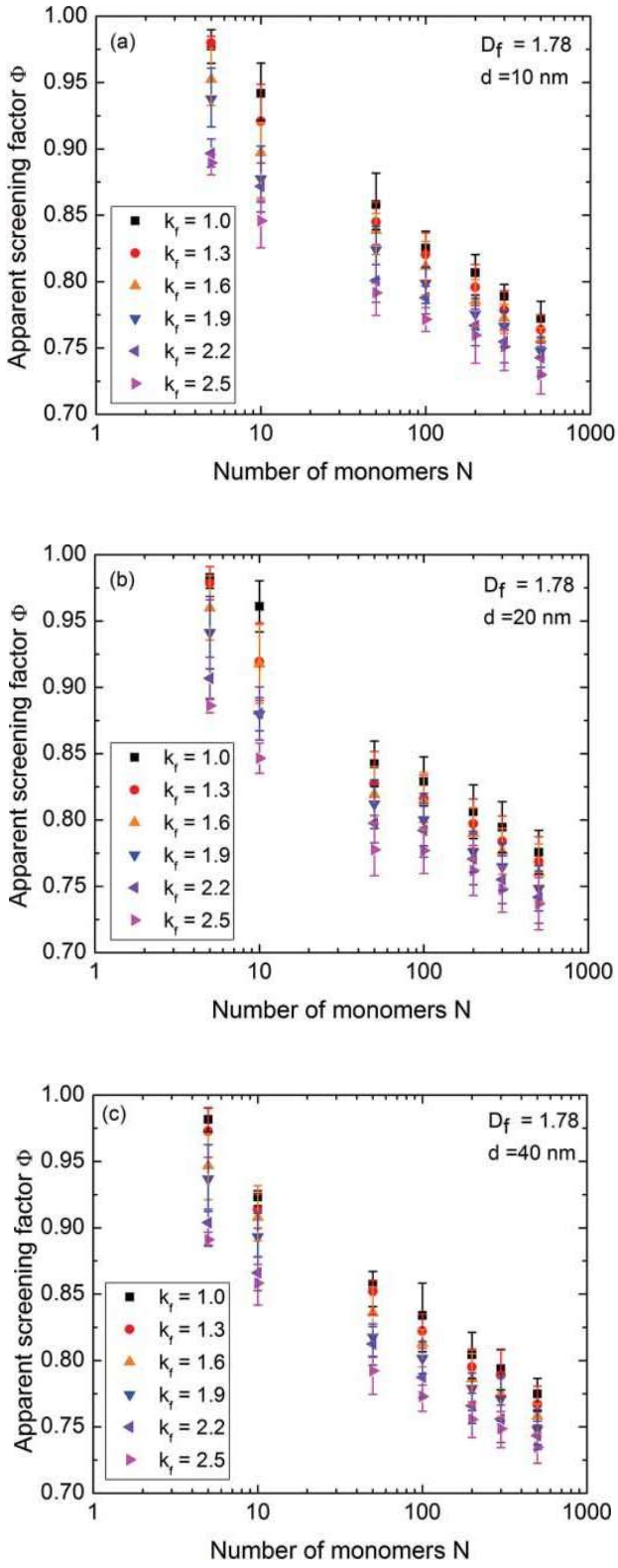

Figure 3.2. Apparent screening factor $\Phi = d_m/(N^{1/2}d)$ as a function of monomer number (N) and fractal prefactor (k_f) for aggregates with monomer diameters: (a) 10 nm, (b) 20 nm, and (c) 40 nm.

Aggregate D_{fm} and K_{fm} were estimated from the known fractal morphological parameters and mobility diameters using Equation (3.6), which is a rearranged form of Equation (3.2b):

$$\ln(N) = \ln\left(K_{fm}\right) + D_{fm}\ln\left(\frac{d_m}{d}\right) \tag{3.6}$$

Figure 3.3 shows the regression analysis with k_f varying from 1.0 to 2.5 and D_f varying from 1.68 to 1.88. Good linearity exists between ln(N) and ln(d_m/d) for the entire range of N. The slope (S) and the intercept (I) corresponding to D_{fm} and ln(K_{fm}) in Equation (3.6) were estimated. Figure 3.4 shows the K_{fm} values of aggregates with varying k_f and D_f. At a fixed D_f, a positive dependency between K_{fm} and k_f is clearly observed, which agrees with the findings of Melas et al. (2014b). At a fixed k_f, the relationship between K_{fm} and D_f is rather noisy and trivial: K_{fm} fluctuates approximately by ±3% around the average value. An empirical relationship between K_{fm} and k_f is proposed as:

$$K_{fm} = 0.850(\pm 0.024)k_f^{0.317(\pm 0.040)} \tag{3.7}$$

Figure 3.5 shows variations in D_{fm} with changing k_f and D_f. At a fixed k_f, by perturbing D_f from 1.68 to 1.88, an increase in D_{fm} is observed. What is not clear is the relationship between D_{fm} and k_f at a fixed D_f. We therefore conclude that the main effect on D_{fm} arises from changes in D_f rather than k_f. The range of D_{fm} also agrees with the experimentally found mean value of 2.2 (Sorensen 2011). The empirical relationship between D_{fm} and D_f is proposed as:

$$D_{fm} = 2.059(\pm 0.054)D_f^{0.143(\pm 0.045)} \tag{3.8}$$

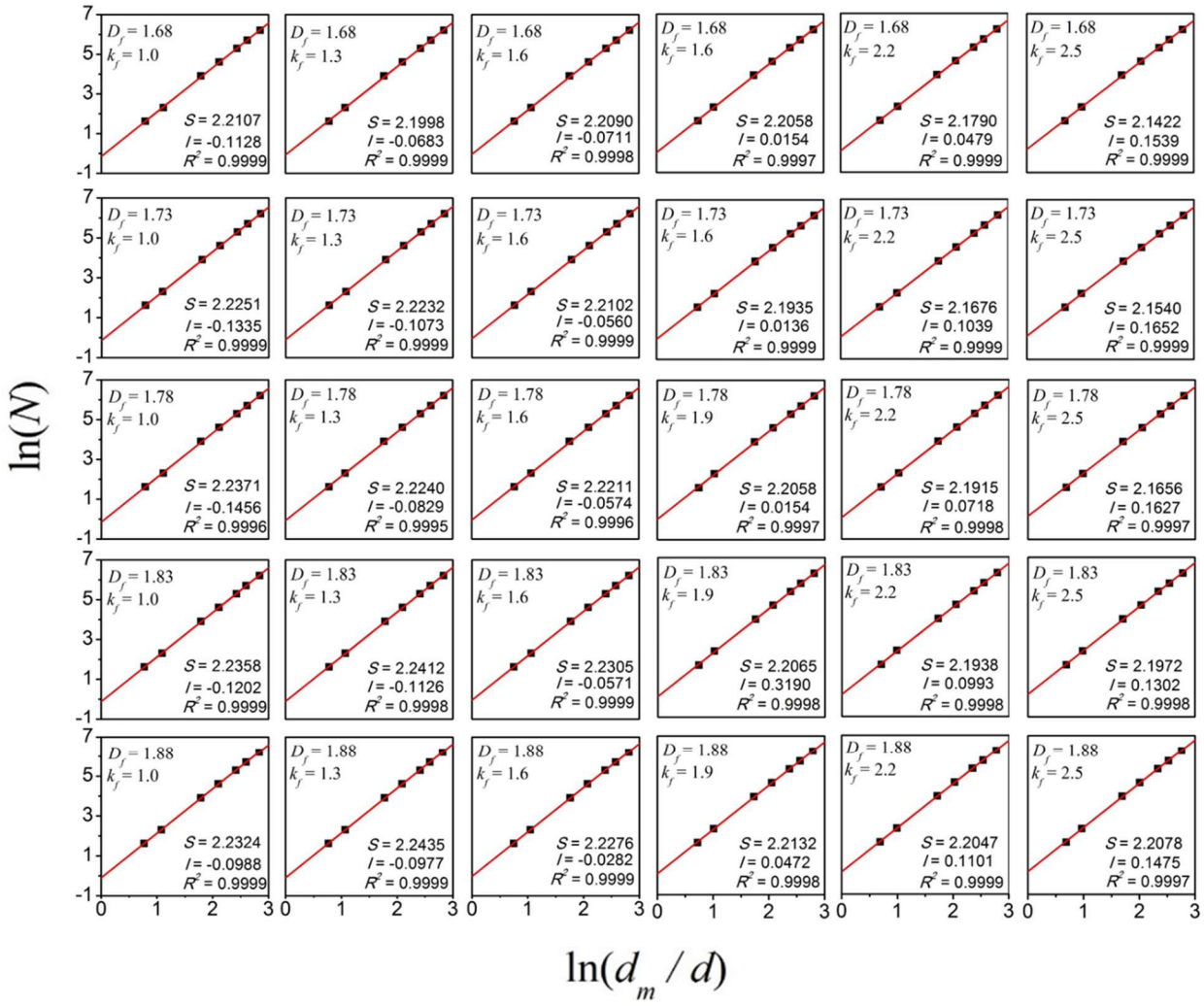

Figure 3.3. Linear regression analysis between ln(N) and ln(d_m/d) per Equation (3.6). S stands for slope, which corresponds to D_{fm}. I stands for intercept, which corresponds to ln(K_{fm}).

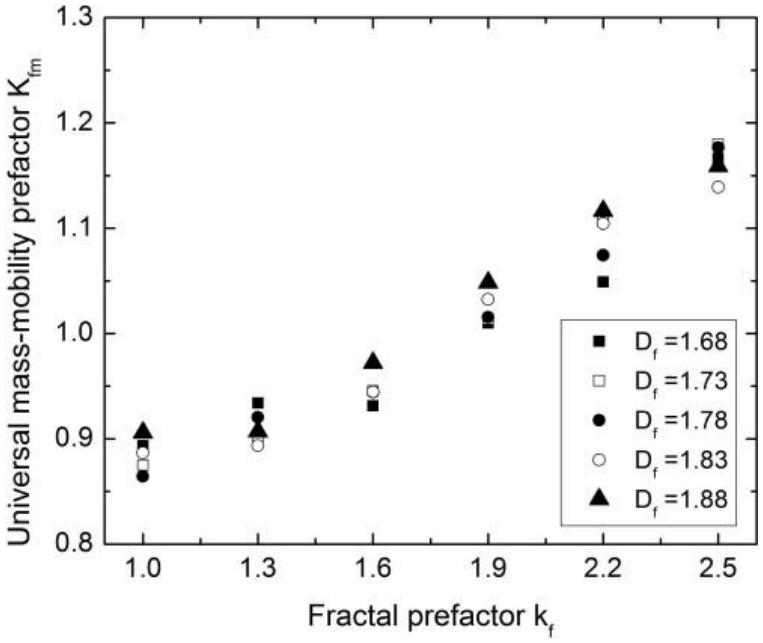

Figure 3.4. Dependency of aggregate K_{fm} on D_f and k_f.

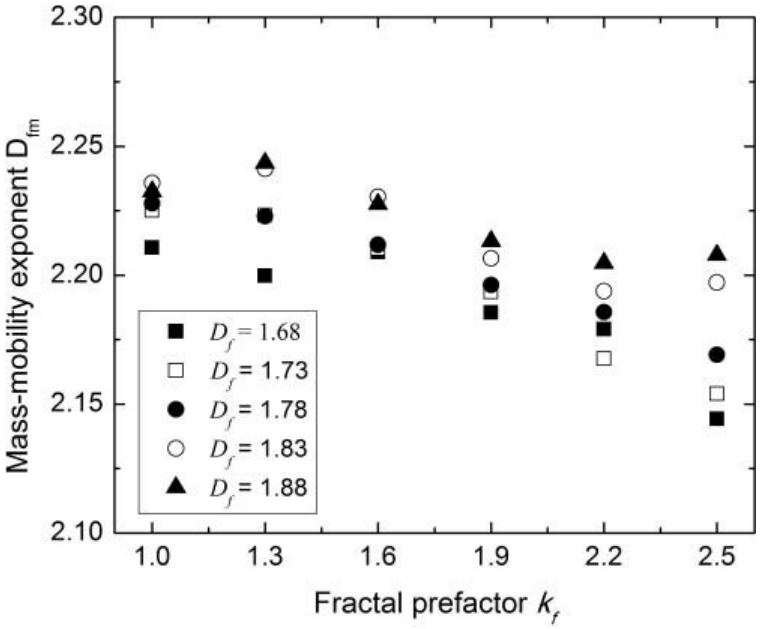

Figure 3.5. Dependency of aggregate D_{fm} on D_f and k_f.

3.3.2 Relationship between 2D and 3D *N*

A conventional approach to calculate *N* in 3D is by raising the estimated *N* in 2D (N_{proj}) to a power of 1.08, as shown in Equation (3.9a) (Brasil et al. 1999). Based on our simulation results, slight modifications were made to Equation (3.9a) by incorporating the role of k_f on N_{proj}. Variation in k_f influences the degree of apparent screening, which in turn influences the average vales of N_{proj}. The modified relation is shown in Equation (3.9b). The plots in Figure 3.6 compares the conventional (red solid line) and modified empirical form. The shaded area corresponds to the difference in estimated N in 3D. This difference becomes more pronounced with increasing N_{proj}. At a high k_f, the enhanced apparent screening effect should not be overlooked when predicting the *N* in 3D.

$$N = N_{proj}^{1.08} \tag{3.9a}$$

$$N = k_f^{0.10} N_{proj}^{1.08} \tag{3.9b}$$

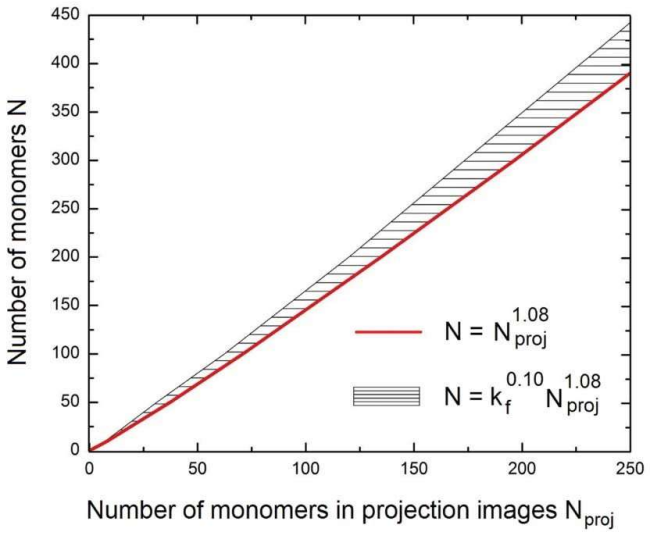

Figure 3.6. Comparison between conventional and corrected correlation factors for predicting *N* from N_{proj}. The range of k_f in the corrected correlation is varied between 1.0 and 2.5.

3.4 Conclusion

In this work, a numerical analysis was conducted to investigate the influence of fractal morphology of aggregates on their mass-mobility relationship. The scope of our study was set to encompass the range of fractal parameters encountered in aggregates generated via the DLCA mechanism, which best represents the formation of real-world aggregates. Empirical relationships were established between aggregate fractal morphological parameters D_f, k_f, N, and d, and their corresponding mass-mobility parameters d_m, D_{fm}, and k_{fm}. The dependency of aggregate d_m on k_f, N, and d was discussed using the concept of apparent screening between monomers. The effect on D_{fm} primarily originated from D_f than k_f. On the contrary, k_{fm} was found to be more sensitive to k_f than D_f. Positive dependency of D_{fm} on D_f and that of K_{fm} on k_f were observed.

The conventional bridging power-law exponent of 1.08 for predicting N from N_{proj} was shown to be inaccurate in the limits of large N and k_f. Correction to this bridging factor by taking into account large limit constraints was proposed. Future work needs to be in the direction of investigating the effects of inherent screening, resulting from inter-monomer sintering, on aggregate mass-mobility relationship.

3.5 References

Brasil, A., Farias, T. L., and Carvalho, M. (1999). A Recipe for Image Characterization of Fractal-Like Aggregates. *J. Aerosol Sci.,* 30:1379-1389.

Chakrabarty, R. K., Beres, N. D., Moosmüller, H., China, S., Mazzoleni, C., Dubey, M. K., Liu, L., and Mishchenko, M. I. (2014). Soot Superaggregates From Flaming Wildfires and their Direct Radiative Forcing. *Sci. Rep.,* 4:3.

Chakrabarty, R. K., Garro, M. A., Chancellor, S., Herald, C., and Moosmüller, H. (2009). FracMAP: An User-Interactive Package for Performing Simulation and Orientation-Specific Morphology Analysis of Fractal-like Solid Nano-Agglomerates. *Comput. Phys. Commun*., 180:1376-1381.

Chakrabarty, R. K., Garro, M. A., Garro, B. A., Chancellor, S., Moosmüller, H., and Herald, C. M. (2011a). Simulation of Aggregates with Point-Contacting Monomers in the Cluster-Dilute Regime. Part 1: Determining the Most Reliable Technique for Obtaining Three-Dimensional Fractal Dimension from Two-Dimensional Images. *Aerosol Sci. Tech.*, 45:75-80.

Chakrabarty, R. K., Garro, M. A., Garro, B. A., Chancellor, S., Moosmüller, H., and Herald, C. M. (2011b). Simulation of Aggregates with Point-Contacting Monomers in the Cluster-Dilute Regime. Part 2: Comparison of Two- and Three-Dimensional Structural Properties as a Function of Fractal Dimension. *Aerosol Sci. Tech*., 45:903-908.

Chakrabarty, R. K., Moosmüller, H., Arnott, W. P., Garro, M. A., Slowik, J. G., Cross, E. S., Han, J.-H., Davidovits, P., Onasch, T. B., and Worsnop, D. R. (2007). Light Scattering and Absorption by Fractal-like Carbonaceous Chain Aggregates: Comparison of Theories and Experiment. *Appl. Optics*, 46:6990-7006.

Chakrabarty, R. K., Moosmüller, H., Arnott, W. P., Garro, M. A., Tian, G., Slowik, J. G., Cross, E. S., Han, J.-H., Davidovits, P., and Onasch, T. B. (2009). Low Fractal Dimension Cluster-Dilute Soot Aggregates from a Premixed Flame. *Phys. Rev. Lett*., 102:235504.

Eggersdorfer, M. L., Kadau, D., Herrmann, H. J., and Pratsinis, S. E. (2012). Aggregate Morphology Evolution by Sintering: Number and Diameter of Primary Particles. *J. Aerosol Sci*., 46:7-19.

Friedlander, S. K. (2000). Smoke, Dust, and Haze. Oxford University Press, Oxford, UK.

Heinson, W., Sorensen, C. M., and Chakrabarti, A. (2010). Does Shape Anisotropy Control the Fractal Dimension in Diffusion-Limited Cluster–Cluster Aggregation? *Aerosol Sci. Tech*., 44:1-4.

Hyeon-Lee, J., Beaucage, G., Pratsinis, S. E., and Vemury, S. (1998). Fractal Analysis of Flame-Synthesized Nanostructured Silica and Titania Powders Using Small-Angle X-ray Scattering. *Langmuir*, 14:5751-5756.

Koylu, U. O., and Faeth, G. M. (1995). Optical Properties of Overfire Soot in Buoyant Turbulent Diffusion Flames at Long Residence Times. *Trans. ASME*, 116:152-159.

Melas, A. D., Isella, L., Konstandopoulos, A. G., and Drossinos, Y. (2014a). Morphology and Mobility of Synthetic Colloidal Aggregates. *J. Colloid Interf. Sci.*, 417:27-36.

Melas, A. D., Isella, L., Konstandopoulos, A. G., and Drossinos, Y. (2014b). Friction Coefficient and Mobility Radius of Fractal-like Aggregates in the Transition Regime. *Aerosol Sci. Tech*., 8:1320-1331.

Melas, A. D., Isella, L., Konstandopoulos, A. G., and Drossinos, Y. (2015). A Methodology to Calculate the Friction Coefficient in the Transition Regime: Application to Straight Chains. *J. Aerosol Sci*., 82:40-50.

McMurry, P. H., Wang, X., Park, K., and Ehara, K. (2002). The Relationship between Mass and Mobility for Atmospheric Particles: A New Technique for Measuring Particle Density. *Aerosol Sci. Tech*., 36:227-238.

Park, K., Kittelson, D. B., and McMurry, P. H. (2004). Structural Properties of Diesel Exhaust Particles Measured by Transmission Electron Microscopy (TEM): Relationships to Particle Mass and Mobility. *Aerosol Sci. Tech*., 38:881-889.

Rogak, S. N., Flagan, R. C., and Nguyen, H. V. (1993). The Mobility and Structure of Aerosol Agglomerates. *Aerosol Sci. Tech*., 18:25-47.

Scheckman, J. H., McMurry, P. H., and Pratsinis, S. E. (2009). Rapid Characterization of Agglomerate Aerosols by In Situ Mass-Mobility Measurements. *Langmuir*, 25:8248-8254.

Sonntag, R. C., and Russel, W. B. (1987). Structure and Breakup of Flocs Subjected to Fluid Stresses: II. Theory. *J. Colloid Interf. Sci*., 115:378-389.

Sorensen, C. (2001). Light Scattering by Fractal Aggregates: A Review. *Aerosol Sci. Tech*., 35:648-687.

Sorensen, C. (2011). The Mobility of Fractal Aggregates: A Review. *Aerosol Sci. Tech*., 45:765-779.

Sorensen, C. M., and Roberts, G. C. (1997). The Prefactor of Fractal Aggregates. *J. Colloid Interf. Sci*., 186:447-452.

Wang, G., and Sorensen, C. (1999). Diffusive Mobility of Fractal Aggregates over the Entire Knudsen Number Range. *Phys. Rev. E*, 60:3036

Chapter 4: Kinetics of Sol-to-Gel Transition in Irreversible Particulate Systems

The results of this chapter have been published in Liu, P., Heinson, W. R., Sorensen, C. M., Chakrabarty R. K. (2019). Kinetics of Sol-to-Gel Transition in Irreversible Particulate Systems. Journal of Colloid and Interface Science, 550, 57-63.

Abstract

A comprehensive theory encompassing the kinetics of the sol-to-gel transition is yet to be formulated due to break-down of the mean-field Smoluchowski Equation. Using high temporal-resolution Monte Carlo simulation of irreversible aggregation systems, we show that this transition has three distinct regimes with kinetic exponent $z \in [1, 2)$ corresponding to aggregation of sol clusters proceeding to the ideal gel point (IGP); $z \in [2, 5.7)$ for gelation of sol clusters beyond IGP; and $z \in [2, 3.5)$ for a hitherto unidentified regime involving aggregation of gels when monomer-dense. We further establish universal power-law scaling relationships that connect the kinetics of these three regimes. Improved parameterizations are performed on the characteristic timescale parameters that define each regime.

4.1 Introduction

Aggregation is a phenomenon ubiquitous in colloidal and aerosol systems (Hausdorff 1918; Forrest andWitten 1979; Sorensen 2011; Family and Landau, 2013; Brinker and Scherer 2013). Upon dispersion, particles collide and often irreversibly stick together to form larger clusters. Provided the monomer-monomer contact is non-coalescent, the aggregates manifest a scale-invariant, fractal-like morphology quantifiable with a mass fractal dimension (D_f) (Hausdorff 1918; Forrest andWitten 1979; Sorensen 2011; Sandkühler et al. 2003). Prolonged aggregation leads to the phenomenon of gelation – a process involving the jamming together of ramified aggregates and the formation of volume-spanning networks with a characteristic $D_f \approx 2.5$ (Sorensen et al. 1998; Sorensen and Chakrabarti 2011; Fry et al. 2002; Rottereau et al. 2004; Dhaubhadel et al. 2006). Gelation, as a phenomenon, has opened many avenues for synthesis of materials with unique properties (Brinker and Scherer 2013; Dhaubhadel et al. 2007; Chakrabarty et al. 2014a; Liu et al. 2015). The contemporary application of gelation theory extends to a broader context, for example, predicting the influence of wildfire emissions on climate change (Chakrabarty et al. 2014b; Kearney and Pierce 2012; Heinson and Chakrabarty 2016) and counteracting the formation of online extremist group supports (Manrique et al. 2018). Despite its wide-ranging applicability, the theory of gelation still grapples with the fundamental questions "*How fast does a sol system gel and what are the associated critical time scales?*" The difficulty in formulating a comprehensive kinetic theory stems from the break-down, at the onset of gelation, of the mean-field assumption which lies at the core of the governing Smoluchowski Equation (SE) (Sandkühler et al. 2003; Sorensen and Chakrabarti 2011; Fry et al. 2002; Rottereau et al. 2004; Friedlander 2000; Lattuada et al. 2003; Sandkühler et al. 2004). That is, SE, which tracks the time evolution of the system can only go so far in predicting the pre-onset of gelation, but not gelation

itself (Sorensen and Chakrabarti 2011; Fry et al. 2002). An alternate successful interpretation of the sol-gel phenomenon is the percolation theory, which is a static model and hence, cannot predict the kinetics (Stauffer 1976; DeGennes 1976; Stauffer et al. 1982). In this study, we address this long-standing problem by establishing a set of system-independent kinetic expressions capable of predicting the complete evolution of the sol-to-gel process. We do so by performing high temporal-resolution analysis on the evolution of diffusion limited cluster-cluster aggregation (DLCA) systems, which have been recently shown to produce gels that share identical morphologies with those produced via the percolation model (Heinson et al. 2017).

This chapter is organized as such: In 4.1.1 and 4.1.2, we briefly revisit the traditional interpretations of the gelation tendency and kinetics, respectively. Concepts regarding the critical conditions that define the transition regimes are introduced. In 4.2, we describe the numerical methods used in simulating the irreversible DLCA process. In 4.3, we present the main results of this study, along with discussion on the time-evolution of cluster mass distribution, the power-law scaling relationships of the transition kinetics, and important characteristic timescales. We conclude this paper with 4.4.

4.1.1 Tendency of sol-to-gel transition

The tendency of gelation stems from the simple fact that the D_f of non-coalescent aggregates is always smaller than the spatial dimension (d). For example, DLCA aggregates have a $D_f = 1.8$ in three-dimensional space ($d = 3$) (Sorensen and Chakrabarti 2011; Fry et al. 2002). As a result, when aggregates grow with $D_f < d$, the increase in their average size outruns their average nearest-neighbor separation. That said, the system inevitably evolves to crowded states (Sorensen and Chakrabarti 2011; Fry et al. 2002). When the total effective volume of all sol clusters reaches the

system volume (V), the system is said to reach ideal gel point (IGP) (Sorensen and Chakrabarti 2011; Dhaubhadel et al. 2007). Note that the effective cluster volume here is the perimeter volume (V_p), which could be visualized as volume of an isotropic sphere caging the cluster (Oh and Sorensen 1997). One should not be confused with the solid volume (V_m) of the cluster, which is the sum of the volumes of its constituent monomers. Visually, the IGP is the point at which sol clusters start to interdigitate (Sorensen and Chakrabarti 2011; Dhaubhadel et al. 2007), and it precedes the physical occurrence of the first gel cluster that spans the entire system volume. The point corresponding to the occurrence of such system-spanning gel is called physical gel point or percolation point (Sorensen and Chakrabarti 2011). Past research has also outlined other methods to identify the onset of gelation in aggregation systems. For example, the occurrence of gel can be experimentally determined by observing the appearance of non-zero elasticity (Sandkühler et al. 2004; Zaccone et al. 2009; Kroy et al. 2004). Theoretically, 1% of effective cluster volume fraction has also been shown as an indicator of imminent gelation (Heine and Pratsinis), consistent with the onset of the cluster-dense regime (Fry et al. 2002), beyond which the aggregation system deviates from the SE dynamics.

4.1.2 Kinetics of sol-to-gel transition

The existing kinetic theory discusses the sol-to-gel transition within two major regimes (Sorensen and Chakrabarti 2011; Fry et al. 2002; Rottereau et al. 2004; Sandkühler et al. 2004). Prior to IGP (hereafter Regime I), the transition is driven by the random collision and aggregation of particles that freely diffuse in system space, and the mean-field assumption holds valid (Sorensen and Chakrabarti 2011; Fry et al. 2002; Rottereau et al. 2004; Sandkühler et al. 2004); Beyond the IGP (hereafter Regime II), the free space in the system is largely taken, and as a result, the motion of clusters is significantly restricted. From this point on, the interconnection among neighboring sol

clusters starts to form, eventually leading to the onset of the gelling network (Sorensen and Chakrabarti 2011; Fry et al. 2002; Rottereau et al. 2004; Sandkühler et al. 2004). When all aggregates in the system are incorporated into one single volume-spanning particle, the system is said to reach final gel state (FGS) (Sorensen and Chakrabarti 2011).

The transition kinetics in Regime I is governed by the SE parameterized with aggregation kernels which depend on factors such as the relative motion between colliding particles and the cluster internal structure (Sandkühler et al. 2003; Sorensen and Chakrabarti 2011; Friedlander 2000). Solution to SE with homogeneous kernel leads to the scaling relationship between total number of clusters in the system (n_{tot}) and inverse time (t^{-1}), $n_{tot} \propto t^{-z}$, where the kinetics exponent (z) quantitatively measures how fast aggregation proceeds (Sorensen and Chakrabarti 2011; Fry et al. 2002; Oh and Sorensen 1997). Regime I is further divided into two sub-regimes – cluster-dilute and dense – per the value of z (Sorensen and Chakrabarti 2011): Cluster-dilute regime describes the initial aggregation stage, during which Brownian kernel holds, yielding $z = 1$ (Sorensen and Chakrabarti 2011; Fry et al. 2002; Oh and Sorensen 1997). Subsequently, the kinetics of aggregation tend to speed up as the system evolves to the cluster-dense regime, along with an increase in the value of z to about two near IGP (Sorensen and Chakrabarti 2011; Fry et al. 2002). A past theoretical modeling study found that the mean-field kinetics still holds valid although the kinetics is enhanced due to system crowding (Fry et al. 2002). This finding is in good agreement with later experiments conducted on a reaction-limited system, wherein the second order kinetics is observed to prevail, even in extremely dense system very close to the gel point (Sandkühler et al. 2004). The kinetic modeling in Regime II remains an active research direction. Fry et al. (2002) empirically mapped the values of increasing z with respect to t for the DLCA systems transitioning between IGP and FGS (i.e. the Post-IGP Regime). Rottereau et al. (2004) quantitated the late-stage

process using the concepts as evolution of connectivity between clusters. However, no explicit kinetic expression has been formulated for Regime II to our knowledge. Purely mathematical based analysis – an application of SE while disregarding the breaking down of mean-field assumption – has led to the advent of mathematical gelation (Van Dongen and Ernst 1985). Such a model, however, has been shown to ultimately fail on real world colloidal systems (Sandkühler et al. 2004). Lushnikov (2006) introduced a truncated model by immediately removing heavy particles (gels) with mass greater than a cutoff value, which reconciles the paradoxical behavior of SE, at a cost of violating mass conservation.

4.2 Methods

Our off-lattice DLCA model follows that introduced in previous publications (Heinson et al. 2017; Meakin 1984). The model algorithm starts out by generating a cubic simulation box with three million randomly placed monomers. The monomer volume fraction (f_{vm}) is controlled by specifying the V of the simulation box,

$$f_{vm} = \frac{4}{3}\pi a^3 \frac{n_{tot,0}}{V} \tag{4.1}$$

where a is a monomer radius in arbitrary units, and $n_{tot,0}$ denotes the total number of particle (cluster) at $t = 0$, which is equal to the conserved total number of monomers in the system. The simulation proceeds by randomly picking a cluster of mass N (number of constituent monomers, and $N = 1$ for monomer) and moving it by $2a$ in a random direction with probability N^{-1/D_f} per Stokes-Einstein diffusion (Friedlander 2000). The algorithm tracks the total number of clusters (n_{tot}), and once every n_{tot} clusters have been picked, t is incremented by unit simulation time t_s. We

define t_s as the time interval during which monomers move by a root-mean-squared-displacement of $2a$ (See Appendix II Section A2.1 for derivation):

$$t_s = \frac{4\pi\mu a^3}{k_B T} \tag{4.2}$$

where k_B, T, and μ respectively represent the Boltzmann constant, temperature, and viscosity of the surrounding gas (Friedlander 2000). During the process, if two clusters collide, they are joined together forming a new cluster, and n_{tot} decreases by one. The above procedure was repeated until $n_{tot} = 1$, that is, the FGS was attained, and the corresponding time was deemed t_{FGS}. By the end of each run, the algorithm outputted a list for cluster N for every t that incremented by t_s in the range between 0 and t_{FGS}. We next calculated, from the list, the cluster mass frequency distribution (hereafter, mass distribution), written as $n(\log_{10}N, t/t_s)/n_{tot}(t/t_s)$, where n denotes the number of clusters having N monomers at time t.

4.3 Results and Discussion

4.3.1 Evolution of cluster mass distribution

Figure 4.1 shows the contour plots of aggregate mass distributions in the $\log_{10}N - t/t_s$ space for systems of various f_{vm}. Panel (a) demonstrates the mean-field growth of sol clusters which is typically seen in Regime I, during which the kinetics could be described with the exact solution to SE (Sorensen and Chakrabarti 2011; Fry et al. 2002; Friedlander 2000; Oh and Sorensen 1997). Next, we discuss the onset of gelation and the subsequent Regime II by comparing the cluster mass

distributions with the analytical solution values of average cluster mass at the IGP (written as N_{IGP}):

$$N_{IGP} = k_f\left(R_{g,IGP}/a\right)^{D_f} \tag{4.3a}$$

$$\text{with } R_{g,IGP} = a\left[f_{vm}^{-1}k_f\left(\frac{D_f}{D_f+2}\right)^{3/2}\right]^{1/(3-D_f)} \tag{4.3b}$$

where $R_{g,IGP}$ is the average radius of gyration (a linear size) of aggregates at the IGP and k_f is the fractal prefactor in the scaling relation. Eq. (4.3a) follows mass scaling power-law relationship with $k_f = 1.3$ and $D_f = 1.8$ describing the morphology of DLCA. Eq. (4.3b), originally introduced in Ref. (Fry et al. 2004), is reached when one equalizes the system V to the total cluster V_P.

Panel (b)–(e) show that when sol clusters grow, their geometric mean mass value, represented by $\langle \log_{10} N \rangle$ (red dashed lines), asymptotes to the $\log_{10} N_{IGP}$ value (red solid lines) predicted by Eq. (4.3a). Subsequently, the IGP could be identified at the point where $\langle \log_{10} N \rangle$ reaches $\log_{10} N_{IGP}$ (See Appendix II, Section A2.2 for more detail), and the corresponding time is regarded as the ideal gel time (t_{IGP}). In Figure 4.1 we mark the IGP at the points ($N = N_{IGP}$; $t = t_{IGP}$) using triangle symbols. One could observe (in Fig. 4.1(b)–(e)) that immediately after IGP, the mass distribution becomes bimodal, indicating the onset of a separate phase, the gel. Subsequently, the gel clusters in the systems continuously grow by scavenging the remaining sol clusters whose mass distribution stays invariant with $\langle \log_{10} N \rangle$ closely matching $\log_{10} N_{IGP}$.

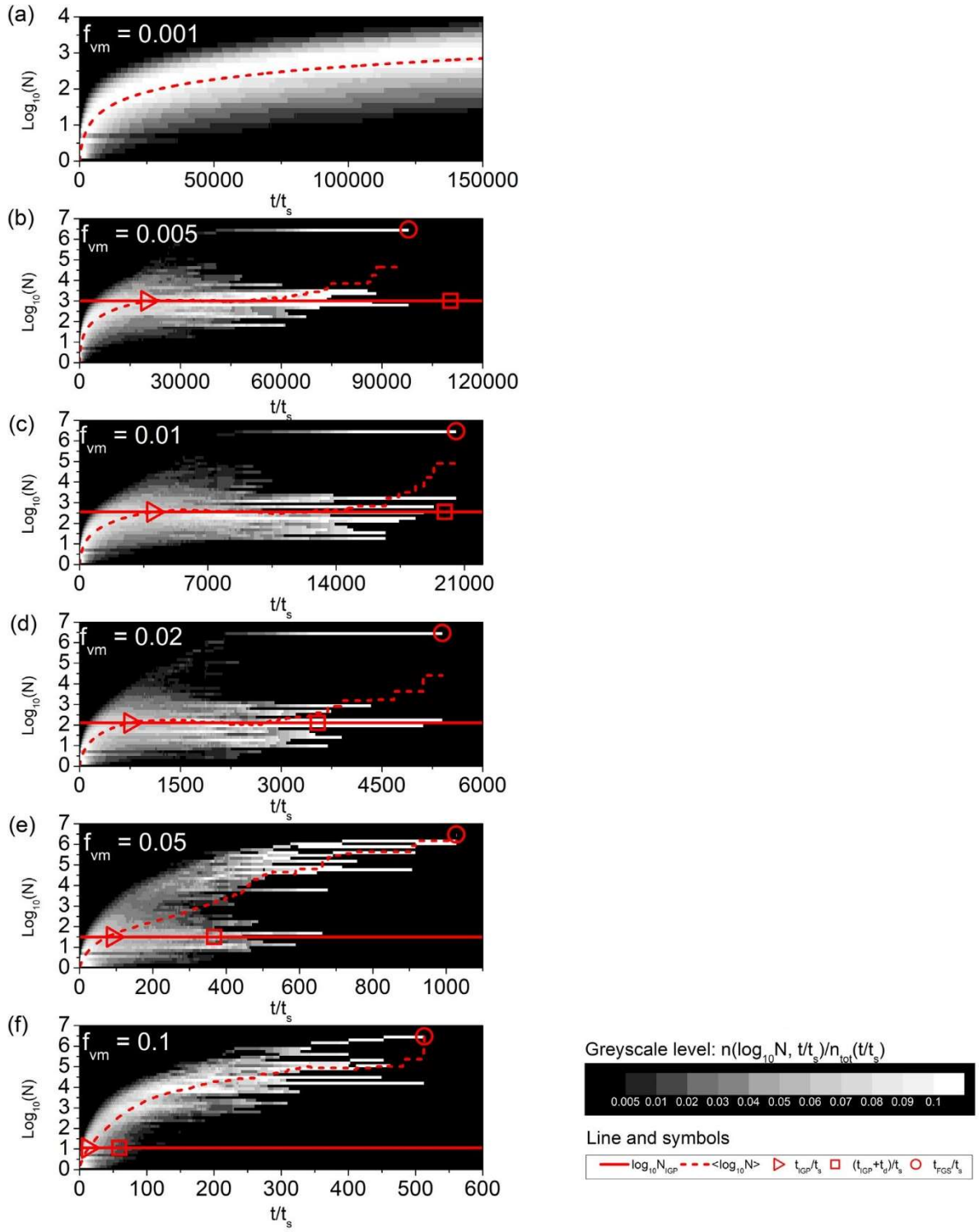

Figure 4.1. Time-evolution of the aggregate mass distribution for DLCA systems with f_{vm} = 0.001 (a), 0.005 (b), 0.01 (c), 0.02 (d), 0.05 (e), and 0.1 (f). The solid lines represent the analytical solution values to the characteristic cluster mass at the IGP, $\log_{10}N_{IGP}$, which follows Eq. (4.3). The dashed lines represent the geometric mean values of cluster mass, $<\log_{10}N>$. In panels (b)–(f), triangles and circles, respectively represent t_{IGP} and t_{FGS}, which are determined from the simulations. Squares indicate the time when sol clusters deplete, $t_{IGP} + t_d$, and t_d is solved using Eq. (4.4). All timescales are presented in units of t_s.

Another important observation from the evolution of mass distribution is that beyond IGP, a considerable amount of time is always needed for the total conversion of sol clusters to gel phase, as shown in Figure 4.1. We next discuss how to quantify the length of the time interval between IGP and the total conversion of sol clusters, which is written as t_d in the context of this paper. Recall that IGP is the point where the perimeter volume fraction of sol clusters reaches unity (Sorensen and Chakrabarti 2011; Fry et al. 2004). Such a condition, however, does not guarantee the immediate formation of the interconnection among neighboring sol clusters (hence t_d exists). This seemingly contradictory observation can be explained by the fact that fractal clusters only partially fill the Euclidean space. In other words, free spaces within the V_p always exist, so that the neighboring sol clusters at IGP could remain interdigitating, instead of forming connections (such configuration is qualitatively described by the schematic diagram in Fig. 4.2). Quantitatively, we measure the free spaces with $V_{p,IGP} - V_{m,IGP}$ (subscripts indicating parameters at IGP). This volume difference, when raised to power of 2/3, yields a square of a length scale whose square root approximately measures the average distance by which clusters need to travel in order to connect with their neighbors. Write the diffusivity of cluster at IGP as D_{IGP}, and the rearrangement of diffusion equation in three dimensional space yields to $t_d = \frac{(V_{p,IG} - V_{m,IGP})^{2/3}}{6D_{IGP}}$. We show a step-by-step derivation in Appendix II Section A2.3 that t_d, after being normalized by t_s, is a function of f_{vm} only, written as:

$$\frac{t_d}{t_s} = \frac{1}{4}\left[\frac{4}{3}\pi(1 - f_{vm})\right]^{\frac{2}{3}}\left(\frac{D_f}{D_f + 2}\right)^{(2D_f+3)/(6-2D_f)}\left(k_f f_{vm}^{-1}\right)^{3/(3-D_f)} \tag{4.4}$$

In Figure 4.1 we mark the critical points corresponding to the total conversion of sol clusters at ($N = N_{IGP}$, $t = t_{IGP} + t_d$) using square symbols. Good agreements between the predictions by Eq. (4.4)

and the simulations are seen for systems with different f_{vm}. Note that t_d is always inversely related to the f_{vm}. Qualitatively, this is because a denser system (with higher f_{vm}) reaches IGP with average sol clusters of smaller mass N_{IGP}, which are in turn characterized with smaller $V_{p,IGP}$ - $V_{m,IGP}$, and simultaneously larger D_{IGP}. One could also observe such inverse correlation between t_d and f_{vm} in Figure 4.1(b)-(e). For example, when a system is sufficiently dilute (f_{vm} = 0.005 and 0.01), the total conversion of sol clusters occurs at a timescale comparable to that of the FGS, formally written as $t_{IGP} + t_d \approx t_{FGS}$. With a further increase in f_{vm} (from 0.02 to 0.05), t_d decreases, the total conversion of sol clusters precedes FGS, and the time interval between $t_{IGP} + t_d$ and t_{FGS} becomes non-trivial. Such tendency reaches an extremity when f_{vm} = 0.1, as shown in Figure 4.1(f), where $t_{IGP} + t_d << t_{FGS}$ and the system evolves with a unimodal cluster mass distribution throughout the entire process. This unimodality implies that sol clusters and gels no longer coexist. For these extremely dense systems (f_{vm} = 0.05 and 0.1), the transition process beyond the $t_{IGP} + t_d$ is defined as Regime III, which differs fundamentally from the classical picture of sol-to-gel transition observed in monomer dilute systems (Sorensen and Chakrabarti 2011)

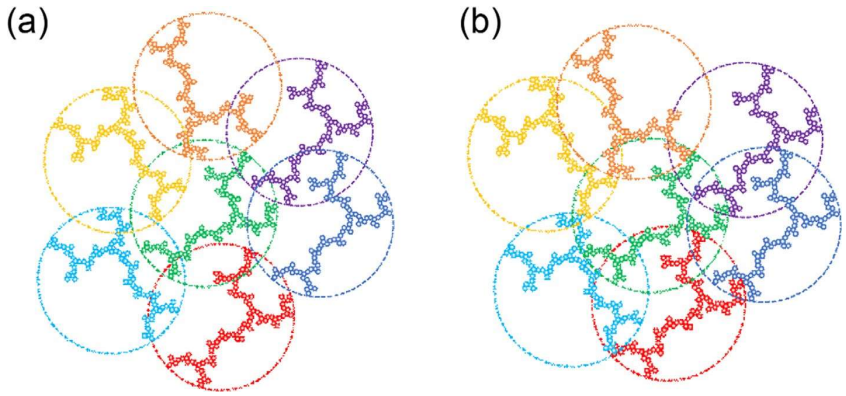

Figure 4.2. Schematic diagrams showing the interdigitating (a) and connected (b) fractal clusters. Individual clusters are colored differently. Dashed circle represents the effective volume of the clusters. In (a), fractal clusters highly interdigitate. Although the effective volume of clusters saturates the system, connections among clusters are not guaranteed. In this case, clusters could still move around freely until they connect with their neighbors. (b) shows the condition at which all clusters are connected, resulting in the onset of gel.

4.3.2 Scaling law for aggregation and gelation kinetics

We next demonstrate that the kinetics within Regimes I, II and III could be unified on coherent power-law relationships, when the transition is observed with two timescales, first, the characteristic time for Brownian aggregation (t_c), and second, the t_{IGP} introduced in previous paragraphs. In Regime I, solving SE with homogeneous Brownian kernel provides the scaling law parameterized with z = 1 (Sorensen and Chakrabarti 2011; Friedlander 2000):

$$\frac{n_{tot}}{n_{tot,0}} = \left(1 + \frac{t}{t_c}\right)^{-1} \tag{4.5}$$

$$\text{and } t_c = \frac{3\mu V}{4k_B T n_{tot,0}} \tag{4.6}$$

According to Eq. (4.5) we empirically determine t_c from DLCA simulations at the time when n_{tot} decreases to half of the initial values (Refer to Appendix II Section 2.4 for more details).

Figure 4.3(a) shows that when t is normalized per $1 + t/t_c$, the early stages of the transition are unified and the trends of $n_{tot}/n_{tot,0}$ follow Eq. (4.5) with z = 1, indicating that the Brownian aggregation mechanism prevails. This is especially true for f_{vm} = 0.001, whereas the behavior becomes more rapid than Eq. (4.5) for progressively larger f_{vm}. This deviation from Eq. (4.5) indicates subsequent cluster-dense conditions, and the kinetics speed up with the kinetic exponent z taking on values larger than unity, during which the driving mechanism of aggregation becomes ballistic-limited as the interdigitating aggregates have no more free space to diffuse (Sorensen and Chakrabarti 2011; Fry et al. 2002; Liu et al. 2018).

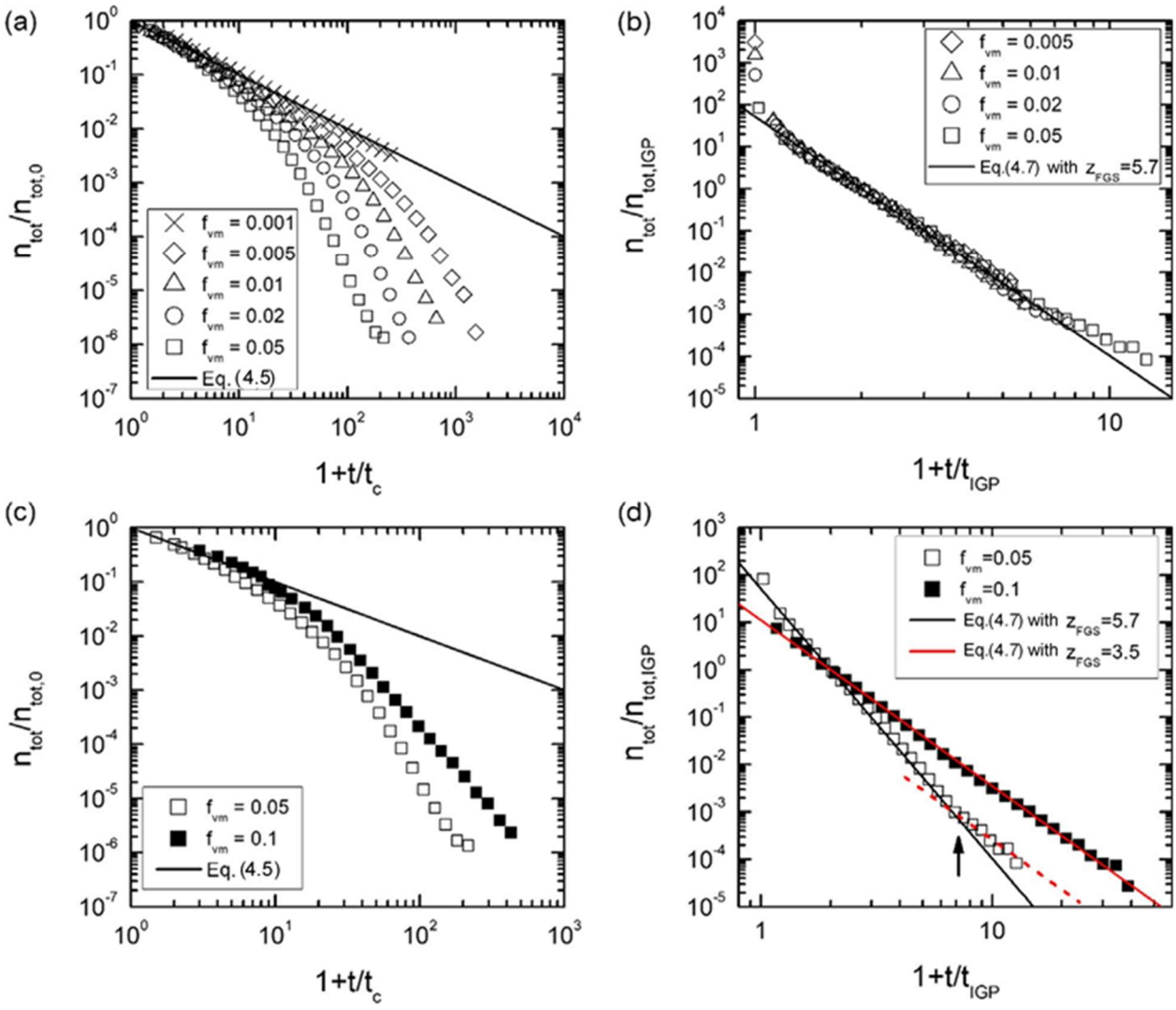

Figure 4.3. (a) and (c) show that early stages of aggregation are unified by Eq. (4.5) when observed with normalized time $1 + t/t_c$. (b) and (d) show that the late stages of transitions, when observed with normalized time $1 + t/t_{IGP}$, are unified by Eq. (4.7). Dashed line in (d) has a slope of about 3.5, and the arrow indicates an inflection in transition kinetics.

Figure 4.3(b) shows that the late stages of the transition are unified upon normalizing t according to $1 + t/t_{IGP}$. A universal power-law relationship manifests as,

$$\frac{n_{tot}}{n_{tot,IGP}} = 2^{z_{FGS}} \left(1 + \frac{t}{t_{IGP}}\right)^{-z_{FGS}} \tag{4.7}$$

where $z_{FGS} \approx 5.7$ is the kinetic exponent reported at the FGS (Fry et al. 2002). The z takes on a terminal value because only when $t >> t_{IGP}$ (that is, a condition approaching FGS) could Eq. (4.7) be reduced to $n_{tot} \propto t^{-z}$. The prefactor, taking up the expression of $2^{z_{FGS}}$, satisfies $n_{tot} = n_{tot,IGP}$ when $t = t_{IGP}$. The two power-law relationships, Eq. (4.5) and the new Eq. (4.7) provide a complete description for the full so-to-gel transition within regimes I and II.

Regime III occurs in system $f_{vm} = 0.1$ with a counterintuitively slower kinetics. Figure 4.3(c) shows that the decrease in $n_{tot}/n_{tot,0}$ for $f_{vm} = 0.1$ falls behind that for $f_{vm} = 0.05$. When observed with $1 + t/t_{IGP}$, a less steep decreasing trend of $n_{tot}/n_{tot,IGP}$ is seen (Panel(d)) when $f_{vm} = 0.1$. Eq. (4.7) still holds valid while a $z_{FGS} \approx 3.5$ fits the data best, per the red solid line in panel (d). This slower rate – in a denser system – could be due to the abundance gel clusters which are considerably less mobile. Qualitatively speaking, the extremely dense system facilitates almost an instantaneous gelation of sol clusters, but the resultant abundance of gels slows down the system progressing from IGP to FGS. Figure 4.3(d) shows that the decreasing trend of $n_{tot}/n_{tot,IGP}$ for the system with $f_{vm} = 0.05$ originally follows Eq. (4.7) with $z_{FGS} \approx 5.7$ until reaching an inflection point indicated by the arrow in (d). Beyond the inflection, the trend asymptotes to the less steep one governed by $z_{FGS} \approx 3.5$. Note that this inflection occurs approximately at $t_{IGP} + t_d$ of the system (see Fig. 4.1(e)), indicating that a slowing down of kinetics is indeed a characteristic of the system in which only gel clusters exist. These dense gelation systems near $f_{vm} = 0.1$ are traditionally discussed in the framework of static percolation and thermodynamics (Stauffer 1976; DeGennes 1976; Stauffer et al. 1982; Heinson et al. 2017) and here we emphasize that the kinetic aspect should not be overlooked.

4.3.3 Improved parameterization on characteristic timescales

We next evaluate the existing analytical expressions for the important characteristic timescales that are involved in the sol-to-gel transition process. Combining Eq. (4.6) with (4.1) and (4.2) yields the analytical expression for t_c in units of t_s:

$$\frac{t_c}{t_s} = \frac{1}{4} f_{vm}^{-1} \tag{4.8}$$

Figure 4.4 compares the prediction of Eq. (4.8) with the t_c/t_s determined from simulations. The exponent -1 fails at large f_{vm}, indicating that the aggregation in these extremely dense systems deviates from the Brownian kernel at a very early point. The enhanced kinetics lead to the t_c being smaller than what Eq. (4.8) predicts. The upper limit for f_{vm} is the percolation threshold, at which point the volume-spanning gel is instantaneously formed, and so that both t_c and t_{IGP} decrease to zero. Ref. (Powell 1979) reports the critical volume fraction (Φ_P) to be about 0.18 (black line in Fig. 4.4) at which a system of randomly packed hard spheres reaches percolation threshold in three-dimensional space. We introduce a semiempirical expression of t_c for the dense DLCA systems near the percolation threshold as:

$$\frac{t_c}{t_s} = \frac{1}{4} (f_{vm}^{-1} - \Phi_P^{-1}) \tag{4.9}$$

The prediction by Eq. (4.9) is plotted in Figure 4.4 and it captures the dramatic decrease in the t_c/t_s near Φ_P. Similarly, we provide an improved parameterization of t_{IGP} for these dense DLCA systems,

$$\frac{t_{IGP}}{t_s} = \frac{1}{4} (f_{vm}^{-1} - \Phi_P^{-1}) \left[b^{-\frac{1}{z}} f_{vm}^{\frac{D_f}{(D_f-3)z}} \left(\frac{D_f}{D_f+2} \right)^{\frac{3D_f}{(6-2D_f)z}} k_f^{\frac{3}{(3-D_f)z}} - 1 \right] \tag{4.10}$$

where b originates from a power-law relationship $\langle N \rangle = b(1 + t/t_c)^z$ quantifying the aggregate growth when cluster-dense condition sets in (Oh and Sorensen 1997). The step-by-step derivation of Eq. (4.10) is outlined in Appendix II Section A2.5. The determination of the values for b and z from DLCA is discussed in Section A2.6. Figure 4.4 also compares the prediction of Eq. (4.10) (solved with $D_f = 1.8$, $k_f = 1.3$, $z = 1.5$ and $b = 0.2$) to the t_{IGP}/t_s determined from simulations.

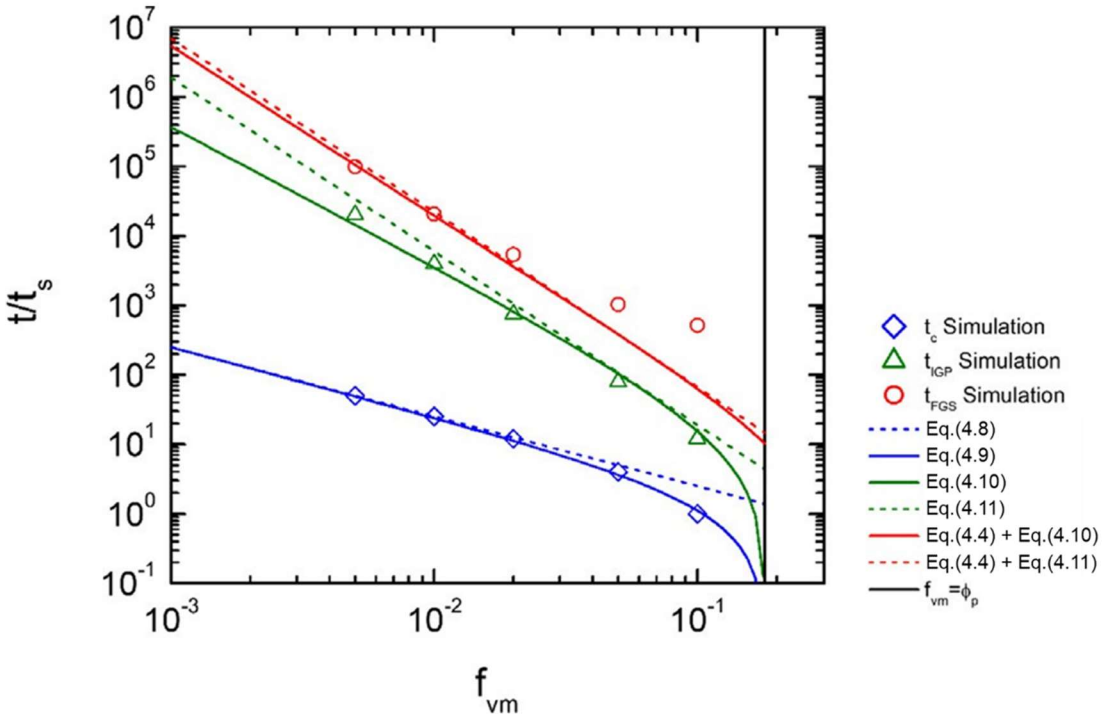

Figure 4.4. Characteristic timescales t_c, t_{IGP} and t_{FGS} as functions of f_{vm}. The timescale parameters determined from DLCA simulations are compared with their analytical solution values.

The traditionally used expression (Sorensen and Chakrabarti 2011; Dhaubhadel et al. 2007) for t_{IGP} is also evaluated here: $t_{IGP} \approx a^3 K^{-1} f_{vm}^{-2.5}$, which after being combined with Eq. (4.2) yields to:

$$\frac{t_{IGP}}{t_s} = \frac{3}{16\pi} f_{vm}^{-2.5} \tag{4.11}$$

Figure 4.4 shows that Eq. (4.11) overestimates t_{IGP} by a factor less than two.

The summation of Eq. (4.10) (or (4.11)) and (4.4) provide analytical solution values for (t_{IGP} + t_d)/t_s, which are compared with the t_{FGS}/t_s determined from simulations. We again observe that a dilute system reaches FGS when the total conversion of sol clusters is attained ($t_{IGP} + t_d \approx t_{FGS}$), but when monomer dense, the time interval between $t_{IGP} + t_d$ and t_{FGS} becomes significant, during which regime III takes over the kinetics.

Figure 4.4 and Eqs. (4.4), (4.8)-(4.11) also show that the timescale parameters – t_c ,t_{IGP}, and t_d – are functions of f_{vm} only. Those parameters are scale independent. Their values are not sensitive to changes in system size V, as long as f_{vm} is fixed. Note that the parameters, n_{tot} and t_{FGS}, however, are scale dependent. Their values are sensitive to system size and hence they are functions of both f_{vm} and V. We show in Appendix II Section A2.7 that $n_{tot} \propto V$, and $t_{FGS} \propto V^{1/z_{FGS}}$. The dependence of t_{FGS} on V is rather insignificant when system is dilute, because z_{FGS} takes a value as large as 5.7. The influence of system scale becomes pronounced when system is dense. At last, we need to emphasize that the entire discussion of scale-independence is built upon an important prerequisite – that the system should be at least large enough, such that for any given f_{vm}, the $n_{tot,0}$ is always much larger than N_{IGP}. This condition guarantees that statistically significant number of clusters exist in the system beyond IGP.

4.4 Conclusion

We conclude the chapter with Figure 4.5 which schematically illustrates the comprehensive picture. The transition Regimes I-III and the corresponding kinetic formulations (Eqs. (4.5) and (4.7)) are presented with the characteristic timescales, t_c, t_{IGP}, and $t_{IGP} + t_d$ serving as milestones.

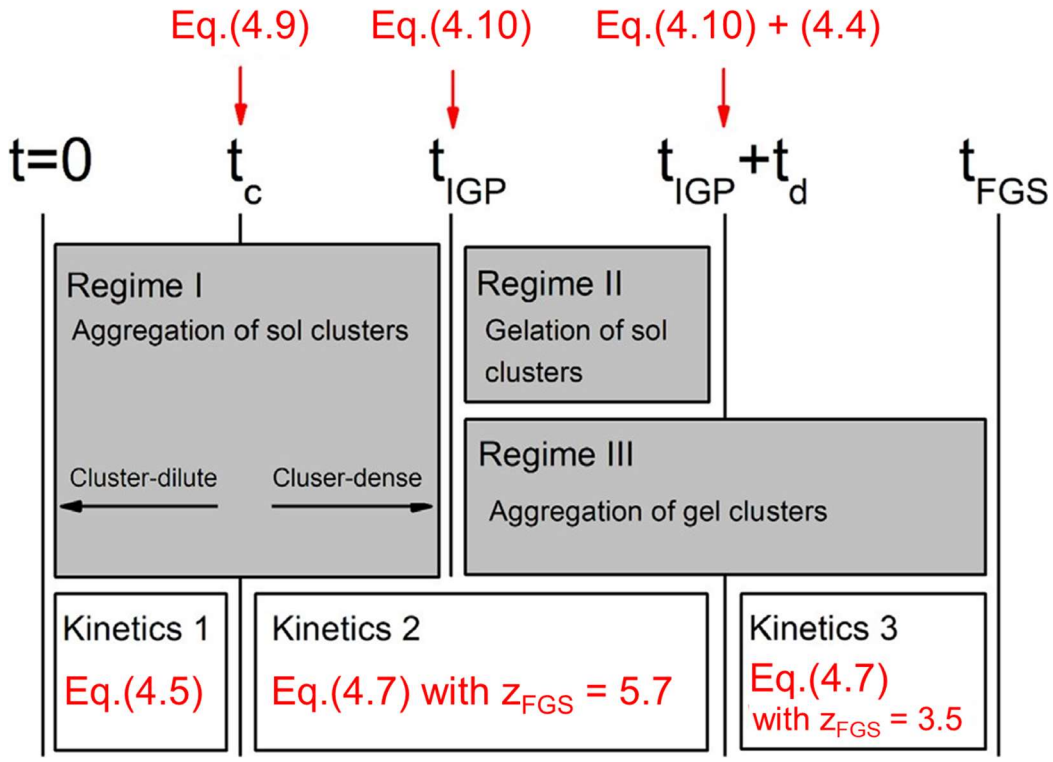

Figure 4.5. The kinetics of full sol-to-gel transition

Please note that the regime I and II are separated per t_{IGP} at which point SE breaks down, but kinetics 1 fails at $t \approx t_c$, the time at which Brownian aggregation kernel no longer holds valid (the cluster-dense condition sets in) (Sorensen and Chakrabarti 2011; Fry et al. 2002). Regime II and III start out simultaneously at IGP, but II tends to dominate over III because number of gel clusters in a system is typically negligible compared to that of the sol clusters. Regime III only takes

precedence after II reaches its completion, that is $t_{IGP} + t_d < t < t_{FGS}$, which only manifests when monomer dense. The latest study (Heinson et al. 2018) on the gelation in DLCA system with f_{vm} = 0.1 reveals a breakdown of the invariance between the mass and surface fractal dimension values for monomer-dense gels. This observation indicates that Regime III is indeed a distinct transition process, regarding both kinetics and the morphologies of resultant gel particles. Future research on this topic should be directed toward experimental studies on the late-stage Regime III in the dense aggregation systems, with an emphasis placed on the kinetic perspective. Another interesting topic for future research is to investigate the gelation kinetics in the systems with f_{vm} varying as a function of t. For example, changing system V as aggregation proceeds, which has been shown critical in studying more realistic aggregation systems with polydispersed constituent monomers (Goudeli et al. 2016).

4.5 References

Brinker, C. J., and Scherer G. W. (2013) Sol-Gel Science: The Physics and Chemistry of Sol-Gel Processing, Academic Press, New York, USA.

Chakrabarty, R. K., Novosselov, I. V., Beres, N. D., Moosmüller, H., Sorensen, C. M., Stipe, C. B. (2014a) Trapping and Aerogelation of Nanoparticles in Negative Gravity Hydrocarbon Flames. *Appl. Phys. Lett.*, 104:243103.

Chakrabarty, R. K., Beres, N. D., Moosmüller, H., China, S., Mazzoleni, C., et al. (2014b) Soot Superaggregates from Flaming Wildfires and Their Direct Radiative Forcing. *Sci. Rep.*, 4:5508.

DeGennes, P. G. (1976) On a Relation between Percolation Theory and the Elasticity of Gels. *J. Phys. Lett. Paris*, 37:1–2.

Dhaubhadel, R., Pierce, F., Chakrabarti, A., and Sorensen, C. M. (2006) Hybrid Superaggregate Morphology as a Result of Aggregation in a Cluster-Dense Aerosol. *Phys. Rev. E*, 73:011404.

Dhaubhadel, R., Gerving, C. S., Chakrabarti, A., and Sorensen, C. M. (2007) Aerosol Gelation: Synthesis of a Novel, Lightweight, High Specific Surface Area Material. *Aerosol Sci. Technol.*, 41:804–810.

Family, F., and Landau, D. P. (1984) Kinetics of Aggregation and Gelation, Elsevier, Massachusetts, USA.

Forrest, S. R., and Witten Jr. T. A. (1979) Long-Range Correlations in Smoke-Particle Aggregates. *J. Phys. A*, 12:L109.

Friedlander, S. K. (2000). Smoke, Dust, and Haze. Oxford University Press, Oxford, UK.

Fry, D., Sintes, T., Chakrabarti, A., and Sorensen, C. M. (2002) Enhanced Kinetics and Free-Volume Universality in Dense Aggregating Systems. *Phys. Rev. Lett.*, 89:148301.

Fry, D., Chakrabarti, A., Kim, W., and Sorensen, C. M. (2004) Structural Crossover in Dense Irreversibly Aggregating Particulate Systems. *Phys. Rev. E*, 69:061401.

Goudeli, E., Eggersdorfer, M. L., and Pratsinis S. E. (2016) Coagulation of Agglomerates Consisting of Polydisperse Primary Particles. *Langmuir* 32:9276–9285.

Hausdorff, F. (1918) Dimension und äußeres Maß. *Math. Ann.*, 79:157–179.

Heine, M. C., and Pratsinis, M. C. (2007) Brownian Coagulation at High Concentration. *Langmuir* 23:9882–9890.

Heinson, W. R., and Chakrabarty, R. K. (2016) Fractal Morphology of Black Carbon Aerosol Enhances Absorption in the Thermal Infrared Wavelengths. *Opt. Lett.*, 41:808–811.

Heinson, W. R., Chakrabarti, A., and Sorensen, C.M. (2017) Kinetic Percolation. *Phys. Rev. E*, 95:052109.

Heinson, W. R., Liu, P., and Chakrabarty, R. K. (2017) Fractal Scaling of Coated Soot Aggregates. *Aerosol Sci. Technol*., 51:12–19.

Heinson, W. R., Heinson, Y. W., Liu, P., and Chakrabarty, R. K. (2018) Breakdown of Fractal Dimension Invariance in High Monomer-Volume-Fraction Aerosol Gels. *Aerosol Sci. Technol.* 52:953–956.

Kearney, S. P., and Pierce, F. (2012) Evidence of Soot Superaggregates in a Turbulent Pool Fire. *Combust. Flame*, 159:3191–3198.

Kroy, K., Cates, M. E., and Poon, W. C. K. (2004) Cluster Mode-Coupling Approach to Weak Gelation in Attractive Colloids. *Phys. Rev. Lett.*, 92:148302.

Lattuada, M., Sandkühler, P., Wu, H., Sefcik, J., and Morbidelli, M. (2003) Aggregation Kinetics of Polymer Colloids in Reaction Limited Regime: Experiments and Simulations. *Adv. Colloid Interface Sci.*, 103:33–56.

Liu, P., Arnold, I. J., Wang, Y., Yu, Y., Fang, J., Biswas, P., and Chakrabarty, R. K. (2015) Synthesis of Titanium Dioxide Aerosol Gels in a Buoyancy-Opposed Flame Reactor, *Aerosol Sci. Technol.*, 49:1232–1241.

Liu, P, Heinson, W. R., Sumlin, B. J., Shen, K., and Chakrabarty, R. K. (2018) Establishing the Kinetics of Ballistic-to-Diffusive Transition using Directional Statistics. *Phys. Rev. E*, 97:042102.

Lushnikov, A. A. (2006) Gelation in Coagulating Systems. *Physica D*, 222:37–53.

Manrique, P.D., Zheng, M., Cao, Z., Restrepo, E. M., and Johnson, N. F. (2018) Generalized Gelation Theory Describes Onset of Online Extremist Support. *Phys. Rev. Lett.*, 121:048301.

Meakin, P. (1984) Computer Simulation of Cluster-Cluster Aggregation using Linear Trajectories: Results from Three-Dimensional Simulations and a Comparison with Aggregates Formed using Brownian Trajectories. *J. Colloid Interface Sci*., 102:505–512.

Oh, C., and Sorensen, C. M. (1997) Light Scattering Study of Fractal Cluster Aggregation Near the Free Molecular Regime. *J. Aerosol Sci.*, 28:937–957.

Powell, M. J. (1979) Site Percolation in Randomly Packed Spheres. *Phys. Rev. B*, 20:4194.

Rottereau, M., Gimel, C. J., Nicolai, T., and Durand, D. (2004) Monte Carlo Simulation of Particle Aggregation and Gelation: I. Growth, Structure and Size Distribution of the Clusters. *Eur. Phys. J. E*, 15:133–140.

Sandkühler, P., Sefcik, J., Lattuada, M., Wu, H., and Morbidelli, M. (2003) Modeling Structure Effects on Aggregation Kinetics in Colloidal Dispersions. *AIChE J*., 49:1542–1555.

Sandkühler, P., Sefcik, J. and Morbidelli, M. (2004) Kinetics of Aggregation and Gel Formation in Concentrated Polystyrene Colloids. *J. Phys. Chem. B*, 108:20105–20121.

Sandkühler, P., Sefcik, J., and Morbidelli, M. (2004) Kinetics of Gel Formation in Dilute Dispersions with Strong Attractive Particle Interactions. *Adv. Colloid Interface Sci.*, 108:133–143.

Sorensen, C. M., Hageman, W. B., Rush, T. J., Huang, H., and Oh, C. (1998) Aerogelation in a Flame Soot Aerosol. *Phys. Rev. Lett.*, 80:1782.

Sorensen C. M. (2011) The Mobility of Fractal Aggregates: A Review. *Aerosol Sci. Technol.*, 45:765–779.

Sorensen, C, M., and Chakrabarti, A. (2011) The Sol to Gel Transition in Irreversible Particulate Systems. *Soft Matter*, 7:2284–2296.

Stauffer, D. (1976) Gelation in Concentrated Critically Branched Polymer Solutions. Percolation Scaling Theory of Intramolecular Bond Cycles. *J. Chem. Soc. Faraday Trans.*, 2:1354.

Stauffer, D., Coniglio, A., and Adam, M., (1982) Gelation and Critical Phenomena. *Adv. Polym. Sci.*, 44:103.

Van Dongen, P. G. J., and Ernst, M. H. (1985) Dynamic Scaling in the Kinetics of Clustering. *Phys. Rev. Lett.*, 54:1396.

Zaccone, A., Wu, H., and Del Gado, E. (2009) Elasticity of Arrested Short-Ranged Attractive Colloids: Homogeneous and Heterogeneous Glasses. *Phys. Rev. Lett.*, 103:208301.

Chapter 5: Fractal Scaling of Soot Packing Density across Five Size Decades

The results of this chapter have been published in Liu, P., Heinson, W. R., Chakrabarty R. K. (2017). Fractal Scaling of Soot Packing Density across Five Size Decades. Aerosol Science and Technology, 51, 879-886.

Abstract

Flame soot particles have been observed to take a broad size range: Their radius of gyration (R_g) extends from few hundreds nanometer to nearly one millimeter depending on the scale of the combustion systems. The morphology, as well as packing density (θ_f, volume fraction of solid matter) of these particles at long range limit of R_g have yet to be comprehensively studied, especially beyond the length scale of aerosol gelation. In this work, we experimentally map the scaling laws for packing density (θ_f, solid component volume fraction) of soot aggregates across five orders of magnitude of size (R_g/a, normalized radius of gyration by monomer radius). The θ_f – R_g/a scaling relationship evolves through three successive regimes with distinct power-law exponents of – 1.20 ± 0.01, – 0.58 ± 0.06, and – 1.31 ± 0.14. The first cross-over agrees with the classical aerosol-to-gel transition theory. This agreement, however, breaks down at the second cross-over point, where a late-stage cluster-cluster aggregation of aerosol gels takes over.

5.1 Introduction

Soot aggregates are produced from incomplete combustion of hydrocarbon fuels in a wide range of natural and anthropogenic systems, for example, vehicular engines, biomass burning, and wildfires (Chao et al. 1998; Park et al. 2004; Kumfer et al. 2006; Law 2010; Rehman et al. 2011; Chakrabarty et al. 2014a). These aggregates constitute of repeating near-spherical monomers and are fractal-like and porous in their morphology and composition, respectively (Forrest and Witten 1979; Sorensen 2001, 2011). The packing density (θ_f) – defined as the fraction of the sub-volume taken by solid matter – is a fundamental property of these aggregates with many important implications. θ_f determines the transport characteristics and radiative forcing of these aggregates in the atmosphere (Bond et al. 2013; Chakrabarty et al. 2014a; Liu and Chakrabarty 2016; Heinson and Chakrabarty 2016). Accurate knowledge of θ_f is necessary to determine the extent of particle deposition in human lungs (Taulbee and Yu 1975; Hinds 1999). When it comes to synthesis of these aggregates for commercial purposes, a control of θ_f renders tailoring of desirable material properties, such as permeability, mechanical strength, thermal, and electrical conductivities (Johnson et al. 1996; Sánchez-González et al. 2005; Dhaubhadel et al. 2007; Greaves et al. 2011; Sakai et al. 2016).

Aggregate θ_f scales with radius of gyration (R_g) following a fractal power-law relationship,

$$\theta_f = k_f\left(R_g/a\right)^{D_f-3} \tag{5.1}$$

where k_f is the fractal prefactor, a is one monomer radius, and D_f is the mass fractal dimension that controls how fast θ_f decreases with increasing R_g (Forrest and Witten 1979; Sorensen 2001, 2011; Zangmeister et al. 2014). The value of D_f provides insight into the aggregate growth mechanism

in a system. Aerosol aggregates with $R_g < 1$ mm have been shown to grow via the diffusion-limited cluster-cluster aggregation (DLCA) mechanism with a characteristic $D_f \approx 1.78$ (Sorensen 2001, 2011). Beyond this size range, DLCA aggregates that are non-coalescent tend to behave as "super-monomers" and jam together to form percolated networks (or aerosol gels) with a $D_f \approx 2.5$ (Sorensen et al. 1998; Sorensen and Chakrabarti 2011). The gelation of aerosol aggregates was first observed by Sorensen et al. (1998) and termed as aerosol gelation (Sorensen and Chakrabarti 2011). The theory of aerosol gelation is however not exhaustive to describe the growth of particles with large R_g. Multiple mechanisms have been suggested to take precedence successively in the growth regime $R_g > 1$ mm (Kim et al. 2006). This implies a varying power-law exponent for θ_f in the large R_g/a limit, different from that predicted by the classical percolation model, ca. -0.5.

There exist very limited studies on the experimental determination of θ_f for fractal aggregates with R_g/a reaching the large limit. Manley et al. (2004) showed aggregate structure tends to catastrophically break down when R_g/a reaches 10^3; thus, the direct measurement of θ_f for the particles that are intact could be hindered by their mechanical instability. More recently, Zangmeister et al. (2014) reported the measurement of θ_f for rigid aggregates subjected to omnidirectional compaction forces. A remarkable scale-invariant $\theta_f \approx 0.36$ of the aggregates was observed for R_g/a across many orders of magnitude (Zangmeister et al. 2014). This confounding scale-independence, implying lack of any growth mechanism beyond percolation, has in part motivated this current study. Our objective herein is to provide a complete picture of the scaling relationship of θ_f across five orders of magnitude of R_g/a for freshly produced soot aggregates and infer their size delimited growth mechanism.

5.2 Methods

5.2.1 Characterization of sub-micron size aggregates

For soot aggregates with R_g < 1 mm, we deduced their θ_f based on previously published mass-mobility experimental data. Cross et al. (2010) had generated nascent soot aggregates using an ethylene flat flame burner and measured the mass (M) of these aggregates with certain mobility diameter (d_m) using a tandem differential mobility analyzer (DMA) – centrifugal particle mass analyzer (CPMA) – condensational particle counter (CPC) setup (Park et al. 2004; Cross et al. 2010; Zangmeister et al. 2014). We estimated N of these aggregates from the aggregate-to-monomer mass ratios. The monomer density ρ and average radius a were taken as 1812 kg/m^3 and 16 nm, respectively (Cross et al. 2010; see Appendix III Section A3.1). We estimated aggregate R_g from their d_m using the well-established empirical relationship for DLCA aggregates with N < 100 (Sorensen 2011):

$$\frac{d_m}{2R_g} = 1.29N^{-0.1} \tag{5.2}$$

Finally, we calculated aggregate θ_f using the expression:

$$\theta_f = \frac{3M}{4\pi R_g^3 \rho} \tag{5.3}$$

5.2.2 Characterization of super-micron size aggregates

Soot aggregates with R_g > 1 mm were generated using a novel buoyancy-opposed flame (BOF) reactor (Chakrabarty et al. 2012, 2014b; Liu et al. 2015) fueled by ethylene. Emitted particles were collected onto conducting carbon films (Ted Pella Inc., Redding, CA, USA) installed in a

multistage size-segregated aerosol impactor (MPS-6, California Measurements Inc., Sierra Madre, CA, USA). Aggregate morphology was characterized using scanning electron microscope (SEM, Nova-230, FEI, Hillsboro, OR, USA) and custom-built image processing software. The number of monomers constituting an aggregate as seen in an image (N_{2d}) was estimated by the ratio of the aggregate's projected area (A_p) to the monomer cross-section area πa^2. N_{2d} was next converted to its three-dimensional (3-d) N based on an empirical relationship established computationally using the off-lattice DLCA model (see Appendix III Section A3.2):

$$N = 0.93 N_{2d}^{1.16} \tag{5.4}$$

We determined the R_g of an aggregate from its pixelated SEM image by calculating the root mean square distance of all pixels (within the aggregate perimeter) from the aggregate geometric center. The θ_f of these particles was calculated with the knowledge of their N, a, and R_g using the equation:

$$\theta_f = N\left(a/R_g\right)^3 \tag{5.5}$$

Please note that we assumed in Equation (5.5) the R_g calculated from two-dimensional (2-d) microscope image to be equal to the true R_g of the aggregates in 3-d. Chakrabarty et al. (2011) showed in their simulation work the ratio of 2-d to 3-d Rg to be about 0.93 for DLCA aggregates in cluster-dilute regime. We show in the Appendix III Section A3.3 that the ratio is about 0.98 for cluster-dense gels.

We calculated the structure factor (S) of the sampled aggregates by performing Fourier transform on their projected images (Sorensen 2001; Heinson et al. 2017). Determination of S facilitated the double-checking for accuracy and consistency of D_f for these particles, per the scaling relationship that holds in the reciprocal-space (Sorensen 2001; Heinson et al. 2017):

$$S \propto \left(qR_g\right)^{-D_f} \tag{5.6}$$

In another set of experiments, we dropped a total of 117 aggregates freshly produced from the ethylene BOF in the size-range 100 mm < R_g < 1.5 mm into stagnant air at 25 °C and 1 atm. The M of these aggregates were estimated from their terminal settling velocity v_{ts} based on the Stokes law (Friedlander 2000),

$$M = g^{-1}6\pi\mu R_g\left[1 + 0.158\left(\frac{2\rho_f v_{ts} R_g}{\mu}\right)^{2/3}\right]v_{ts} \tag{5.7}$$

where g is gravitational acceleration, μ and ρ_f are the air dynamic viscosity and density with the value of 1.8×10^{-5} Pa·s and 1.29 kg/m3, respectively. Note that the measured v_{ts} was divided by a factor $C = 6.15 \pm 2.15$ prior to the calculation of M using Equation (5.7), per the work of Johnson et al. (1996). This precaution was taken to compensate for the systematic over-estimation of M when applying Stokes law on fractal aggregates that are porous and permeable (Johnson et al. 1996). The R_g of these aggregates were determined from their pixelated optical microscope images, according to the similar method discussed in previous paragraph. The θ_f of this set of aggregates was next determined using Equation (5.3).We find it important to mention the assumption made when using Equations (5.3) and (5.5). The bulk volume of a fractal aggregate is approximated to be that of a sphere with radius R_g. The uncertainties that could stem from this assumption are investigated in detail in the Results section.

5.2.3 Numerical simulation

We performed two sets of numerical investigation to complement and theoretically validate our experimental findings. The first set of simulations involved generating 53,483 aggregates using

the off-lattice DLCA algorithm (Meakin 1985; 1999). The detailed description of this algorithm can be found in references (Heinson and Chakrabarty 2016; Heinson et al. 2017; Heinson 2015). The initial monomer volume fraction (f_{vm}), which is an important control parameter for aerosol aggregation, was varied between the extreme values of 0.001 and 0.1. The influence of f_{vm} on the earliness of aerosol gelation was comprehensively discussed in Reference (Sorensen and Chakrabarti 2011). The second set of simulations involved using the percolation model to generate 10^4 aggregates (Stauffer and Aharony 1994; Heinson 2015). θ_f of all numerically generated aggregates were calculated using Equation (5.5). Table 5.1 summarizes the various experimental and numerical techniques employed in this study to generate and characterize particles in different size ranges for determination of their θ_f. The source of the mass-mobility data, based on which we inferred the θ_f for aggregates in the extremely small R_g/a limit, is also listed in Table 5.1

Table 5.1 Source of previously published data involved in our analysis and the experimental methods employed in this work

<table>
<tr><th>Group Index</th><th>Size Range R_g/a</th><th colspan="2">Particle Source</th><th>Characterization Method</th></tr>
<tr><td>A</td><td>1-20</td><td colspan="2">Kerosene flame</td><td>DMA-CPMA-CPC</td></tr>
<tr><td>B</td><td rowspan="2">2-400</td><td rowspan="6">Off-lattice DLCA model</td><td>f_{vm} = 0.001</td><td rowspan="7">N/A</td></tr>
<tr><td>C</td><td>f_{vm} = 0.003</td></tr>
<tr><td>D</td><td rowspan="2">2-300</td><td>f_{vm} = 0.01</td></tr>
<tr><td>E</td><td>f_{vm} = 0.02</td></tr>
<tr><td>F</td><td>2-200</td><td>f_{vm} = 0.1</td></tr>
<tr><td>G</td><td>3-1,000</td><td colspan="2">Percolation model</td></tr>
<tr><td>H</td><td>30-5,000</td><td colspan="2" rowspan="2">Ethylene BOF</td><td>SEM Image processing</td></tr>
<tr><td>I</td><td>3,000-50,000</td><td>Stokes Law Eq. (5.3)</td></tr>
</table>

5.3 Results and Discussion

5.3.1 Spherical approximation of aggregate bulk volume

The uncertainty that stems from applying spherical geometry to approximate the bulk volume for aggregates, that is, $V_{agg(spher\ )} = \frac{4}{3}\pi R_g^3$ is determined in this section. We do so by comparing $V_{agg(sphere)}$ to $V_{agg(ellipsoid)} = \frac{4}{3}\pi R_1 R_2 R_3$, where R_1, R_2, and R_3 are the three principal radii of an aggregate as well as an ellipsoid tightly bounding the aggregate. It has been shown that the use of these three principal radii takes into account the aggregate shape anisotropy (Heinson et al. 2010). In Figure 5.1, we plot the ratio $V_{agg(sphere)}/V_{agg(ellipsoid)}$ as a function of aggregate shape anisotropy $A = R_1/R_3$ for particles generated in experimental sets N1, N5, and N6. These three sets of particles represent cluster-dilute DLCA, cluster-dense DLCA, and gel particles, respectively. One can see from Figure 5.1 that with increasing A, the ratio $V_{agg(sphere)}/V_{agg(ellipsoid)}$ increases monotonically for all particle sets. This trend implies that a spherical approximation leads to overestimation of the bulk volume of highly anisotropic aggregates with large A. However, had we used aggregate perimeter radius instead of its R_g, the ratio $V_{agg(sphere)}/V_{agg(ellipsoid)}$ would always be greater than 1 for all aggregates. In other words, the use of R_g partially compensates for the overestimation stemming from the spherical volume approximation. For cluster-dilute DLCA aggregates, whose A distribution peaks at 2.5 (Heinson et al. 2010), the R_g-based spherical geometry reasonably approximates the aggregate bulk volume. We should also emphasize here that when DLCA aggregates gel, the shape of the resulting gel particles tends to be more isotropic with smaller A. As A decreases, the bulk volume of gels would be underestimated, which would yield an overestimated θ_f. Finally, it is worth mentioning that the fractal scaling of θ_f would remain unaffected regardless of how the bulk volume of a particle is approximated. That is to say, the

scaling exponent of θ_f would always be equal to $D_f - 3$ so long as a Euclidean object is chosen to represent the encompassing space.

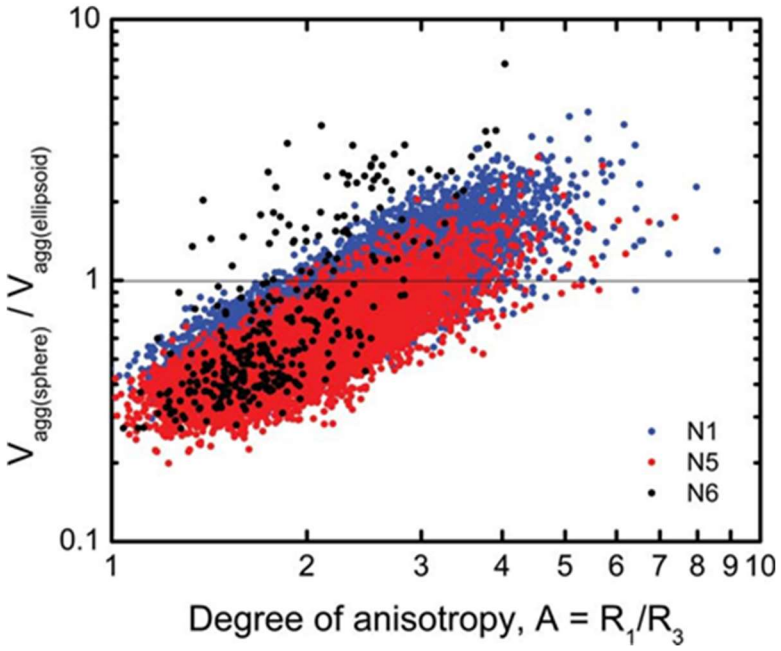

Figure 5.1. Ratio of $V_{agg(sphere)} = 4\pi R_g^3/3$ to $V_{agg(ellipsoid)} = 4\pi R_1 R_2 R_3/3$ as a function of shape anisotropy $A = R_1/R_3$ of the aggregates (or gels) numerically generated using off-lattice DLCA model (sets N1 and N5) and percolation model (set N6).

5.3.2 Fractal scaling of θ_f

Figure 5.2 shows the comparison of the $\theta_f - R_g/a$ scaling relationships between aggregates studied by Cross et al. (2010) and that of sets N1–N6 from this study. Good agreement between Cross et al. (2010) and set N1 aggregates could be seen. Empirical fit to the data of set N1 aggregates following Equation (5.1) reveals an ensemble average $D_f = 1.80 \pm 0.01$, which is in good agreement with the prediction of DLCA growth mechanism in a cluster-dilute Brownian system (for example, $f_{vm} = 0.001$). Comparison between sets N1 and N2 aggregates shows that for initial monomer $f_{vm} = 0.003$, the decreasing trends of θ_f starts to deviate from the prediction of DLCA (black line) at

R_g/a = ca. 10^2. This inflection is an indication of the onset of aerosol gelation. Comparison between aggregates corresponding to sets N1–N5 shows that with an increase of initial monomer f_{vm}, the inflection point shifts toward smaller R_g/a. This implies that gelation of DLCA aggregates takes place more readily in a denser (high f_{vm}) sol system, which is in agreement with the prediction of aerosol-to-gel theory (Sorensen and Chakrabarti 2011). When an aggregating system starts out under extremely dense conditions, which correspond to f_{vm} = 0.1 (set N5 aggregates), the scaling relationship of θ_f asymptotes to what the percolation model predicts (see the red line and set N6 data). Empirical fitting of the data corresponding to set N6 aggregates reveals a D_f = 2.42 ± 0.03, which closely matches the $D_f \approx 2.5$ value observed for gels. Summarizing Figure 5.2, we show the evolution of $\theta_f - R_g/a$ scaling relationships for aerosol aggregates in the small R_g/a limit.

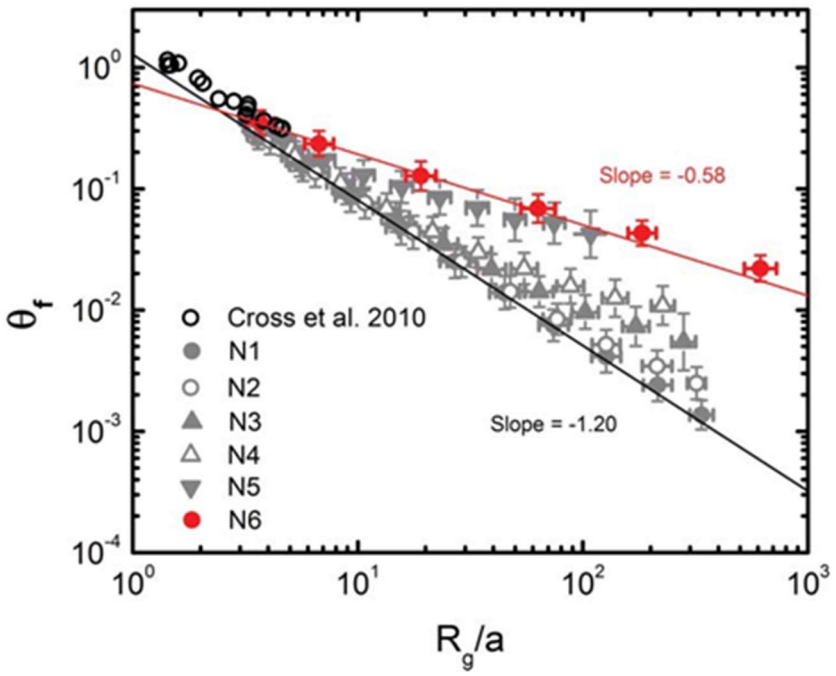

Figure 5.2. The $\theta_f - R_g/a$ scaling relationship of soot aggregates studied by Cross et al. (2010) compared to that of sets N1–N6 from this study. Error bars represent one geometric standard deviation. Least-square fitting of the data of sets N1 and N6 yields $\theta_f = 1.28 \pm 0.03(R_g/a)^{-1.20 \pm 0.01}$ (lower black line) and $\theta_f = 0.74 \pm 0.08(R_g/a)^{-0.58 \pm 0.06}$ (upper red line), respectively.

Figure 5.3 shows the microscope images of the BOF-produced soot particles in the large R_g/a limit (corresponding to sets E1 and E2). We present this series of microscope images at changing degrees of magnification to give the readers a qualitative feel of the morphology of cluster-dense soot produced by our reactor. The constituent monomers, with a mean radius = 30 nm, are near spherical and point-contacting. At larger length scales, the monomers are no longer discernible; however, the fractal nature of the aggregates is still preserved, implying scale-dependence of θ_f.

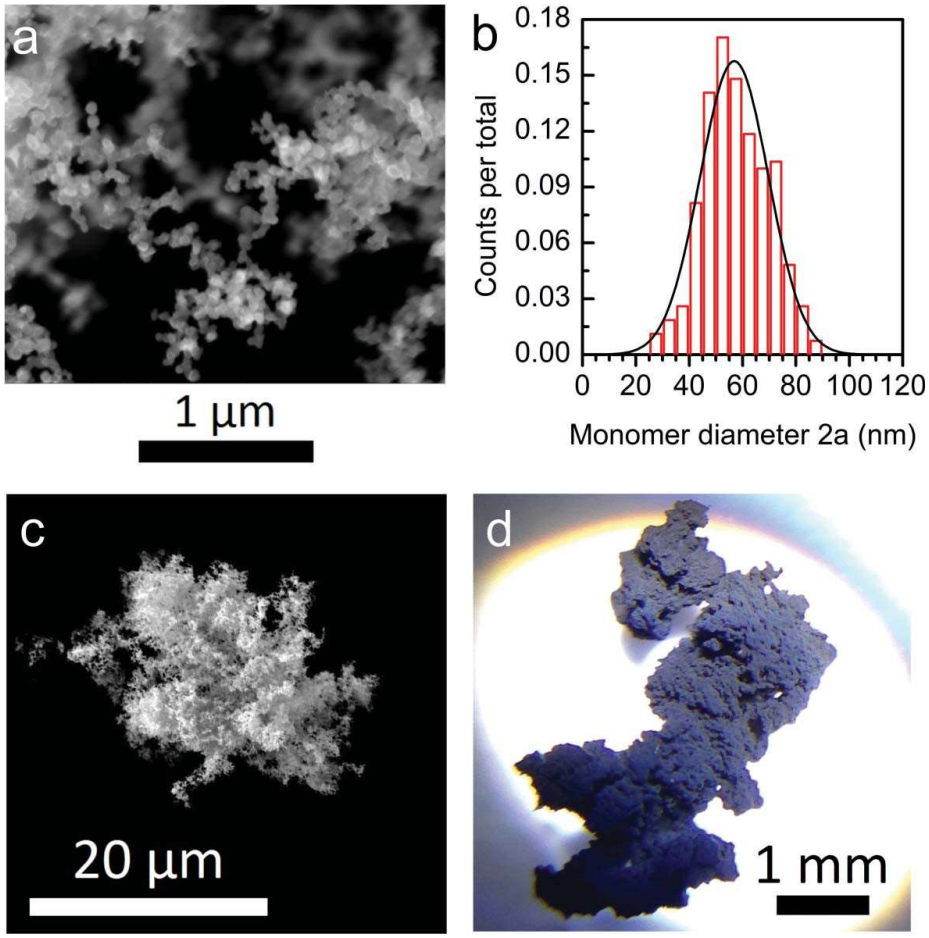

Figure 5.3. Morphologies of BOF produced soot (sets E1 and E2) at three different length scales. (a) SEM image showing the shape of the soot monomers. (b) The probability distribution of the monomer diameter $2a$. Columns (red) represent the normalized counts of monomers within each size bin having a width of 5 nm. The solid line represents a Gaussian fit that peaks at 60.2 nm. (c) SEM image showing the soot morphology at micrometer scale. (d) Optical microscope image showing soot morphology at millimeter scale.

Figure 5.4 shows the comparison of $\theta_f - R_g/a$ scaling relationship for particles corresponding to sets N6, E1, and E2. The E1 dataset, obtained from digital processing of SEM images of BOF-generated soot, deviates slightly from the prediction of the percolation model (red dash line). This slight deviation may arise from the artifacts associated with the particle sampling process. Inertial impaction could cause deformation of an aggregate's silhouette (or outer structure) but not its internal structure and monomer packing arrangements. This is evident from the structure factor $S(qR_g)$ plot in Figure 5.5, which contains details on a particle's internal structure. Beyond the Guinier regime ($qR_g > 1$), S is observed to scale with $qR_g^{-2.5}$ in concurrence with the D_f of gels.

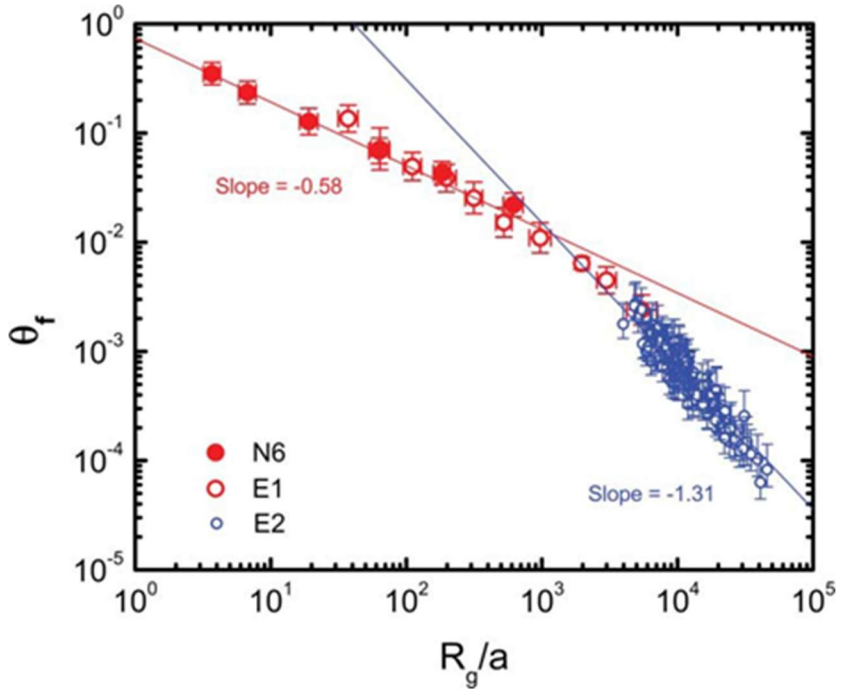

Figure 5.4. The $\theta_f - R_g/a$ scaling relationship of particles corresponding to sets N6, E1, and E2. Error bars represent one geometric standard deviation for N6 and E1 datasets. For the E2 dataset, errors stem from the uncertainty in $C = 6.15 \pm 2.15$ as reported by Johnson et al. (1996). Least-square fitting of the data of set E2 yields $\theta_f = 130.20 \pm 164.12(R_g/a)^{-1.31 \pm 0.14}$ (right-most blue line).

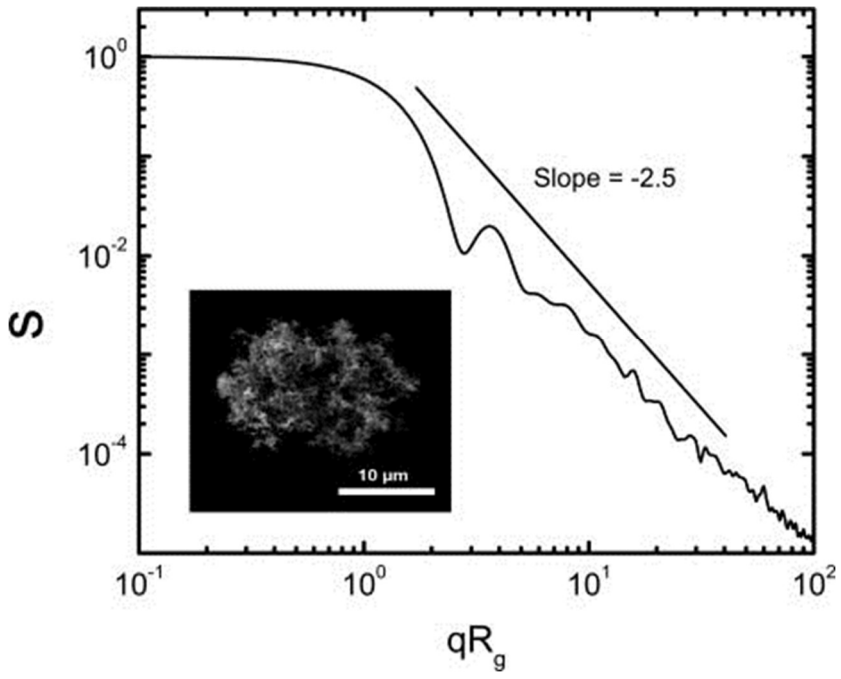

Figure 5.5. SEM image of a typical particle from set E1 and its structure factor in reciprocal space $S(qR_g)$. Black line with a slope = – 2.5 serves as a guide to eyes.

Particles corresponding to sets E1 and E2 have R_g/a in the large limit, that is, $\geq 10^3$. The power-law exponent of θ_f versus R_g/a for these particles gradually decreases to a new value of -1.31 ± 0.14 (blue dash line). Per Equation (5.1), this exponent suggests a distinct $D_f \approx 1.7$, which implies a growth mechanism involving the cluster-cluster aggregation of individual gel particles. Visually, we are encountering a scenario where for $R_g/a > 10^3$ the volume spanning gels start to act like monomers and participate in a late-stage cluster-cluster aggregation process. The dynamics of this late-stage aggregation, which is beyond the typical length-scale of aerosol gelation (Kim et al. 2006), has yet to be systematically studied in flame systems.

We make an attempt to provide a phenomenological understanding of the occurrence of this late-stage aggregation of gel particles, which is observed experimentally but not captured theoretically

in our simulations. Aggregation in open-flow systems, such as flames, deviates from the idealized systems described in the aerosol-to-gel transition theory (Sorensen and Chakrabarti 2011). The spatial distribution of particle f_{vm} could be largely inhomogenous in flames. This gives rise to "dense-spots" in which the f_{vm} of particles is substantially higher than the surroundings, and gels with $D_f \approx 2.5$ are readily formed. For example, Figure 5.6a shows a "dense-spot" in the body of our BOF. The sub-volume wherein the recirculating particle-laden gas flow makes a "U-turn" becomes densely populated with DLCA aggregates (see the location indicated by the red arrow in panel (a)). At this dense-spot, the aerosol-to-gel transition is so prominent that it is visible to naked eyes. Next, the individual gel particles formed in these *dense-spots* are observed to be spatially spreading out (see Figure 5.6b). These diverging gel particles, whose average nearest neighbor separation distance is much larger than their average size, eventually start to behave as monomeric units leading to collision with each other before irreversibly forming the millimeter-size, chain-like, and open-structure aggregates demonstrating a low D_f of ≈1.7 (see the particle indicated by the blue arrow in panel (b)). A qualitative explanation for why the D_f of these particles appears to be smaller than the typical value of 1.8–1.9 expected for a 3-d cluster-cluster aggregation mechanism is briefly provided here. In situ tracking of particle motion in our flame system reveals that the particle trajectories are tightly bound in a 3-d annular region (please refer to the figure in the Appendix III Section A3.4). The thickness of this annular is about 5 mm, which is slightly larger than the mean size of these particles. This confined geometry limits the collisions between a pair of particles to be quasi 3-d in nature, meaning that the probability of particle–particle collision along the radial direction is comparatively lower than along the angular and vertical directions. We infer that this constrained collisional arrangement may have led to a D_f slightly smaller in value than that resulting from unconstrained omni-directional 3-d cluster-cluster

aggregation. On the other hand, this value is still much greater than $D_f \approx 1.4$ resulting from a 2-d cluster-cluster aggregation growth mechanism (Sorensen and Hageman 2001).

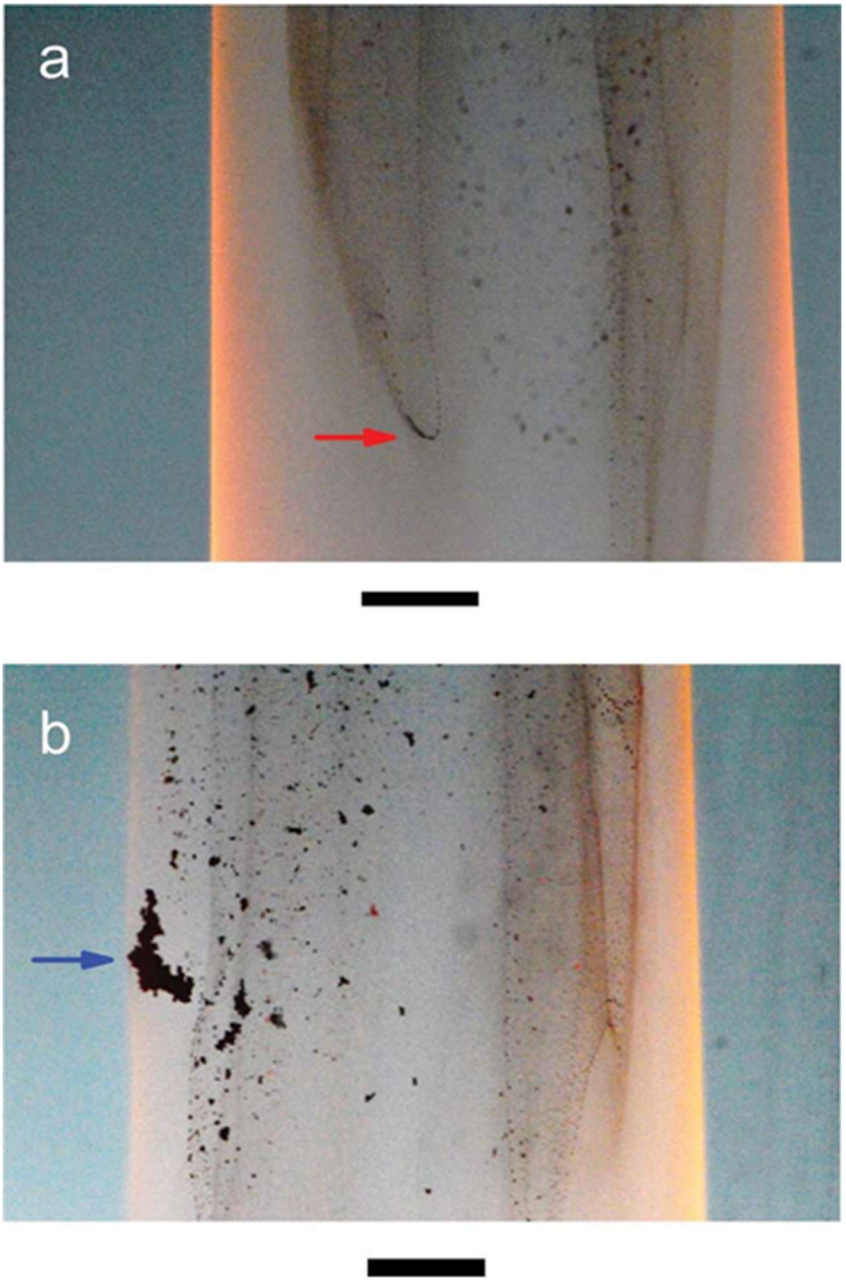

Figure 5.6. Photographs of the ethylene BOF. Scale bars are both 5 mm. Panel (a) shows a "dense-spot" location (indicated by the arrow) where sub-micron DLCA soot aggregates undergoes aerosol gelation. Panel (b) shows the spatial spreading out of gel particles, who then participates in late-stage cluster-cluster aggregation as monomeric units. The resulting macro particle (or aggregated gels) has a low D_f (the one marked by the arrow).

5.4 Conclusion

We now stitch together and summarize the results from above and draw a picture of the scaling variance for θ_f as a function of R_g/a across five orders of magnitude length scale (Figure 5.7). θ_f decreases in distinct power-law exponents of −1.20 ± 0.01, −0.58 ± 0.06, and −1.31 ± 0.14 successively. Fractal nature of soot aggregates is shown to hold even as R_g/a reaches the extremely large limit of 5×10^4. The $\theta_f - R_g/a$ scaling power-law exponents reveal three successive aggregate growth regimes, namely, aggregation of sol clusters (DLCA), gelation of sol clusters, and cluster-cluster aggregation of gels.

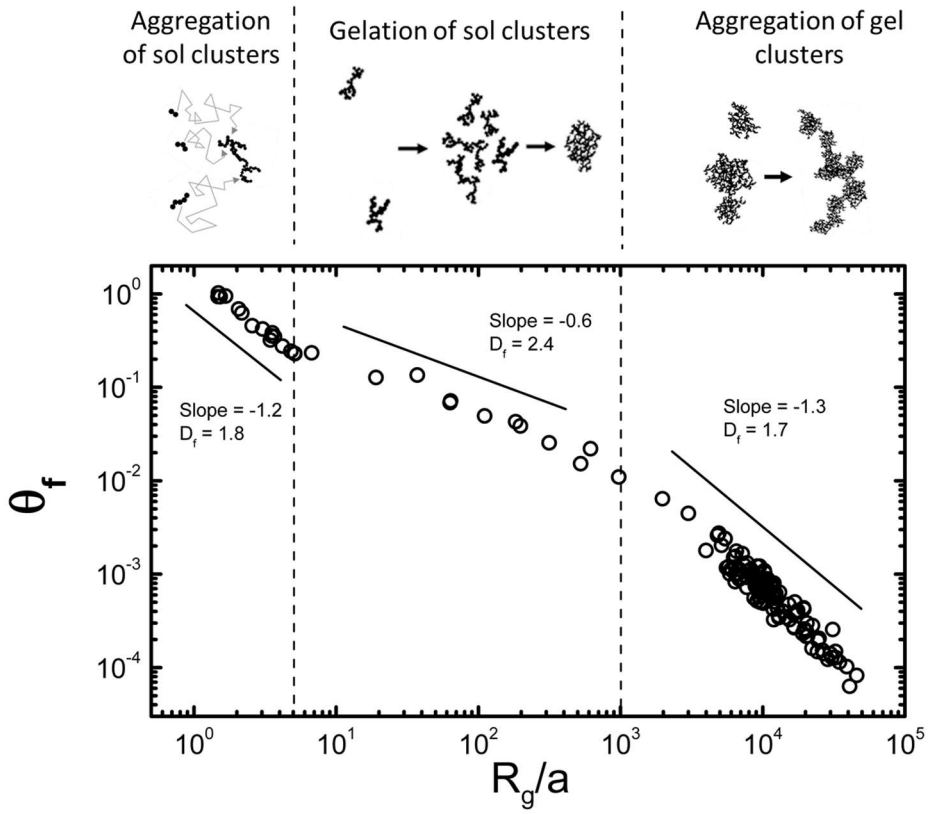

Figure 5.7. Generalized picture of the scale dependence of θ_f for soot aggregates. With R_g/a increasing from 1 to 5×10^4, three successive growth regimes were identified, namely, aggregation of sol clusters (DLCA), gelation of sol clusters, and cluster-cluster aggregation of gels. These growth mechanisms are sketched on top of the figure with their corresponding cross-over points at $R_g/a = 5$ and 10^3. Note that these cross-over R_g/a could be highly system dependent. Blacklines with slopes = – 1.2, – 0.4, and – 1.3 serve as guide to eyes.

The late-stage recurrence of cluster-cluster aggregation in the large R_g/a limit, ca. $\geq 10^3$, could be system dependent and needs to be verified for other sol systems (Sorensen and Feke 1996 Sorensen; Sorensen and Hageman 2001; Kim et al. 2006). Our observation of this fractal scale dependence of θ_f in the large R_g/a limit has important implications for the synthesis of materials with tunable porosity, extremely low density and refractive index, and high surface area per unit volume (Johnson et al. 1996; Sánchez-González et al.; Dhaubhadel et al. 2007; Greaves et al. 2011; Chakrabarty et al. 2014b; Liu et al. 2015; Sakai et al. 2016) and accurate estimation of radiative forcing by carbonaceous aerosols (Bond et al. 2013; Chakrabarty et al. 2014a; Heinson and Chakrabarty 2016).

5.5 References

Bond, T. C., Doherty, S. J., Fahey, D. W., Forster, P. M., Berntsen, T., et al. (2013). Bounding the Role of Black Carbon in the Climate System: A Scientific Assessment. *J. Geophys. Res.*, 118:5380–5552.

Chakrabarty, R. K., Beres, N. D., Moosmüller, H., China, S., Mazzoleni, C., Dubey, M. K., Liu, L., and Mishchenko, M. I. (2014a). Soot Superaggregates from Flaming Wildfires and Their Direct Radiative Forcing. *Sci. Rep.*, 4:5508.

Chakrabarty, R. K., Garro, M. A., Garro, B. A., Chancellor, S., Moosmüller, H., and Herald, C. M. (2011). Simulation of Aggregates with Point-Contacting Monomers in the Cluster–Dilute Regime. Part 2: Comparison of Two-and Three-Dimensional Structural Properties as a Function of Fractal Dimension. *Aerosol Sci. Technol.*, 45:903–908.

Chakrabarty, R. K., Moosmüller, H., Garro, M. A., and Stipe, C. B. (2012). Observation of Superaggregates from a Reversed Gravity Low-Sooting Flame. *Aerosol Sci. Technol.*, 46:i–iii.

Chakrabarty, R. K., Novosselov, I. V., Beres, N. D., Moosmüller, H., Sorensen, C. M., and Stipe, C. B. (2014b). Trapping and Aerogelation of Nanoparticles in Negative Gravity Hydrocarbon Flames. *Appl. Phys. Lett.*, 104:243103.

Chao, B. H., Liu, S., and Axelbaum, R. L. (1998). On Soot Inception in Nonpremixed Flames and the Effects of Flame Structure. *Combust. Sci. Technol.*, 138:105–135.

Cross, E. S., Onasch, T. B., Ahern, A., Wrobel, W., Slowik, J. G., et al., (2010). Soot Particle Studies—Instrument Inter-Comparison—Project Overview. *Aerosol Sci. Technol.*, 44:592–611.

Dhaubhadel, R., Gerving, C. S., Chakrabarti, A., and Sorensen, C. M. (2007). Aerosol Gelation: Synthesis of a Novel, Lightweight, High Specific Surface Area Material. *Aerosol Sci. Technol.*, 41:804–810.

Forrest, S. R., and Witten Jr, T. A. (1979). Long-Range Correlations in Smoke-Particle Aggregates. *J. Phys. A*, 12:L109–L117.

Friedlander, S. K. (2000). Smoke, Dust and Haze: Fundamental of Aerosol Dynamics. Oxford University Press, New York, pp. 109.

Greaves, G. N., Greer, A. L., Lakes, R. S., and Rouxel, T. (2011). Poisson's Ratio and Modern Materials. *Nat. Mater.*, 10:823–837.

Heinson, W. R. (2015). Simulation Studies on Shape and Growth Kinetics for Fractal Aggregates in Aerosol and Colloidal Systems. Ph.D. Thesis, Kansas State University.

Heinson, W. R., and Chakrabarty, R. K. (2016). Fractal Morphology of Black Carbon Aerosol Enhances Absorption in the Thermal Infrared Wavelengths. *Opt. Lett*., 41:808–811.

Heinson, W. R., Liu, P., and Chakrabarty, R. K. (2017). Fractal Scaling of Coated Soot Aggregates. *Aerosol Sci. Technol.*, 51:12–19.

Heinson, W. R., Sorensen, C. M., and Chakrabarti, A. (2010). Does Shape Anisotropy Control the Fractal Dimension in Diffusion-Limited Cluster-Cluster Aggregation? *Aerosol Sci. Technol.*, 44:i–iv.

Hinds, W. C. (1999). Aerosol Technology: Properties, Behavior, and Measurement of Airborne Particles. Wiley, New York, pp. 233–249.

Johnson, C. P., Li, X., and Logan, B. E. (1996). Settling Velocities of Fractal Aggregates. *Environ. Sci. Technol*., 30:1911–1918.

Kim, W., Sorensen, C. M., Fry, D., and Chakrabarti, A. (2006). Soot Aggregates, Superaggregates and Gel-Like Networks in Laminar Diffusion Flames. *J. Aerosol Sci.*, 37:386–401.

Kumfer, B. M., Skeen, S. A., Chen, R., and Axelbaum, R. L. (2006). Measurement and Analysis of Soot Inception Limits of Oxygen-Enriched Coflow Flames. *Combust. Flame*, 147:233–242.

Law, C. K. (2010). Combustion Physics. Cambridge University Press, New York, pp. 119–121.

Liu, P., Arnold, I. J., Wang, Y., Yu, Y., Fang, J., Biswas, P., and Chakrabarty, R. K. (2015). Synthesis of Titanium Dioxide Aerosol Gels in a Buoyancy-Opposed Flame Reactor. *Aerosol Sci. Technol*., 49:1232–1241.

Liu, P., and Chakrabarty, R. K. (2016). Sensitivity Analysis of Aggregate Morphology on Mass-Mobility Relationship and Improved Parameterizations. *Aerosol Sci. Technol*., 50:63–70.

Manley, S., Cipelletti, L., Trappe, V., Bailey, A. E., Christianson, R. J., et al. (2004). Limits to Gelation in Colloidal Aggregation. *Phys. Rev. Lett*., 93:108302.

Meakin, P. (1985). Off Lattice Simulations of Cluster-Cluster Aggregation in Dimensions 2–6. *Phys. Lett. A*, 107:269–272.

Meakin, P. (1999). A Historical Introduction to Computer Models for Fractal Aggregates. *J. Sol-Gel Sci. Technol.*, 15:97–117.

Park, K., Kittelson, D. B., and McMurry, P. H. (2004). Structural Properties of Diesel Exhaust Particles Measured by Transmission Electron Microscopy (TEM): Relationships to Particle Mass and Mobility. *Aerosol Sci. Technol*., 38:881–889.

Rehman, I. H., Ahmed, T., Praveen, P. S., Kar, A., and Ramanathan, V. (2011). Black Carbon Emissions from Biomass and Fossil Fuels in Rural India. *Atmos. Chem. Phys.*, 11:7289–7299.

Sakai, K., Kobayashi, Y., Saito, T., and Isogai, A. (2016). Partitioned Airs at Microscale and Nanoscale: Thermal Diffusivity in Ultrahigh Porosity Solids of Nanocellulose. *Sci. Rep*., 6:20434.

Sánchez-González, J., Macías-García, A., Alexandre-Franco, M. F., and Gómez-Serrano, V. (2005). Electrical Conductivity of Carbon Backs under Compression. *Carbon*, 43:741–747.

Sorensen, C. M. (2001). Light Scattering by Fractal Aggregates: A Review. *Aerosol Sci. Technol.*, 35:648–687.

Sorensen, C. M. (2011). The Mobility of Fractal Aggregates: A Review. *Aerosol Sci. Technol.*, 45:765–779.

Sorensen, C. M., and Chakrabarti, A. (2011). The Sol to Gel Transition in Irreversible Particulate Systems. *Soft Matter*, 7:2284–2296.

Sorensen, C. M., and Feke, G. D. (1996). The Morphology of Macroscopic Soot. *Aerosol Sci. Technol*., 25:328–337.

Sorensen, C. M., and Hageman, W. B. (2001). Two-Dimensional Soot. *Langmuir*, 17:5431–5434.

Sorensen, C. M., Hageman, W. B., Rush, T. J., Huang, H., and Oh, C. (1998). Aerogelation in a Flame Soot Aerosol. *Phys. Rev. Lett.*, 80:1782–1785.

Stauffer, D., and Aharony, A. (1994). Introduction to Percolation Theory. Taylor and Francis, London, pp. 153–168.

Taulbee, D. B., and Yu, C. P. (1975). A Theory of Aerosol Deposition in the Human Respiratory *Tract. J. Appl. Physiol.*, 38:77–85.

Zangmeister, C. D., Radney, J. G., Dockery, L. T., Young, J. T., Ma, X., You, R., and Zachariah, M. R. (2014). Packing Density of Rigid Aggregates is Independent of Scale. *Proc. Natl. Acad. Sci. U.S.A.*, 111:9037–904.

Chapter 6: Synthesis of Titanium Dioxide Aerosol Gels in a Buoyancy-Opposed Flame Reactor

The results of this chapter have been published in Liu, P., Arnold, I. J., Wang, Y., Yu, Y., Fang, J., Biswas, P., Chakrabarty, R. K. (2015). Synthesis of Titanium Dioxide Aerosol Gels in a Buoyancy-Opposed Flame Reactor. Aerosol Science and Technology, 49, 1232-1241.

Abstract

Aerosol gels are a novel class of materials with potential to serve in various energy and environmental applications. In this work, we demonstrate the synthesis of titanium dioxide (TiO_2) aerosol gels using a methane-oxygen co-flow diffusion flame reactor operated in down-fired configuration (fuel flow in the direction opposite to buoyancy forces). Titanium tetraisopropoxide was fed as a precursor to the flame under different operating conditions. Control of the monomer size and crystalline phase of TiO_2 gel particles was achieved by adjusting the flame operating conditions, specifically the flame temperature, which was shown to significantly influence the phase transformation and rate of particle growth and sintering. The resulting materials were characterized for their physical and optical properties. Results showed that the TiO_2 aerosol gels had effective densities in the range 0.021–0.025 g/cm^3, which is 2 orders of magnitude less than the theoretical mass density of TiO_2. The monomer size distribution and crystalline phase, and UV-Vis absorbance spectra of the gels showed distinct characteristics as a function of flame temperature.

6.1 Introduction

Aerosol gels exhibit unique material properties such as ultralow density and high surface area that give rise to their potential in various environmental applications such as catalysis, water and air purification, and photovoltaic (Dhaubhadel et al. 2007; Dhaubhadel et al. 2012). Synthesis of aerosol gel in gas phase has been recently demonstrated as a viable and economical alternative to the conventional wet sol-gel process, which is both time-consuming and expensive (Dhaubhadel et al. 2007; Brinker and Scherer 2013; Chakrabarty et al. 2014). The fundamentals of aerosol gelation theory have been thoroughly investigated in the last two decades, primarily by Sorensen's group at the Kansas State University (Sorensen et al. 1998; Dhaubhadel et al. 2007; Sorensen and Chakrabarti 2011). On the experimental front, novel techniques have been demonstrated for lab-scale synthesis of various aerosol gel materials (Dhaubhadel et al. 2007; Chakrabarty et al. 2014). However, much work still remains to establish gas phase as a scalable synthesis route for production of aerosol gels with controlled properties. In particular, control of monomer size in aerosol gels is needed because of its importance in governing the specific surface area (SSA), mobility, and optical properties of these materials.

In this study, we demonstrate the gas-phase synthesis of titanium dioxide (hereafter, TiO_2) aerosol gels with controlled monomer size and crystalline phase using a diffusion flame aerosol reactor operated in a buoyancy-opposed configuration (Chakrabarty et al. 2012; 2014). Flame aerosol reactors have been widely adopted by industries for cost-effective, continuous and one-step synthesis of a wide variety of nanomaterials. TiO_2, a material with versatility in practical applications ranging from white pigment to photocatalyst, has not yet been synthesized in a gel form via gas phase processes. At the same time, its well-investigated material properties as a

function of process parameters make it an ideal reference material to demonstrate the extent of control in our synthesis process (Jiang et al. 2007). A brief review of gas-phase gelation theory and the necessary criteria for designing a flame reactor are discussed in the next paragraph. This is followed by a section on experimental setup and analytical procedures. Next, results and findings of this study are discussed. The chapter concludes with summarizing our major findings and pointing to future research directions.

6.2 Criteria for Designing Gas-Phase Gelation Reactor

In gas phase, aerosol gelation starts out with individual nanoparticle monomers colliding in the "cluster-dilute" regime via the diffusion-limited cluster agglomeration (DLCA) mechanism to form submicron-sized aggregates with a fractal dimension D_f = ca. 1.8 (Sorensen and Chakrabarti 2011). Such a non-coalescing behavior of the aggregating monomers is an important prerequisite for gelation to take place in gas phase (Dhaubhadel et al. 2007). With time, if the scaling dimensionality of the growing DLCA collisional system remains smaller than three, the condition for "cluster dense" agglomeration sets in. The available free volume inside the system then begins to get progressively occupied by DLCA aggregates to the point where the cluster volume fraction f_{vc}, defined as the ratio of total perimeter volume of DLCA aggregates to the system volume, starts to approach unity (Sorensen and Chakrabarti 2011). When f_{vc} reaches unity, DLCA aggregates start to form network-spanning superaggregates and eventually, gels with a characteristic D_f = ca. 2.5. Such threshold condition (f_{vc} = 1) is called ideal gel point (IGP), and the amount of time required for DLCA systems to reach IGP can be quantified as:

$$t_{IGP} = \frac{4}{3}\pi K^{-1} a^3 f_{vm}^{-2.5} \tag{6.1}$$

where K is the aggregation kernel, a is the radius of constituent monomers, and f_{vm} is the volume fraction of monomers in the system (Dhaubhadel et al. 2007). In order to reach the conditions for gelation, the particle residence time t_{res} should be greater than the threshold gelation time in the system, that is $t_{res} > t_{IGP}$.

The possible roadblock involved in controlling monomer size in gas-phase systems hence arises from the third order dependency of t_{IGP} on the monomer radius, as revealed by Equation (6.1). A small increase in the monomer size would substantially increase t_{gel}, which would need to be facilitated by the gas-phase reactors. Typical particle t_{res} in these reactors is in the order of a few hundred milliseconds (Chakrabarty et al. 2014) and increasing it to reach gelling conditions would require doing major structural modifications to the reactor design (e.g., increasing the reactor length). One way to overcome this difficulty is by operating a flame aerosol reactor in downfired buoyancy-opposed configuration. A past study has demonstrated the unique capability of a down-fired diffusion flame system to synthesize gel materials by enhancing particle t_{res} by as much as 6 orders of magnitude compared to that of the conventional up-fired configuration (Chakrabarty et al. 2014). The different operating conditions of this reactor and their influence on gel properties are described in detail in the subsequent sections.

6.3 Methods

6.3.1 Schematic diagram of reactor setup

Figure 6.1 shows the schematic diagram of the flame reactor setup used in this study. A Burke-Schumann type co-flow diffusion flame burner was operated in down-fired configuration. The burner consists of two concentric stainless-steel tubes with 16- and 70-mm inner diameters, respectively. A honeycomb flow straightener was attached to the outer concentric tube to straighten the co-flow stream. A quartz tube with 70 mm inner diameter and 402 mm length, used for housing the flame, was attached to the burner. Methane (CH_4) served as the combustible hydrocarbon fuel in this work, and was delivered through the inner concentric tube (burner head) at a constant volumetric flow rate of 1.0 lpm. Oxygen (O_2) served as the oxidizer and was delivered through the outer concentric tube at a volumetric flow rate of 10.0 lpm. Nitrogen (N_2) dilution, with flow rate varying from 0 to 30 lpm, was applied to the O_2 stream prior to entering the burner for the purpose of adjusting the flame temperature. Titanium tetraisopropoxide (TTIP), the precursor for TiO_2, was fed into the system from a bubbler via N_2 carrier gas. The flow rate of N_2 carrier stream was maintained at 1.0 lpm. The temperature of the water bath housing the TTIP was set at 80 °C to maintain the precursor feed rate at a steady 0.334 mmol/min, as per the calculations proposed by Siefering and Griffin (1990). A heating tape maintained at 250 °C was wrapped around the TTIP delivery line to prevent the condensation of TTIP vapor onto the line surface. A bypass line without the TTIP feed was also installed to facilitate study of the TTIP-free hydrocarbon flame system. The flow rate of CH_4, O_2, and N_2-TTIP were controlled with mass flow controllers (Airgas Inc., PA, USA) The N_2 dilution flow was controlled using the combination of a needle valve and rotameter. The flow rates of all species mentioned above were controlled and measured at standard temperature and pressure conditions (25 °C and 1 atm).

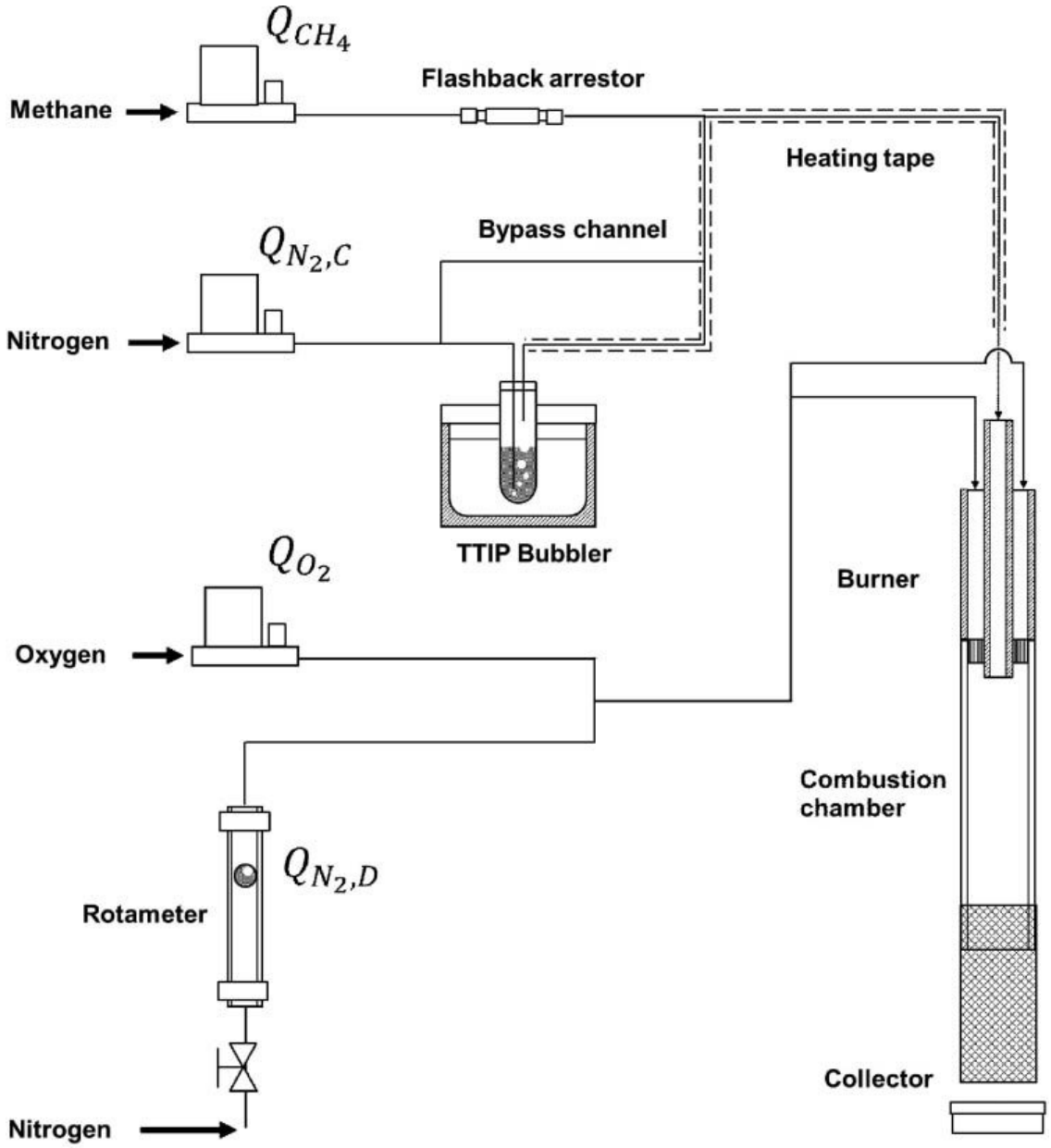

Figure 6.1. Schematic diagram of the buoyancy-opposed flame aerosol reactor. *Q* denotes volumetric flow rate of each species. Subscripts *C* and *D* respectively stand for the "carrier" and the "dilutor" nitrogen.

6.3.2 Characterization of the buoyancy-opposed flame

Prior to synthesizing TiO_2 aerosol gel, specific emphasis was placed to understand the influence of N_2 dilution on flame temperature condition. The precursor bubbler was bypassed in this part of the experiment. Seven operating conditions, outlined in Table 6.1, were identified with volumetric flow rates of N_2 ranging between 0 and 30.0 lpm in 5 lpm increments.

Table 6.1 The different flame operating conditions of this study achieved by varying the amount of N_2 dilution in the co-flow stream. *Q* stands for the volumetric flow rate of each species. Units are all in lpm.

Conditions	Q_{CH4}	Q_{O2}	$Q_{N2,D\ (Dilutor)}$	$Q_{co\text{-}flow}$	$Q_{N2,C\ (TTIP\ carrier)}$
I	1	10	0	10	1
II			5	15	
III			10	20	
IV			15	25	
V			20	30	
VI			25	35	
VII			30	40	

Flame temperatures were measured using a K-type thermocouple with bead diameter = 0.80 mm. The measurements were carried out at two specific locations: (i) the flame center, and (ii) the flame annular region. In the case of (i), the thermocouple bead was placed at the position along the axis of the cylindrical flame body at a distance of half the flame length from the burner head. In the case of (ii), the thermocouple bead was placed at the radially outermost position near the flame bottom. The measurement of temperature in the flame annular region holds valid under the assumption that the axial component of temperature gradient is negligible compared to its radial

counterpart. Photographs of the flame body corresponding to these operating conditions were taken in a dark room.

6.3.3 Synthesis and characterization of TiO_2 aerosol gels

We performed the TiO_2 aerosol gel synthesis at the two extreme operating conditions, I and VII (Table 6.1). Effective density of the gel sample before and after mechanical crushing with mortar and pestle was evaluated by measuring the weight of sample loaded in a container of known volume, according to the method outlined in Ref. (Dhaubhadel et al. 2007). Elemental composition of the samples in the product material were identified using energy dispersive X-ray spectroscopy (EDX, SEM FEI Nova 230). Purity of the material was evaluation based on weight percent values of elemental Ti and O.

The morphology of TiO_2 aerosol gel was investigated with scanning electronic microscope (SEM FEI Nova 230). SSA and equivalent monomer diameter ($D_{p,BET}$) of TiO_2 aerosol gels were determined using the Brunauer–Emmett–Teller (BET) methodology with N_2 as an adsorbate. The crystalline phase of TiO_2 was examined with a Bruker d8 X-ray diffractometer with diffraction angle ranging from 2.5° to 30°.

TiO_2 aerosol gel absorbance spectrum in the ultraviolet (UV) and visible range was determined using a Perkin Elmer UV-Vis spectrometer. Absolute ethyl alcohol was used to disperse the samples. Sample suspension was loaded in a quartz micro cuvette with a 10 mm transmitted path line. Transmittance was measured using an integrating sphere. Absorbance was subsequently evaluated from the transmittance measurements (Perkampus et al. 1992).

6.4 Results and Discussion

6.4.1 Influence of nitrogen dilution on flame temperature

As in conventional diffusion flames, control of temperature in a down-fired buoyancy-opposed diffusion flame could be achieved by addition of inert gases to the co-flow gas stream. In this study, a decrease in temperature from 1250 °C to 590 °C at the flame annular region was observed upon incremental addition (0–30 lpm) of N_2 dilution to the co-flow gas stream (Figure 6.2). With the increase in flow rate of N_2 dilution, the total specific heat of the system is increased, hence resulting in a decrease in adiabatic flame temperature. The increased amount of N_2 in the system also absorbs sensible heat from combustion, further lowering the temperature of the system. The temperature of the flame center was always lower compared to the annular regions. The temperature of the flame's annular region is an important control parameter for particle synthesis. Although gelation of aggregates take place throughout the flame body, the gel particles have been observed to reside the maximum duration in the flame's annular region. It is likely that we could have underestimated the flame temperatures by not accurately accounting for the radiative heat losses associated with the surface of thermocouple beads (Shannon and Butler 2003). Nonetheless, we anticipate this error to be negligible due to the small bead size (0.80 mm in diameter) of our thermocouple used in this study (Hindasageri et al. 2013). Figure 6.3 shows the increase in flame lengths and subsequent change in flame color with N2 dilution ranging between 0 and 30 lpm in 5 lpm increment (from condition I to VII outlined in Table 6.1). The decrease in flame temperature could be qualitatively seen as the bluing of the flame body from the snapshot images in the figure. A lower temperature decreased the rate of CH_4 decomposition and suppressed soot formation, resulting in the blue color of the soot-free flame. It is to be noted that changing of the flame color from yellow to blue does not happen instantaneously with switching of the flame operating

conditions. As shown via the sequence of photographs in Figure 6.4, there was a latency period of approximately 3 min between the color changes, which could be attributed to the residual soot particles trapped in the flame vortices continuing to give off yellow incandescence. This latency period could be qualitatively translated as the maximum residence time of the gel particles before they gravitationally settle out.

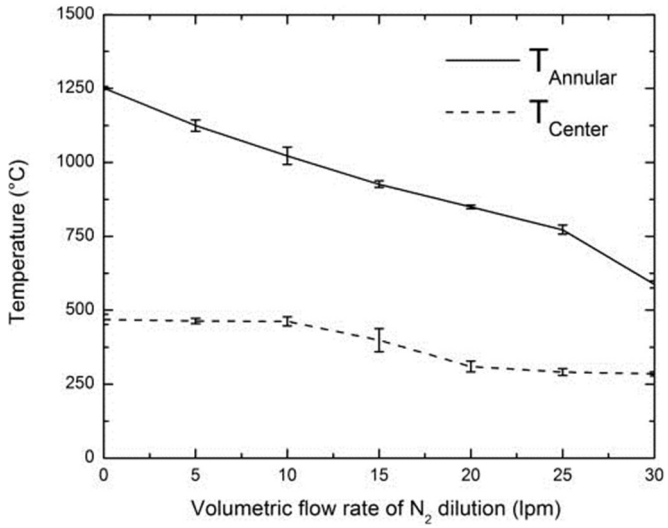

Figure 6.2. Temperature measurement at the flame center (dashed line) and annular region (solid line) under different operating conditions with N_2 dilution (0 to 30 lpm) applied to the co-flow stream.

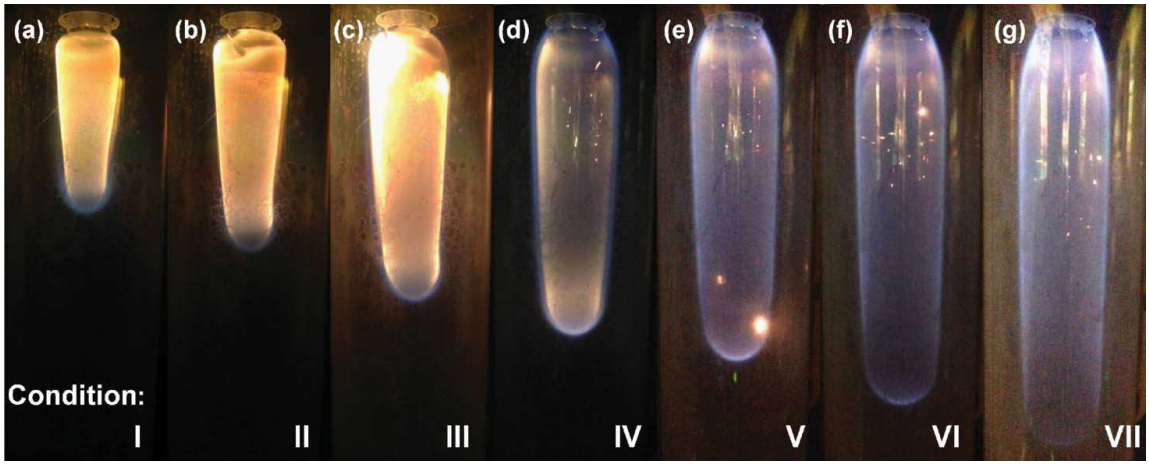

Figure 6.3. (a–g): Photographs of flame operated at conditions I–VII of Table 6.1. Volumetric flow rate of CH_4 and O_2 were kept at 1 and 10 lpm, respectively. N_2 dilution in co-flow stream varied from 0 to 30 lpm in 5 lpm increments.

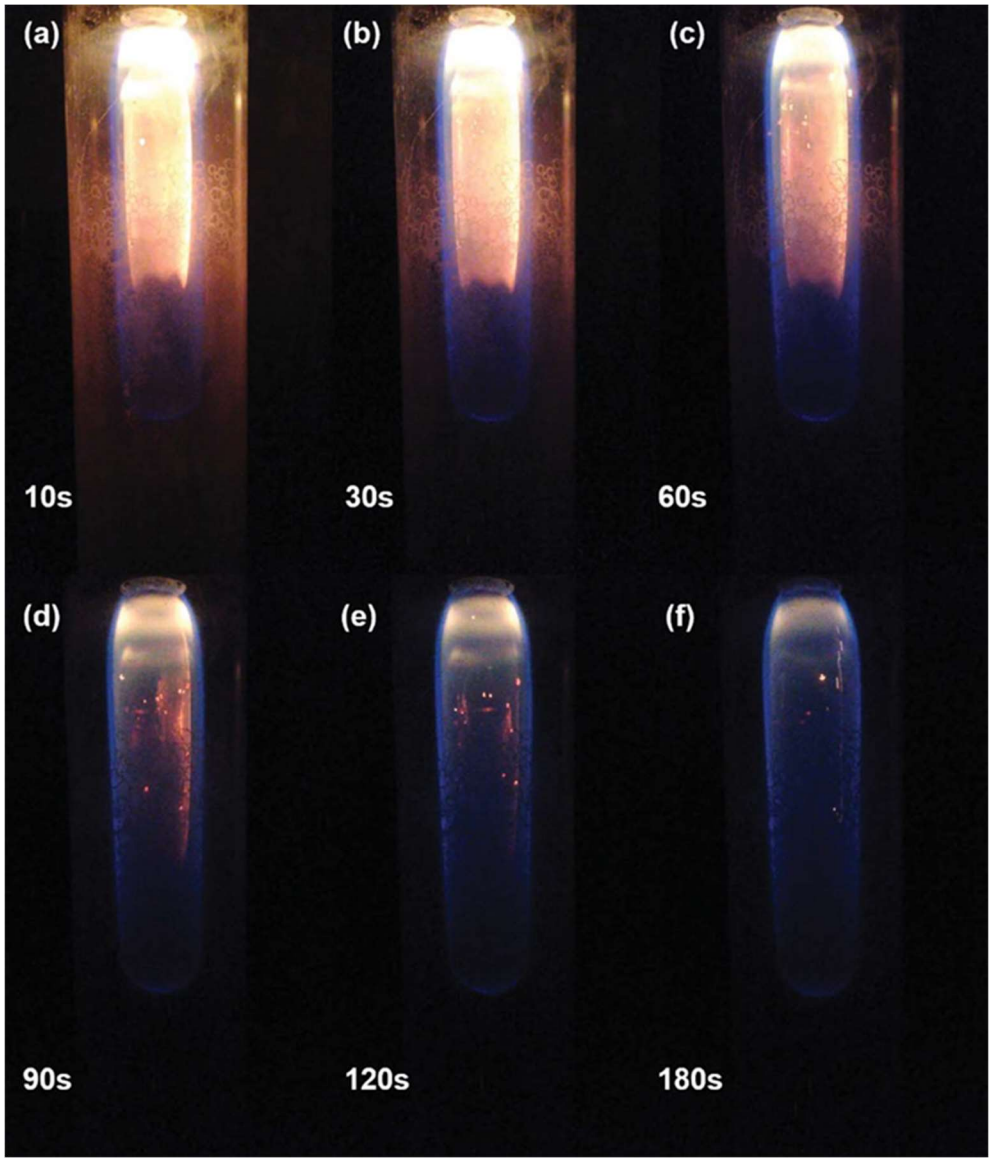

Figure 6.4. (a–f) Photographs of flame body taken at 10, 30, 60, 90, 120, and 180 s after flame condition was switched from condition I to V of Table 6.1.

6.4.2 Influence of flame temperature on TiO_2 aerosol gel properties

Continuous aerosol gelation of TiO_2 nanoparticles was visually observable in the flame body upon addition of TTIP precursor to the system. Physical size of the individual gel particles reached submillimeter in size before gravitationally settling out. Henceforth, in this article, the TiO_2 gel

particles produced in high temperature condition I and low temperature condition VII (Table 6.1) are denoted as TiO2 aerosol gel type 1 (TG1) and type 2 (TG2), respectively. As shown in Figure 6.5, Ti and O atoms were the primary compositional elements detected in the EDX spectra of the gel particles. In the case of TG1, presence of silicon was observed due to the interference of the silicon wafer substrate on which the gel particles were sampled. The weight percent of carbon elements in TG1 and TG2 were 1.83 and 1.73, respectively, suggesting that the gel particles were generally free from carbon contamination. For synthesizing TG1, the flame was operated with pure O_2 in the co-flow stream, which facilitated rapid and complete oxidation of any solid carbonaceous products. In the case of TG2, the flame was operated below sooting limit, thereby inhibiting formation of any solid carbon products.

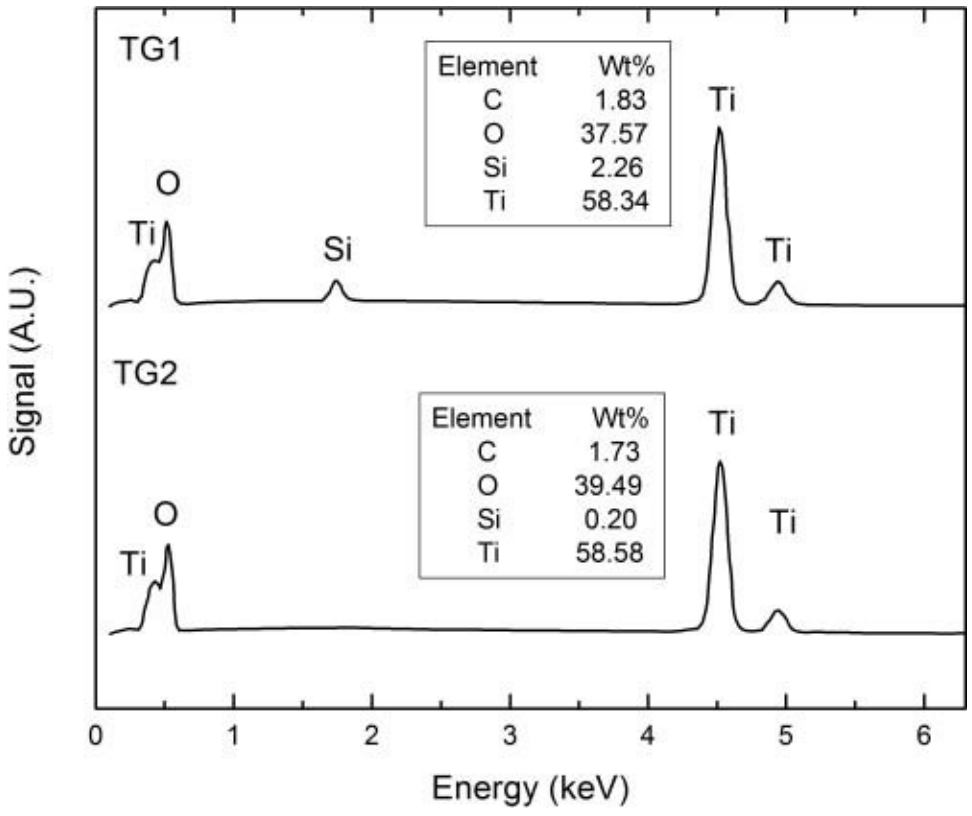

Figure 6.5. EDX spectra with element weight percentage of TiO_2 aerosol gels synthesized at 1250 °C (TG1) and 590 °C (TG2).

The effective densities of uncrushed TG1 and TG2 particles were measured to be 0.025 and 0.021 g/cm^3, respectively. In comparison to TG2, the TG1 sample demonstrated greater rigidity and mechanical strength by resisting structural fragmentation upon mechanical crushing with bare hands. The effective densities of the crushed samples were 0.829 and 0.838 g/cm^3, respectively. The large differences between the effective densities and the theoretical TiO_2 material density (4.23 g/cm^3) is an evidence of the "fluffiness" or large fraction of air voids inside the aerosol gel materials (Dhaubhadel et al. 2007). Note that the effective densities of the TiO_2 gel particles in this study are approximately four to five times greater than that of the carbon gel particles synthesized in a recent study using the same reactor (Chakrabarty et al. 2014). Leaving aside the fact that the mass density of TiO_2 is greater than that of carbon, the high degree of sintering between the TiO_2 monomers could have contributed to their higher effective density. Sintering and necking of monomers significantly reduced the volume fraction of voids in the gel materials.

Figure 6.6 (a, c, and e for TG1; b, d, and f for TG2) shows the TiO_2 gel morphologies at different magnifications. Optical photographs (panel (a) and (b)) show that bulk aerosol gels were white in color and submillimeter in average size. From the SEM images (panel (c)–(f)), the highly porous nature of the material is seen. In panel (c) and (d), the typical volume spanning and network-like structure of aerosol gels can be observed (Brinker and Scherer 2013). Upon zooming in, the crystalline nature of TiO_2 monomers and their degrees of sintering are observed. Interparticle necking interfered with the accurate determination of monomer size distribution from SEM images. Due to this, the average monomer sizes of different samples were also estimated using the BET technique (Akbari et al. 2011).

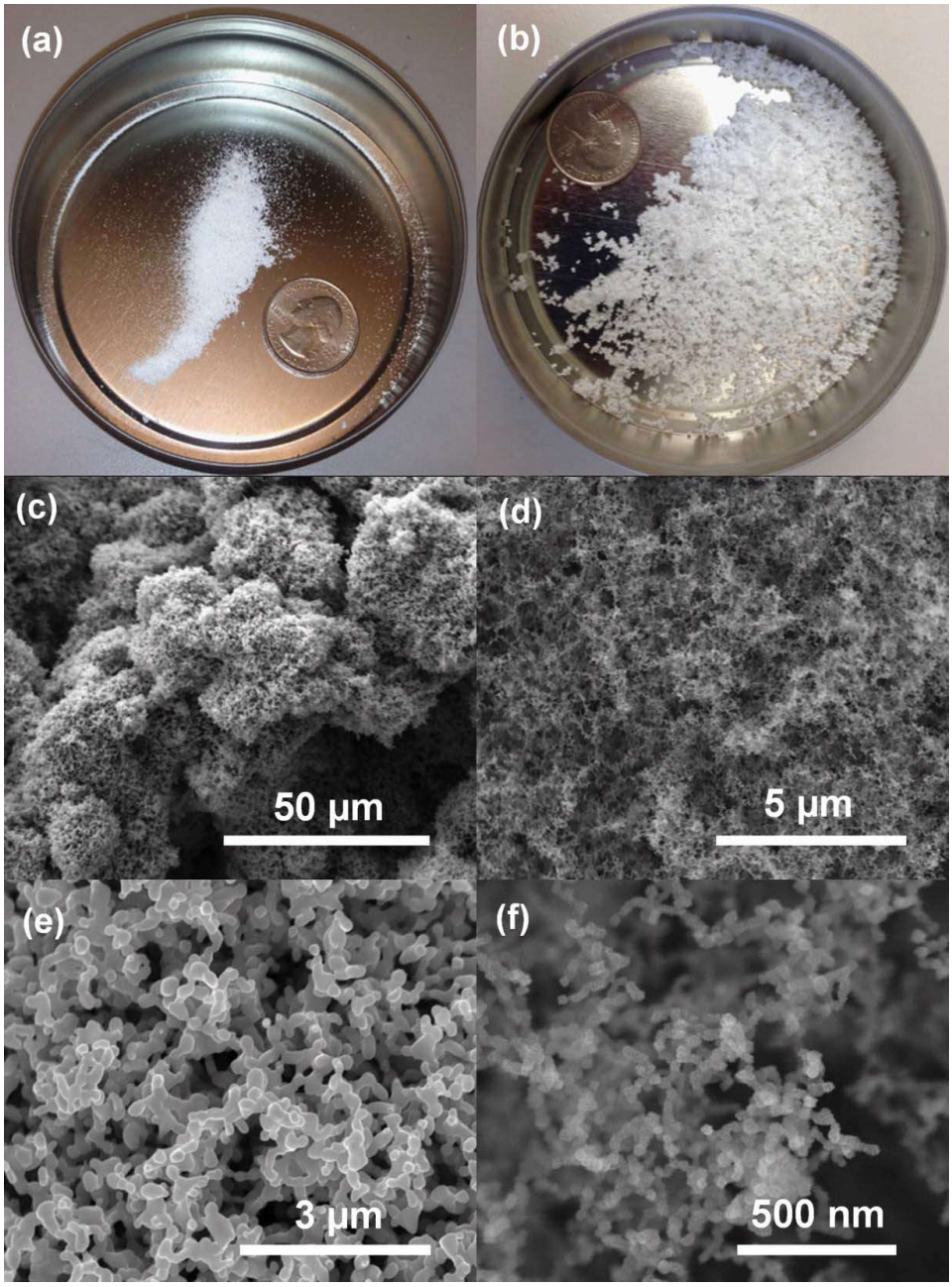

Figure 6.6. (a) and (b) Optical photographs of TG1 and TG2 bulk samples. (c) and (e) SEM images of TG1 particles at different magnifications. (d) and (f) SEM images of TG2 particles at different magnifications.

Our results of the monomer number size distribution are shown in Figure 6.7. The average monomer size of the TG1 sample was an order of magnitude greater than that of TG2. This is because of the increased particle growth and sintering rate in a higher temperature reaction system, such as that of TG1 (Kammler et al. 2001; Cho and Biswas 2006). Figure 6.8 shows the SSA versus monomer diameter of TG1 and TG2 samples. In the same figure, comparison of our results with previous findings is made (Jang and Kim 2001; Jiang et al. 2007; Suttiponparnit et al. 2011). The SSA values of aerosol gels produced in this work were on the lower side owing to the larger monomer diameter and high degree of necking between the monomers.

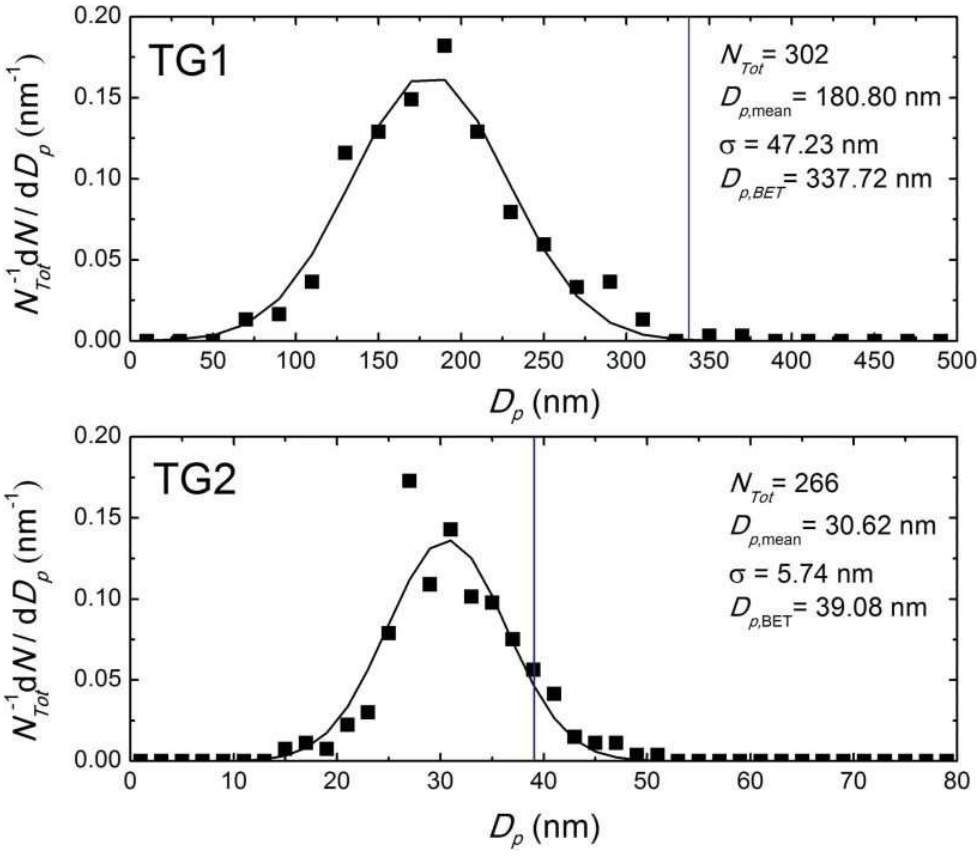

Figure 6.7. Monomer size distribution of TG1 and TG2 (squares), as determined by SEM analysis. Vertical solid lines represent the values determined using BET technique.

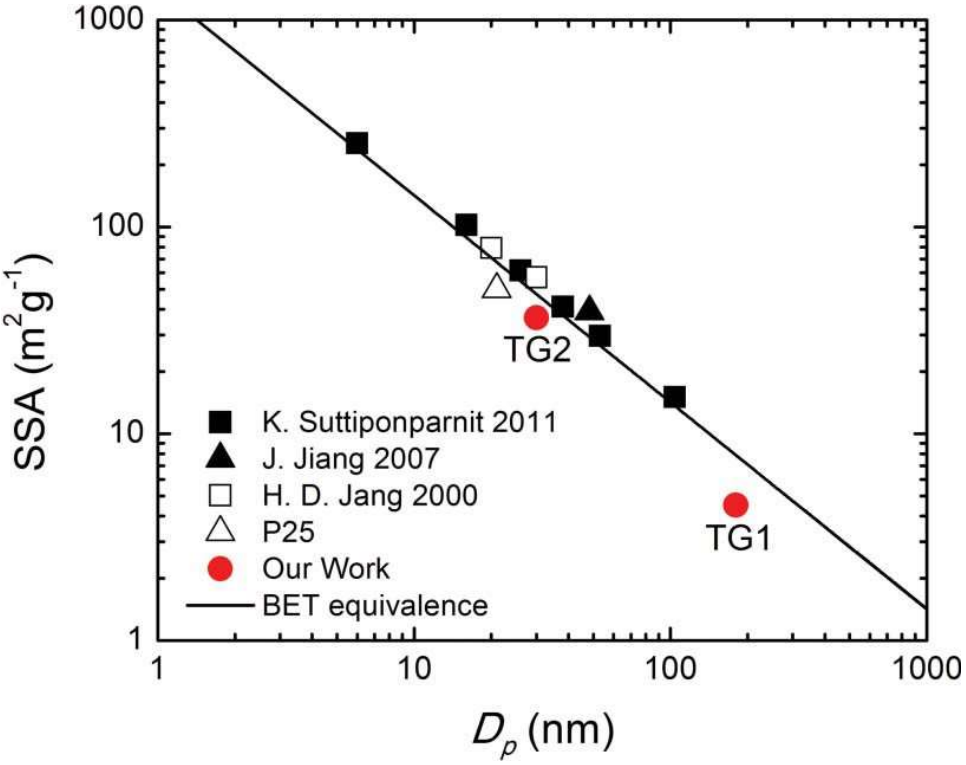

Figure 6.8. Specific surface area (SSA) of TG1 and TG2 are functions of monomer size, and its comparison with previous findings by different research groups. Note: BET equivalence monomer size $D_{p,BET} = 6/(SSA \cdot \rho)$.

Figure 6.9 shows the X-ray diffraction patterns of TiO_2 gel samples. Monocrystalline anatase and rutile phases of TiO_2 were identified in TG2 and TG1, respectively. Their distinct crystal phase shows up due to their synthesizing temperature conditions. Past studies showed that TiO_2 crystal formation always starts from anatase phase owing to its lower surface free energy (Yang et al. 1996; Banfield 1998; Ghosh et al. 2004). Anatase to rutile (ATR) phase transformation has been theorized to occur when temperature of the system is high enough to sustain the nonreversible rearrangement of the crystal lattice structure (Hanaor and Sorrell 2011). Thus, the kinetics of ATR transformation is temperature dependent and has been shown to be "immeasurably slow" for temperatures below 610 °C (Rao 1961). This threshold is very close to the operating temperature of our flame used for synthesizing TG2. Hence, it is no surprise that we observed pure anatase

phase comprising the TG2 sample. On the other hand, the higher temperature used for synthesizing TG1 led to its complete ATR transformation in its composition.

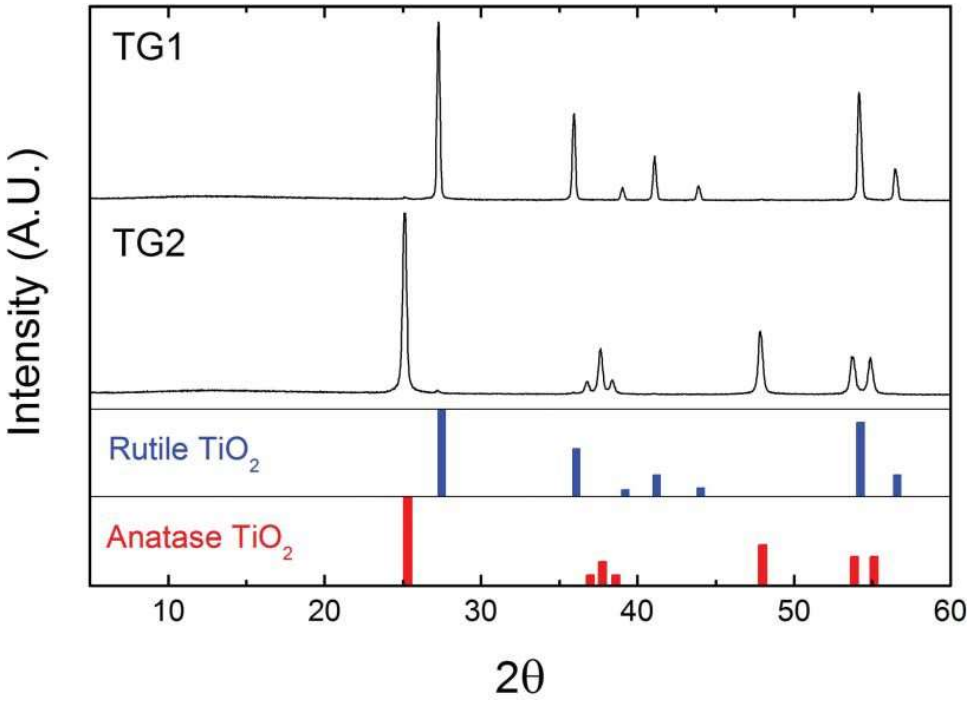

Figure 6.9. X-ray diffraction patterns of TG1 and TG2 and their comparison with the standard spectra of pure rutile and anatase TiO_2.

Figure 6.10 shows the UV-Vis absorbance spectra of TG1 and TG2 in comparison to that of the industry-standard P25 (Sigma-Aldrich, St. Louis, MO, USA). The absorbance spectrum of TG2 demonstrates a similar pattern to P25 due to both materials' similar crystalline composition (anatase) and monomer size. The absorbance shoulder in both samples occurs around 325 nm of the incident light wavelength. Beyond this point, absorbance attenuates with increasing wavelength. This is in good agreement with the well-investigated optical properties of TiO_2 (Ceylan et al. 2013). On the contrary, TG1 demonstrates a rather unconventional absorbance spectrum: a flat and slowly attenuating curve. One possible explanation of this behavior could be

the enhancement in scattering by the larger monomers of the TG1 sample. When monomer size reaches as high as 300 nm, the scattering efficiency dominates over absorption irrespective of change in wavelengths in the UV-Vis spectrum.

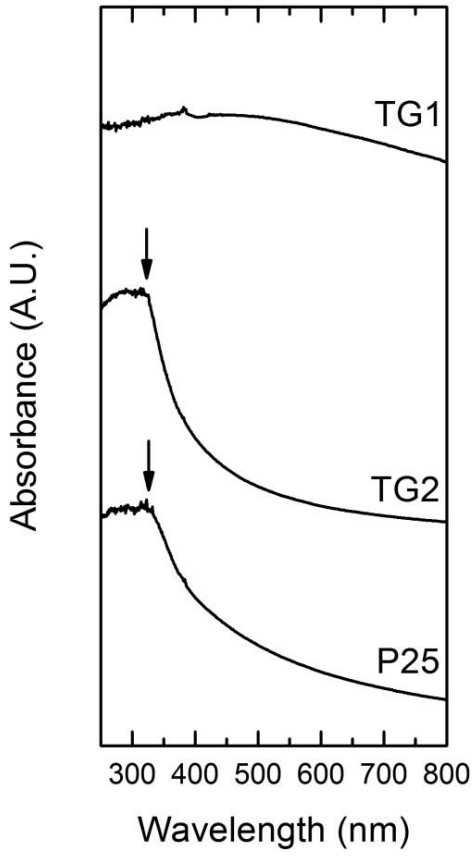

Figure 6.10. UV-Vis absorbance spectra of TG1 and TG2 particles and their comparison with the spectrum of TiO_2 P25. The arrows represent the absorbance shoulders observed in the spectra of TG2 and P25 samples.

6.5 Conclusion

In this work, the phenomenon of aerosol gelation in a down-fired, buoyancy-opposed diffusion flame systems was utilized to synthesize TiO_2 gels. The in-flame aerosol trapping effect was reproduced under varying flame operating conditions of N_2 dilution ranging between 0 and 30 lpm.

The corresponding flame temperatures ranged between 1250 °C and 590 °C. Control of the morphology and crystalline phase of TiO_2 aerosol gels was achieved by exploiting the dependency of monomer growth rate and crystal transformation on temperature. Doping of TiO_2 with soot particles was avoided by operating the flame in extreme temperature conditions.

The effective densities of TiO_2 aerosol gels synthesized in high (TG1) and low (TG2) temperature conditions were measured to be 0.025 and 0.021 g/cm^3, respectively, before mechanical crushing, and 0.829 and 0.838 g/cm^3, respectively, after crushing. The average monomer diameters of TG1 and TG2 samples were 181 and 31 nm, respectively, based on SEM images, and were 338 and 39 nm, respectively, based on measurements by the BET technique. The large difference in monomer size distribution was primarily attributed to the difference in particle growth rates at different operating temperature conditions. Monocrystallite rutile and anatase phases of TiO2 were detected in TG1 and TG2, respectively, with high degree of purity. TG2 demonstrated typical UV-Vis absorbance spectrum associated with anatase TiO_2; while an overall flattened absorbance spectrum was seen in the case of TG1. Further investigation is required to fully understand this nonvarying behavior of absorbance with changing wavelength.

Future research needs to be directed toward in situ studies of gel formation and aerosol growth mechanism using small angle static light scattering and thermophoretic sampling techniques (Dobbins and Megaridis 1987; Sorensen et al. 1992). How the gel formation mechanism changes as a function of temperature and other flame parameters is another uninvestigated area of research. Finally, efforts will be made in subsequent work to present more accurate measurements of temperature profile after applying proper radiative corrections and particle residence time.

6.6 References

Akbari, B., Tavandashti, M. P., and Zandrahimi, M. (2011). Particle Size Characterization of Nanoparticles – A Practical Approach. *Iran. J. Mater. Sci. Eng*., 8:48–56.

Banfield, J. (1998). Thermodynamic Analysis of Phase Stability of Nanocrystalline Titania. *J. Mater. Chem.*, 8:2073–2076.

Brinker, C. J., and Scherer, G. W. (2013). Sol-Gel Science: The Physics and Chemistry of Sol-Gel Processing. Academic Press, San Diego, CA, 518–526

Ceylan, H., Ozgit-Akgun, C., Erkal, T. S., Donmez, I., Garifullin, R., Tekinay, A. B., Usta, H., Biyikli, N., and Guler, M. O. (2013). Size-Controlled Conformal Nanofabrication of Biotemplated Three-Dimensional TiO_2 and ZnO Nanonetworks. *Sci. Rep.*, 3:2306–2313.

Chakrabarty, R. K., Moosmüller, H., Garro, M. A., and Stipe, C. B. (2012). Observation of Superaggregates from a Reversed Gravity Low-Sooting Flame. *Aerosol Sci. Technol.*, 46:i–iii.

Chakrabarty, R. K., Novosselov, I. V., Beres, N. D., Moosmüller, H., Sorensen, C. M., and Stipe, C. B. (2014). Trapping and Aerogelation of Nanoparticles in Negative Gravity Hydrocarbon Flames. *Appl. Phys. Lett.*, 104:243103.

Cho, K., and Biswas, P. (2006). Sintering Rates for Pristine and Doped Titanium Dioxide Determined Using a Tandem Differential Mobility Analyzer System. *Aerosol Sci. Technol*., 40:309–319.

Dhaubhadel, R., Gerving, C. S., Chakrabarti, A., and Sorensen, C. M. (2007). Aerosol Gelation: Synthesis of a Novel, Lightweight, High Specific Surface Area Material. *Aerosol Sci. Technol*., 41:804–810.

Dhaubhadel, R., Rieker, T., Chakrabarti, A., and Sorensen, C. M. (2012). Synthesis of Silica Aerosol Gels via Controlled Detonation. *Aerosol Sci. Technol*., 46:596–600.

Dobbins, R. A., and Megaridis, C. M. (1987). Morphology of Flame-Generated Soot as Determined by Thermophoretic Sampling. *Langmuir*, 3:254–259.

Ghosh, T., Dhabal, S., and Datta, A. (2004). Erratum: On Crystalline Size Dependence of Phase Stability of Nanocrystalline TiO_2. *J. Appl. Phys.*, 95:408–408.

Hanaor, D. A., and Sorrell, C. C. (2011). Review of the Anatase to Rutile Phase Transformation. *J. Mater. Sci*., 46:855–874.

Hindasageri, V., Vedula, R., and Prabhu, S. (2013). Thermocouple Error Correction for Measuring the Flame Temperature with Determination of Emissivity and Heat Transfer Coefficient. *Rev. Sci. Instrum*., 84:024902.

Jang, H. D., and Kim, S.-K. (2001). Controlled Synthesis of Titanium Dioxide Nanoparticles in a Modified Diffusion Flame Reactor. *Mater. Res. Bull.*, 36:627–637.

Jiang, J., Chen, D.-R., and Biswas, P. (2007). Synthesis of Nanoparticles in a Flame Aerosol Reactor with Independent and Strict Control of Their Size, Crystal Phase, and Morphology. *Nanotechnology*, 18:285603.

Kammler, H. K., Mädler, L., and Pratsinis, S. E. (2001). Flame Synthesis of Nanoparticles. *Chem. Eng. Technol.*, 24:583–596.

Perkampus, H.-H., Grinter, H.-C., and Threlfall, T. (1992). UV-VIS Spectroscopy and Its Applications. Springer: New York.

Rao, C. (1961). Kinetics and Thermodynamics of the Crystal Structure Transformation of Spectroscopically Pure Anatase to Rutile. *Can. J. Chem.*, 39:498–500.

Shannon, K., and Butler, B. (2003). A Review of Error Associated with Thermocouple Temperature Measurement in Fire Environments. In *Second International Wildland Fire*

Ecology and Fire Management Congress and Fifth Symposium on Fire and Forest Meteorology. American Meteorological Society, Orlando, FL, pp. 16–20.

Siefering, K., and Griffin, G. (1990). Growth Kinetics of CVD TiO_2: Influence of Carrier Gas. *J. Electrochem. Soc*., 137:1206–1208.

Sorensen, C. M., Cai, J., and Lu, N. (1992). Light-Scattering Measurements of Monomer Size, Monomers per Aggregate, and Fractal Dimension for Soot Aggregates in Flames. *Appl. Opt.*, 31:6547–6557.

Sorensen, C. M., and Chakrabarti, A. (2011). The Sol to Gel Transition in Irreversible Particulate Systems. *Soft Matter*, 7:2284–2296.

Sorensen, C. M., Hageman, W., Rush, T., Huang, H., and Oh, C. (1998). Aerogelation in a Flame Soot Aerosol. *Phys. Rev. Lett*., 80:1782–1785.

Suttiponparnit, K., Jiang, J., Sahu, M., Suvachittanont, S., Charinpanitkul, T., and Biswas, P. (2011). Role of Surface Area, Primary Particle Size, and Crystal Phase on Titanium Dioxide Nanoparticle Dispersion Properties. *Nanoscale Res. Lett*., 6:27.

Yang, G., Zhuang, H., and Biswas, P. (1996). Characterization and Sinterability of Nanophase Titania Particles Processed in Flame Reactors. *Nanostruct. Mater*., 7:675–689.

Chapter 7: Conclusion and Future Work Directions

This chapter summarizes the major findings of the works presented in this dissertation and provides suggestions on the future research directions.

The ubiquitous ballistic-to-diffusive (BD) transition in random walks, which has been shown to influence the aggregation kinetics near the gelling condition, was studied using directional statistics (Chapter 2). The BD transition for a two-dimensional (2-d) random walk was modelled using the time-evolution of the walkers turning angle distribution $P(\theta)$, which evolves from a delta function to a circular uniform distribution with increasing time. This flattening of $P(\theta)$ can be accurately parameterized using a wrapped Cauchy distribution (WCD) with a shape factor decreasing from unity to zero. Good agreements were observed between our directional statistical description and the traditionally used power-law scaling relationship for walkers mean squared displacement (MSD). The kinetics of BD transition was established with mathematical expressions that connect the shape factor of WCD, the power-law exponent of MSD, and time. Future works should be directed toward generalizing the BD transition kinetics to three-dimensional random (3-d) walk. It worth to note that the spherical uniform distribution in 3-d differs from the circular uniformity in 2-d with a biased $\sin(|\theta|)$ functionality. Thus, the onset of diffusional motion should be modelled using the flattening of a $Q(\theta) = \frac{P(\theta)/\sin(|\theta|)}{\int P(\theta)/\sin(|\theta|)d\theta}$, instead of $P(\theta)$. Another interesting research topic is to investigate the transition behavior for walkers that are subject to geometric confinements in both 2-d and 3-d spaces.

The influence of fractal morphology on aerosol mass-mobility relationship was investigated for aggregates produced via diffusion-limited cluster-cluster aggregation (DLCA) in cluster-dilute regime (Chapter 3). The Empirical relationship was established between the aggregate morphological parameters and mass-mobility scaling parameters. Furthermore, the decreasing

trend in aggregates mobility diameter with an increase in k_f, was interpreted with the concept of apparent screening between monomers at changing degree of shape anisotropy. Future studies on this topic should incorporate a more realistic aggregate morphology, such as poly-dispersed monomers and monomer necking, into the parameterization of mass-mobility relationship.

The kinetics of aerosol gelation was comprehensively studied using high temporal-resolution Monte Carlo simulations of irreversible DLCA systems (chapter 4). System independent scaling relationships were established to describe the transition kinetics in both the pre-IGP and the previously understudied post-IGP regimes. Improved parameterizations were provided for the important characteristic timescale parameters in the existing theoretical framework of aerosol aggregation and gelation. A new timescale parameter predicting the completeness gelation in the post-IGP regime was introduced. A new mechanism, which involves the aggregation of gels, was introduced to interpret the particle growth in extremely dense DLCA systems. Future studies should focus on investigating the onset of this distinct late-stage kinetics in DLCA with a monomer volume fraction in the range between 0.05 and 0.1.

Fractal scaling law for the packing density of soot aggregates produced from an ethylene-oxygen buoyancy-opposed flame (BOF) was experimentally mapped out across five orders of magnitude length scale (chapter 5). An inflection in the power-law scaling relationship was observed in the super-micron size range, which is characterized with a decrease in aggregates fractal dimension (D_f) value from about 2.5 to 1.7. The reappearance of the small D_f indicates that a cluster-cluster aggregation of gels takes over the late-stage growth mechanism for the millimeter-sized particles. Future research should be directed to parameterizing the aggregation kernel of the gel particles trapped in the recirculation zone of the BOF reactor.

Controlled synthesis of titanium dioxide (TiO_2) aerosol gels was realized using a methane-oxygen BOF aerosol reactor with titanium tetraisopropoxide precursor (Chapter 6). The in-flame aerosol trapping effect was reproduced in the BOF reactor at a variety of operating conditions. Control of flame temperature was established in the range between c.a. 600 and 1300 °C with the application of nitrogen dilution at variable flow rates. Control of the morphology and crystal phase of the TiO_2 was achieved by exploiting the dependencies of monomer sintering and crystal phase transformation on temperature. Future studies should focus on experimentally mapping out the temperature-time history of the aerosol gel particles in the BOF reactor operated at changing conditions.

Appendix I. Supporting Materials for Chapter 2

A1.1 Determining θ from Trajectory

A1.2 Enumeration of $\theta_{i,1}$

A1.3 Enumeration of $\theta_{i,2}$

A1.1 Determining θ from Trajectory

The turning angle θ of could be determined from three successive positions of the walker, $[x(t), y(t)]$, $[x(t+\tau), y(t+\tau)]$ and $[x(t+2\tau), y(t+2\tau)]$, which are termed as A, B, and C, respectively. We calculate θ by finding the angle of $\overrightarrow{\mathrm{BC}}$ relative to $\overrightarrow{\mathrm{AB}}$. Note that θ takes value between -π to π and counterclockwise is regarded positive for angle. Define φ_{AB} to be the angle of vector $\overrightarrow{\mathrm{AB}}$ relative to positive x-axis. Note that $\varphi_{\mathrm{AB}} \in [0, 2\pi)$, and it increases as $\overrightarrow{\mathrm{AB}}$ rotates around A along counterclockwise direction ($\varphi_{\mathrm{AB}} = 0$ when $\overrightarrow{\mathrm{AB}}$ is parallel to x and points to the positive direction). We calculate the φ_{AB} as follows:

$$\varphi_{\mathrm{AB}} = k\pi + \arctan\left[\frac{y(t+\tau) - y(t)}{x(t+\tau) - x(t)}\right]$$

$$\text{and } k = \begin{cases} 0 & \text{if } x(t+\tau) > x(t) \text{ and } y(t+\tau) > y(t) \\ 1 & \text{if } x(t+\tau) < x(t) \\ 2 & \text{if } x(t+\tau) > x(t) \text{ and } y(t+\tau) < y(t) \end{cases} \tag{A1.1}$$

Similarly, we calculate the angle φ_{BC} of vector $\overrightarrow{\mathrm{BC}}$ relative to positive x-axis:

$$\varphi_{\mathrm{BC}} = k\pi + \arctan\left[\frac{y(t+2\tau) - y(t+\tau)}{x(t+2\tau) - x(t+\tau)}\right]$$

$$\text{and } k = \begin{cases} 0 & \text{if } x(t+2\tau) > x(t+\tau) \text{ and } y(t+2\tau) > y(t+\tau) \\ 1 & \text{if } x(t+2\tau) < x(t+\tau) \\ 2 & \text{if } x(t+2\tau) > x(t+\tau) \text{ and } y(t+2\tau) < y(t+\tau) \end{cases} \tag{A1.2}$$

At last, we calculate θ using φ_{AB} and φ_{BC}:

$$\theta = 2m\pi + \varphi_{\mathrm{BC}} - \varphi_{\mathrm{AB}}$$

$$\text{and } m = \begin{cases} 0 & \text{if } |\varphi_{BC} - \varphi_{AB}| < \pi \\ -1 & \text{if } |\varphi_{BC} - \varphi_{AB}| > \pi \text{ and } \varphi_{BC} > \varphi_{AB} \\ 1 & \text{if } |\varphi_{BC} - \varphi_{AB}| > \pi \text{ and } \varphi_{BC} < \varphi_{AB} \end{cases} \quad \text{(A1.3)}$$

A1.2 Enumeration of $\theta_{i,1}$

Define that a walker is seen at positions O, A, B, C and D when t increments by τ_i. Figure A1.1 demonstrates the relationship between the turning angles and the corresponding vector pairs. Note that the following discussion is based on the assumption that the net displacement δ_i during τ_i is constant, or $|\overrightarrow{OA}| = |\overrightarrow{AB}| = |\overrightarrow{BC}| = |\overrightarrow{CD}| = \delta_i$. The counterclockwise direction is regarded positive for angles.

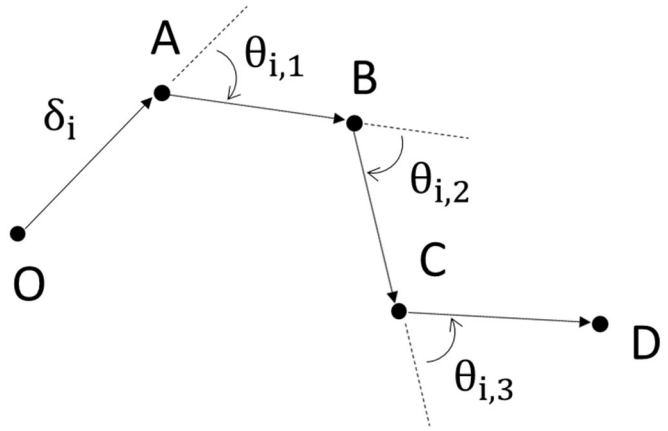

Figure A1.1. When the walker is observed with timescale τ_i, it is seen at five successive locations O, A, B, C and D.

Next, set up a Cartesian coordinate with O serving as the origin and $\overrightarrow{OB}$ representing the positive x-axis, as shown in Figure A1.2. Define ω to be the angle of $\overrightarrow{OA}$ relative to positive y-axis. One

could observe that the range for $\theta_{i,1}$ is unrestricted, and $\theta_{i,1}$ takes value from 0 to -2π twice before all possible configurations are exhausted. Specifically, an enumeration is outlined in the following:

(i). When ω decreases from 0 to $-\pi/2$, correspondingly A migrates from (0, δ_i) through the 1st quadrant to (δ_i, 0), $\theta_{i,1}$ increases from $-\pi$ to 0.

(ii) When ω decreases from $-\pi/2$ to $-\pi$, correspondingly A migrates from (δ_i, 0) through the 2nd quadrant to (0, $-\delta_i$), $\theta_{i,1}$ increases from 0 to π.

(iii). When ω decreases from $-\pi$ to $-3\pi/2$, correspondingly A migrates from (0, $-\delta_i$) through the 3rd quadrant to ($-\delta_i$, 0), $\theta_{i,1}$ increases from $-\pi$ to 0.

(iv). When ω decreases from $-3\pi/2$ to -2π, correspondingly A migrates from ($-\delta_i$, 0) through the 4th quadrant to (0, δ_i), $\theta_{i,1}$ increases from 0 to π.

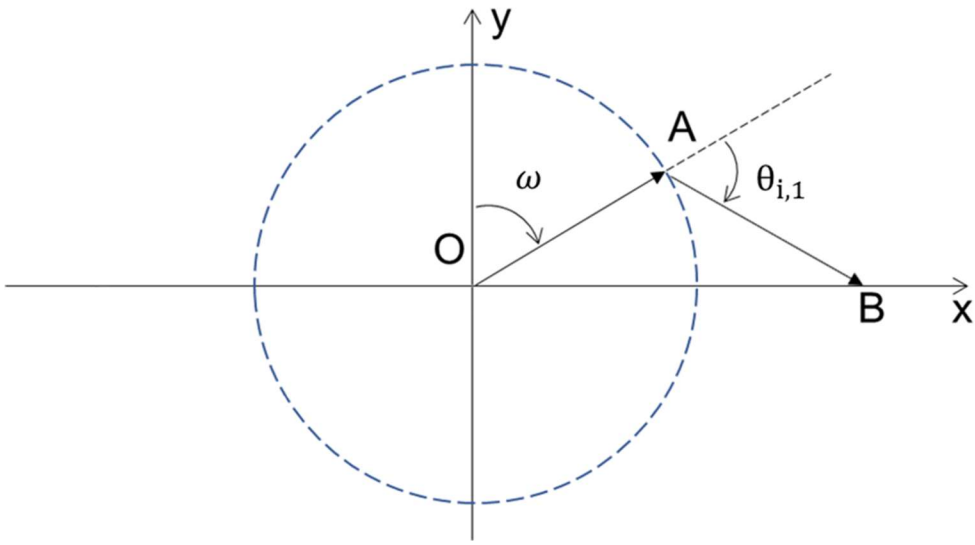

Figure A1.2. Enumeration of $\theta_{i,1}$.

A1.3 Enumeration of $\theta_{i,2}$

The range for $\theta_{i,2}$ is discussed under the condition that both $\theta_{i,1}$ and θ_{2i} are specified. Note that $\theta_{i,1}$ could take any arbitrary value but $\theta_{2i} = 0$. As shown in Figure A1.3, segment PQ which is perpendicular to x-axis passes it through B. The half-circle (dashed curve) has a radius of δ_i and it intercepts with the x-axis at R. Note that since vector $\overrightarrow{OB}$ is set as positive x, the condition $\theta_{2i} = 0$ requires that $\overrightarrow{BD}$ also resides on x-axis and points to the positive direction. In other words, vector $\overrightarrow{CD}$ has to connect with x-axis at the position D satisfying $x_D > x_B$.

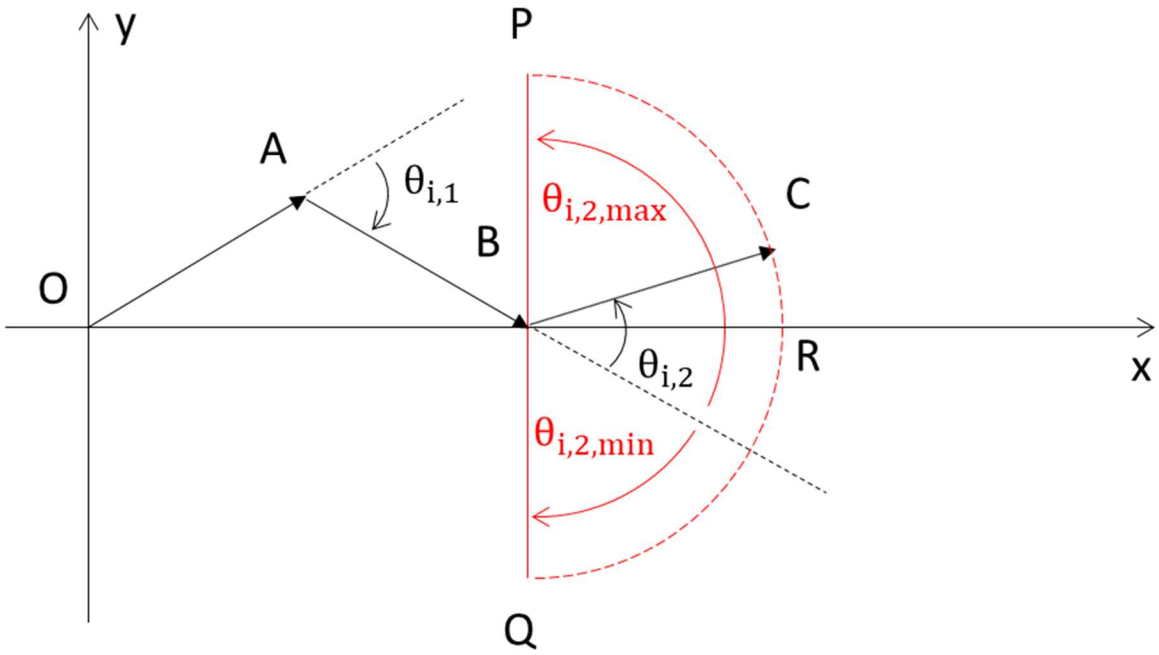

Figure A1.3. Enumeration of $\theta_{i,2}$.

The half circle $\overset{\frown}{PRQ}$ exhausts all possible positions for C under the premise of $\theta_{2i} = 0$. In other words, C could only reside on $\overset{\frown}{PRQ}$ such that the vector $\overrightarrow{CD}$ could subsequently connect x-axis at

D with a constant length δ_i. The maximum and minimum of $\theta_{i,2}$ (indicated in Fig. A1.3 by the red arrows) are dictated by the value of $\theta_{i,1}$, which could be written as: $\theta_{i,2,min} = -\frac{1}{2}(\theta_{i,1} + \pi)$ and $\theta_{i,2,max} = -\frac{1}{2}(\theta_{i,1} - \pi)$.

Appendix II. Supporting Materials for Chapter 4

A2.1 Derivation of Equation (4.2)

The off-lattice DLCA model operates with a unit timescale t_s during which monomers move by a root-mean-squared-displacement $\sqrt{\langle \delta^2 \rangle}$ that equals the monomer diameter $2a$. In three-dimensional space,

$$\langle \delta^2 \rangle = 6Dt \tag{A2.1}$$

where $D = k_B T/(6\pi\mu a)$ is the monomer diffusivity when under Stokes-Einstein diffusion. Substituting the $\langle \delta^2 \rangle$, t, and D by $4a^2$, t_s, and $k_B T/(6\pi\mu a)$, respectively, Eq. (A2.1) becomes $t_s = 4\pi\mu a^3/k_B T$, which is Eq. (4.2) in chapter 4.

A2.2 Determination of t_{IGP} from DLCA

The determination of t_c from DLCA data follows the rule $\langle N(t_{IGP})\rangle = N_{IGP}$. Visually, this treatment is shown in Figure A2.1. Note that the characteristic time is reported in units of t_s.

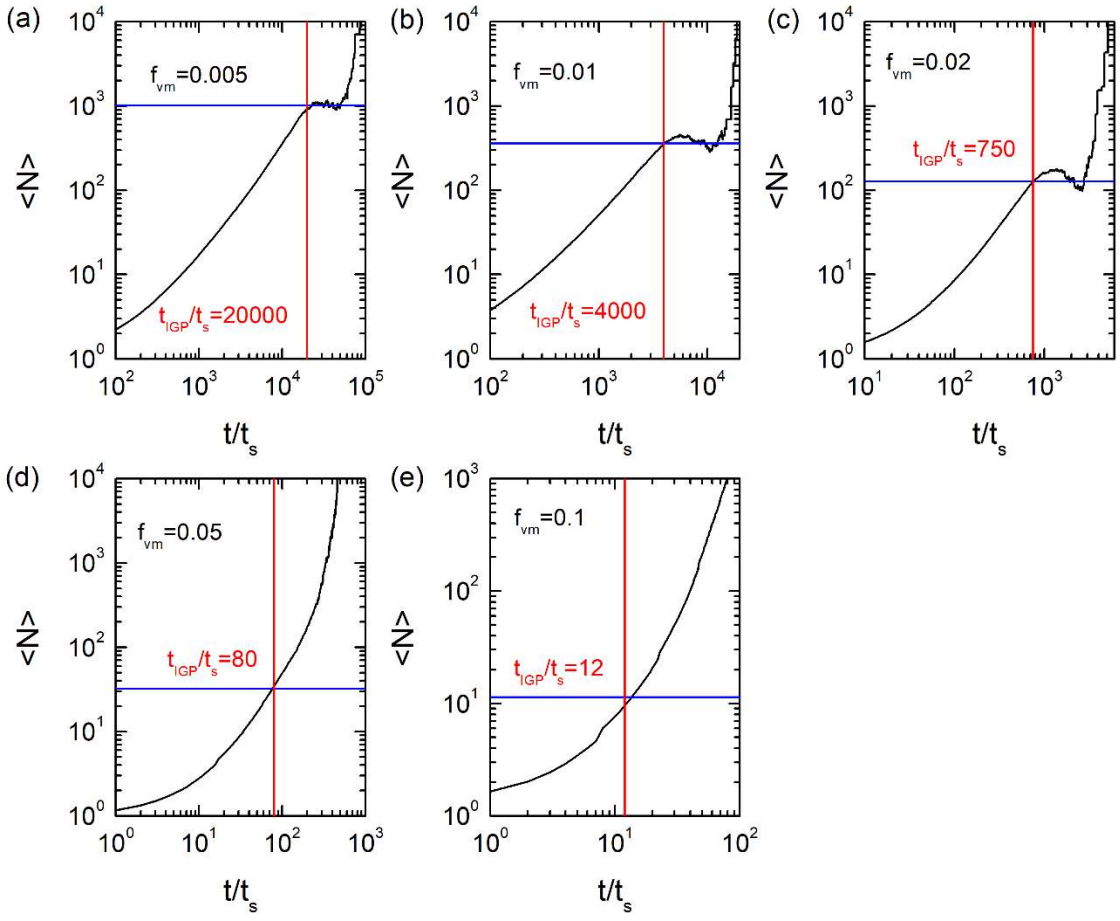

Figure A2.1. Increase in $\langle N\rangle$ as a function of simulation time t/t_s for DLCA starting out with f_{vm} = 0.005 (a), 0.01 (b), 0.02 (c), 0.05 (d), and 0.1 (e). Black solid curves represent <*N*>. Blue solid lines mark the values for N_{IGP} calculated per Eq. (4.3) in chapter 4. Red lines mark the critical t_{IGP}/t_s, at which <*N*> reaches the N_{IGP} value for that system.

A2.3 Derivation of Equation (4.4)

The volume occupied by the solid components of an aggregates is $V_m = \frac{4}{3}\pi a^3 N$. For the average cluster at IGP, we have,

$$V_{m,IGP} = \frac{4}{3}\pi a^3 N_{IGP} \tag{A2.2}$$

Combining $N_{IGP} = k_f\left(R_{g,IGP}/a\right)^{D_f}$ and $R_{g,IGP} = a\left[f_{vm}^{-1}k_f\left(\frac{D_f}{D_f+2}\right)^{3/2}\right]^{1/(3-D_f)}$ (which are respectively the Eq. (4.3a) and (4.3b) in Chapter 4), we get,

$$N_{IGP} = f_{vm}^{D_f/(D_f-3)}k_f^{3/(3-D_f)}\left(\frac{D_f}{D_f+2}\right)^{3D_f/(6-2D_f)} \tag{A2.3}$$

Substituting the N_{IGP} in Eq. (A2.2) using (A2.3), we get the dimensionless form of aggregate volume,

$$\frac{V_{m,IGP}}{a^3} = \frac{4}{3}\pi f_{vm}^{D_f/(D_f-3)}k_f^{3/(3-D_f)}\left(\frac{D_f}{D_f+2}\right)^{3D_f/(6-2D_f)} \tag{A2.4}$$

The perimeter volume of an aggregates is $V_p = \frac{4}{3}\pi R^3$, where R is the perimeter radius (Oh and Sorensen 1997) and it is related to R_g per $R = R_g\left[\left(D_f+2\right)/D_f\right]^{1/2}$. Thus, for the average cluster at IGP, we have,

$$V_{p,IGP} = \frac{4}{3}\pi R_{g,IGP}^3\left(\frac{D_f+2}{D_f}\right)^{3/2} \tag{A2.5}$$

Substituting the $R_{g,IGP}$ in Eq. (A2.5) using $R_{g,IGP} = a\left[f_{vm}^{-1}k_f\left(\frac{D_f}{D_f+2}\right)^{3/2}\right]^{1/(3-D_f)}$ (which is Eq. (4.3b) in Chapter 4), we get the dimensionless form of perimeter volume,

$$\frac{V_{p,IGP}}{a^3} = \frac{4}{3}\pi f_{vm}^{3/(D_f-3)}k_f^{3/(3-D_f)}\left(\frac{D_f}{D_f+2}\right)^{3D_f/(6-2D_f)} \tag{A2.6}$$

Combining Eq. (A2.4) and (A2.6), we get the expression for the free volume within the perimeter volume of the average clusters at IGP,

$$\frac{V_{p,IGP}-V_{m,IGP}}{a^3} = \frac{4}{3}\pi(1-f_{vm})\left[k_f\left(\frac{D_f}{D_f+2}\right)^{D_f/2}f_{vm}^{-1}\right]^{3/(3-D_f)} \tag{A2.7}$$

The Stokes-Einstein diffusivity of the average cluster at IGP is written as $D_{IGP} = \frac{k_BT}{6\pi\mu R_{g,IGP}}$, and when combined with $t_s = \frac{4\pi\mu a^3}{k_BT}$ (which is Eq. (4.2) in Chapter 4), it yields to a dimensionless expression:

$$\frac{t_sD_{IGP}}{a^2} = \frac{2}{3}\left(\frac{R_{g,IGP}}{a}\right)^{-1} \tag{A2.8}$$

Substituting the $R_{g,IGP}$ using $R_{g,IGP} = a\left[f_{vm}^{-1}k_f\left(\frac{D_f}{D_f+2}\right)^{3/2}\right]^{1/(3-D_f)}$ (which is Eq. (4.3b) in Chapter 4), Eq. (A2.8) becomes:

$$\frac{t_sD_{IGP}}{a^2} = \frac{2}{3}\left[f_{vm}^{-1}k_f\left(\frac{D_f}{D_f+2}\right)^{3/2}\right]^{1/(D_f-3)} \tag{A2.9}$$

The characteristic time $t_d = \frac{\left(V_{p,IGP} - V_{m,IGP}\right)^{2/3}}{6D_{IGP}}$ can be reached by rearranging Eq. (A2.1). After being combined with Eq. (A2.7) and (A2.9), the expression of t_d yields to the dimensionless form shown in Chapter 4 as Eq. (4.4):

$$\frac{t_d}{t_s} = \frac{1}{4}\left[\frac{4}{3}\pi(1 - f_{vm})\right]^{2/3}\left(\frac{D_f}{D_f + 2}\right)^{(2D_f+3)/(6-2D_f)}\left(k_f f_{vm}^{-1}\right)^{3/(3-D_f)}$$

A2.4 Determination of t_c from DLCA

The determination of t_c from DLCA data follows the rule $n_{tot}(t_c) = n_{tot,0}/2$, according to $\frac{n_{tot}}{n_{tot,0}} = \left(1 + \frac{t}{t_c}\right)^{-1}$ (which is Eq. (4.5) in Chapter 4). Visually, this treatment is shown in Figure A2.2. Note that the characteristic time is reported in units of t_s.

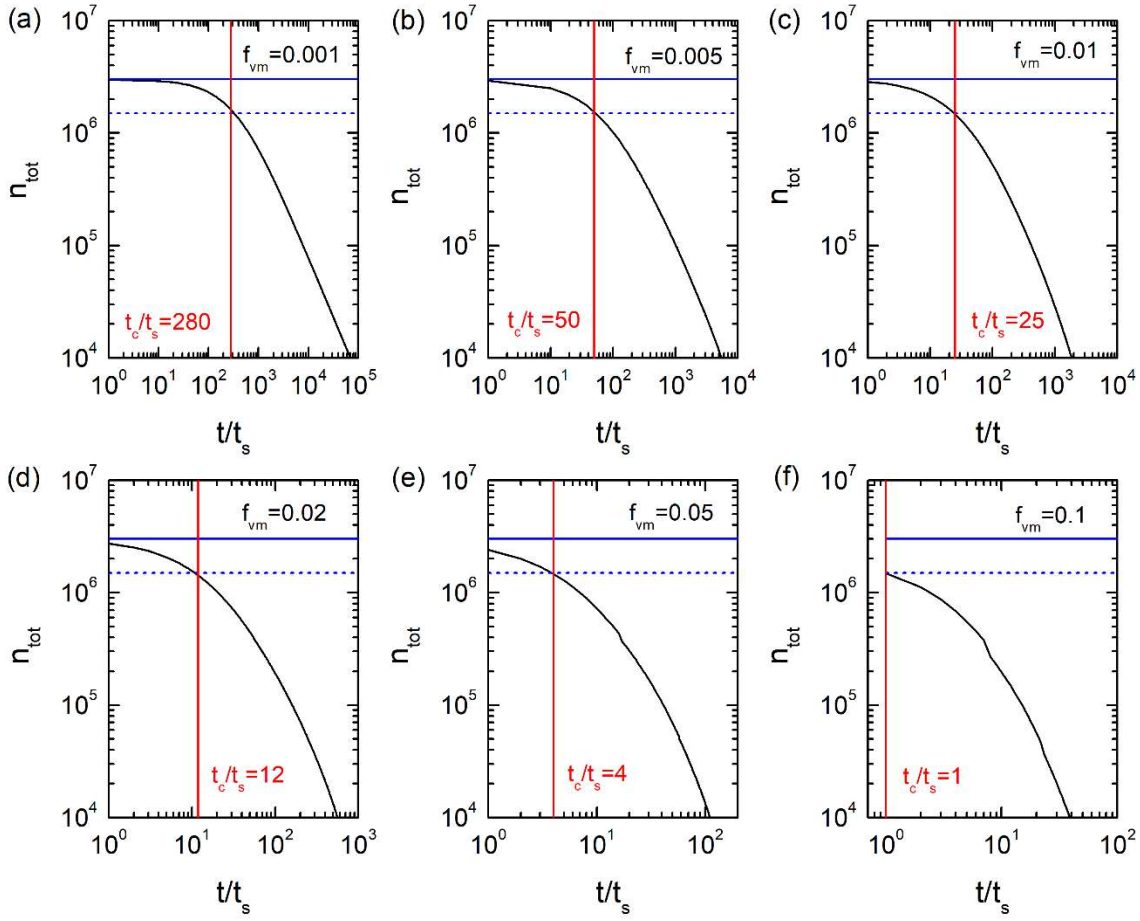

Figure A2.2. Decrease in n_{tot} as a function of simulation time t/t_s for DLCA starting out with f_{vm} = 0.001 (a), 0.005 (b), 0.01 (c), 0.02 (d), 0.05 (e), and 0.1 (f). Black solid curves represent n_{tot}. Blue solid-lines and dotted lines mark the values for $n_{tot,0}$ and $n_{tot,0}/2$, respectively. Red lines mark the critical t_c/t_s, at which n_{tot} reaches the value of $n_{tot,0}/2$ for that system.

A2.5 Derivation of Equation (4.10)

Per Ref. (Oh and Sorensen 1997), solution to SE with homogenous kernel yields the average DLCA cluster mass $\langle N \rangle \propto (1 + t/t_c)^z$, and we use the following power-law relationship to describe the particle growth in the cluster-dense regime:

$$\langle N \rangle = b(1 + t/t_c)^z \tag{A2.10}$$

where b and z are assumed to take constant values for simplicity. Combining Eq. (A2.10) and Eq. (A2.3) under the condition $\langle N \rangle = N_{IGP}$ at $t = t_{IGP}$ gives:

$$t_{IGP} = t_c \left[b^{-\frac{1}{z}} f_{\mathrm{vm}}^{\frac{D_f}{(D_f-3)z}} \left(\frac{D_f}{D_f+2} \right)^{\frac{3D_f}{(6-2D_f)z}} k_f^{\frac{3}{(3-D_f)z}} - 1 \right] \tag{A2.11}$$

Replacing the t_c with the right-hand-side of $\frac{t_c}{t_s} = \frac{1}{4}(f_{vm}^{-1} - \Phi_P^{-1})$ (which is Eq. (4.9) in Chapter 4), we get:

$\frac{t_{IGP}}{t_s} = \frac{1}{4}(f_{vm}^{-1} - \Phi_P^{-1}) \left[b^{-\frac{1}{z}} f_{vm}^{\frac{D_f}{(D_f-3)z}} \left(\frac{D_f}{D_f+2} \right)^{\frac{3D_f}{(6-2D_f)z}} k_f^{\frac{3}{(3-D_f)z}} - 1 \right]$, which is Eq. (4.10) in Chapter 4

A2.6 The power-law growth of DLCA aggregates in the cluster-dense regime

Figure A2.3 shows the onset of the power-law relationship between $\langle N \rangle$ and $1 + t/t_c$ in the cluster-dense regimes. Parallel trends with a constant exponent z of about 1.5 are observed for DLCA systems starting out with different values of f_{vm}. A Rigorous treatment requires parameterizing the prefactor b in Eq. (A2.10) as a function of f_{vm}. We, however, use a constant $b = 0.2$ so as to reach a simpler final expression of Eq. (4.10) in Chapter 4.

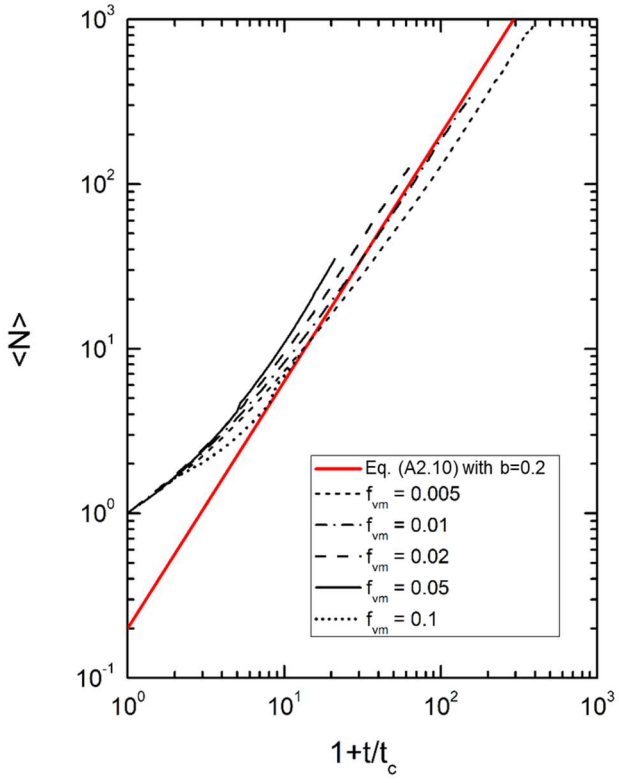

Figure A2.3. Increase in <*N*> as a function of 1 + *t*/t_c for the aggregates in DLCA systems during the time interval between the begin of aggregation and the IGP.

A2.7 Discussions on scale-dependent parameters

In this section, we show that n_{tot} and t_{FGS} are scale-dependent variables and derive the scaling relationships that connects their values with system size V.

Given the conservation of monomers (Sorensen and Chakrabarti 2011), one could assume $n_{tot} \approx n_{tot,0}/\langle N \rangle$. At IGP, such relationship yields to:

$$n_{tot,IGP} \approx n_{tot,0}/N_{IGP} \tag{A2.13}$$

Substitute N_{IGP} using Eq. (A2.3), and assume $D_f = 1.8$:

$$n_{tot,IGP} \approx n_{tot,0} f_{vm}^{1.5} \tag{A2.14}$$

The power-law relation $\frac{n_{tot}}{n_{tot,IGP}} = 2^{z_{FGS}} \left(1 + \frac{t}{t_{IGP}}\right)^{-z_{FGS}}$ (which is Eq. (4.7) in Chapter 4) provides:

$$n_{tot} = n_{tot,IGP} \left(1 + \frac{t}{t_{IGP}}\right)^{-z_{FGS}} \tag{A2.15}$$

Substitute $n_{tot,IGP}$ with Eq. (A2.14) and then substitute t/t_{IGP} with $\frac{t_{IGP}}{t_s} = \frac{3}{16\pi} f_{vm}^{-2.5}$ (which is Eq. (4.11) in Chapter 4), the Eq. (A2.15) yields to:

$$n_{tot} \approx n_{tot,0} f_{vm}^{1.5} \left(1 + \frac{16\pi}{3} \frac{t}{t_s} f_{vm}^{2.5}\right)^{-z_{FGS}} \tag{A2.16}$$

Towards the late-stage, that is $t \gg t_{IGP}$, Eq. (A2.16) can be simplified as following:

$$n_{tot} \approx n_{tot,0} f_{vm}^{1.5-2.5z_{FGS}} t^{-z_{FGS}} \tag{A2.17}$$

Substitute the $n_{tot,0}$ using $f_{vm} = \frac{4}{3}\pi a^3 \frac{n_{tot,0}}{V}$ (which is Eq. (4.1) in Chapter 4), and get:

$$n_{tot} \approx V f_{vm}^{2.5(1-z_{FGS})} t^{-Z_{FGS}} \tag{A2.18}$$

At FGS, $n_{tot} = 1$ and $t = t_{FGS}$, and Eq. (A2.18) gives:

$$t_{FGS} \approx V^{1/Z_{FGS}} f_{vm}^{2.5(1-z_{FGS})/Z_{FGS}} \tag{A2.19}$$

A2.8 References

Oh, C., and Sorensen, C. M. (1997) Light Scattering Study of Fractal Cluster Aggregation Near the Free Molecular Regime. *J. Aerosol Sci.*, 28:937–957.

Sorensen, C, M., and Chakrabarti, A. (2011) The Sol to Gel Transition in Irreversible Particulate Systems. *Soft Matter*, 7:2284–2296.

Appendix III. Supporting Materials for Chapter 5

A3.1 Inference of monomer radius and material density of the nascent soot aggregates from their mass-mobility data published in Cross et al. (2010).

The monomer radius (a), material density (ρ) were inferred from the datapoints in Figure 6 of Reference (Cross et al. 2016). The first data point (in Figure 6 of Cross et al. 2016) at d_m = ca. 32 nm and M = ca. 0.03 fg was inferred to be representing a nascent soot monomer, considering the magnitude of d_m. We assume the monomer to be spherical shape and the d_m can be regarded to be the geometric diameter of the sphere because the particle is within the free molecular flow regime (Sorensen 2011). The material density ρ can be inferred using the equation $\rho = \frac{M}{1/6 \cdot \pi d_m^3}$, which yields ρ = 1812 kg/m^3. The value of ρ matches the generally accepted value for nascent soot particle, 1.8 g/cm^3, which confirmed that the first data point in Figure 6 of Cross et al. 2016 indeed represents monomer. This is because the density expression $\rho = \frac{M}{1/6 \cdot \pi d_m^3}$ only holds for monomers which are of Euclidean geometry and non-porous. The monomer a was regarded as half of monomer d_m and thus a = 16 nm.

The Table A3.1 label the M and d_m data extracted from Figure 6 of Cross et al. (2010). Number of constituent monomer in aggregates N was estimated from the mass ratio of aggregate and monomer. The Radius of gyration R_g was next estimated using the empirical relationship $\frac{d_m}{2R_g} = 1.29N^{-0.1}$ proposed by Sorensen (2011). Note that the value of N calculated from mass

ratio is non-integer because of the uncertainty in the value of mass measured using the centrifugal particle mass analyzer. We used the non-integer N for the estimation of aggregate R_g.

Table A3.1 The fractal parameters of nascent soot aggregates inferred from the mass-mobility data published in Cross et al. (2010)

d_m (nm)	M (fg)	N	R_g (nm)	R_g/a
31.538	0.030	1.000	NA	NA
49.851	0.090	3.039	21.594	1.369
51.979	0.090	3.014	22.497	1.427
51.576	0.100	3.360	22.566	1.431
53.219	0.100	3.360	23.285	1.477
55.936	0.131	4.390	25.137	1.594
66.301	0.180	6.031	30.757	1.950
69.315	0.190	6.395	32.344	2.051
80.035	0.231	7.750	38.071	2.414
89.573	0.350	11.770	44.426	2.817
100.230	0.391	13.121	50.254	3.187
100.239	0.462	15.508	51.106	3.241
99.722	0.510	17.144	51.355	3.257
115.144	0.603	20.264	60.297	3.824
127.183	0.801	26.923	68.521	4.345
132.621	0.901	30.265	72.292	4.584
133.317	0.916	30.775	72.793	4.616

A3.2 Empirical relationship between the number of monomers in the three-dimensional gel particles and the number of monomers in their projections.

We sampled 7,563 individual aggregates generated using the dense DLCA model and their two-dimensional (2-d) projected images were taken from random orientations. The number of monomers seen in the projection (N_{2d}) of these gel particles were obtained via dividing their projected area by monomer cross-section area. Figure A3.1 shows the log-log plot of total number of monomers in 3-d (N) versus N_{2d} for these numerically generated gels. The empirical relationship $N = 0.93N_{2d}^{1.16}$ (black line in Figure A3.1) was obtained by fitting the data according to a power-law.

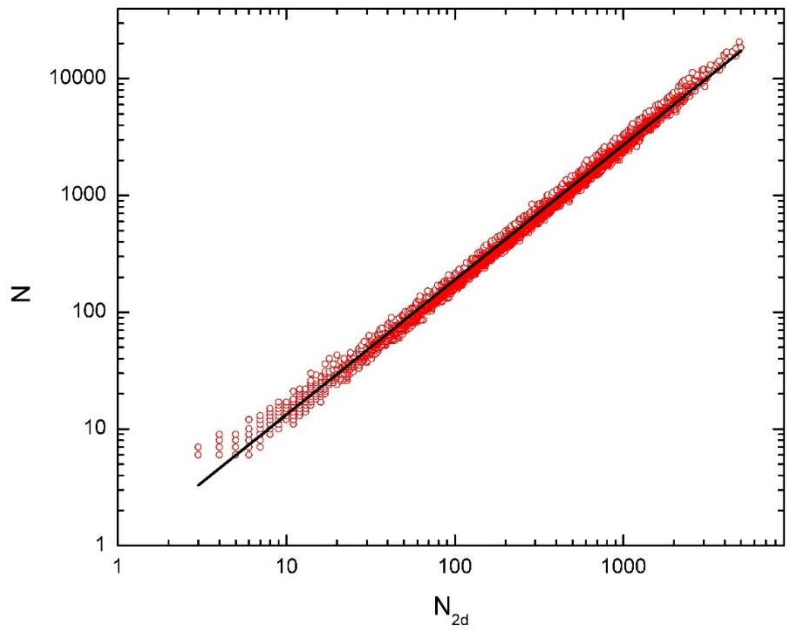

Figure A3.1. Empirical relationship between N and N_{2d} for gels simulated using the dense DLCA model. Solid line follows $N = 0.93N_{2d}^{1.16}$.

A3.3 Comparison between 2-dimensional radius of gyration and 3-dimensional radius of gyration for gel particles in cluster-dense regime.

We sampled 7,563 individual aggregates generated using the dense DLCA model. The ratio of their 2-d radius of gyration ($R_{g,2d}$) to 3-d radius of gyration ($R_{g,3d}$) are plotted in Fig. A3.2 with N across three order of magnitudes. The average value of $R_{g,2d}/R_{g,3d}$ is 0.98 and one standard deviation is 0.03.

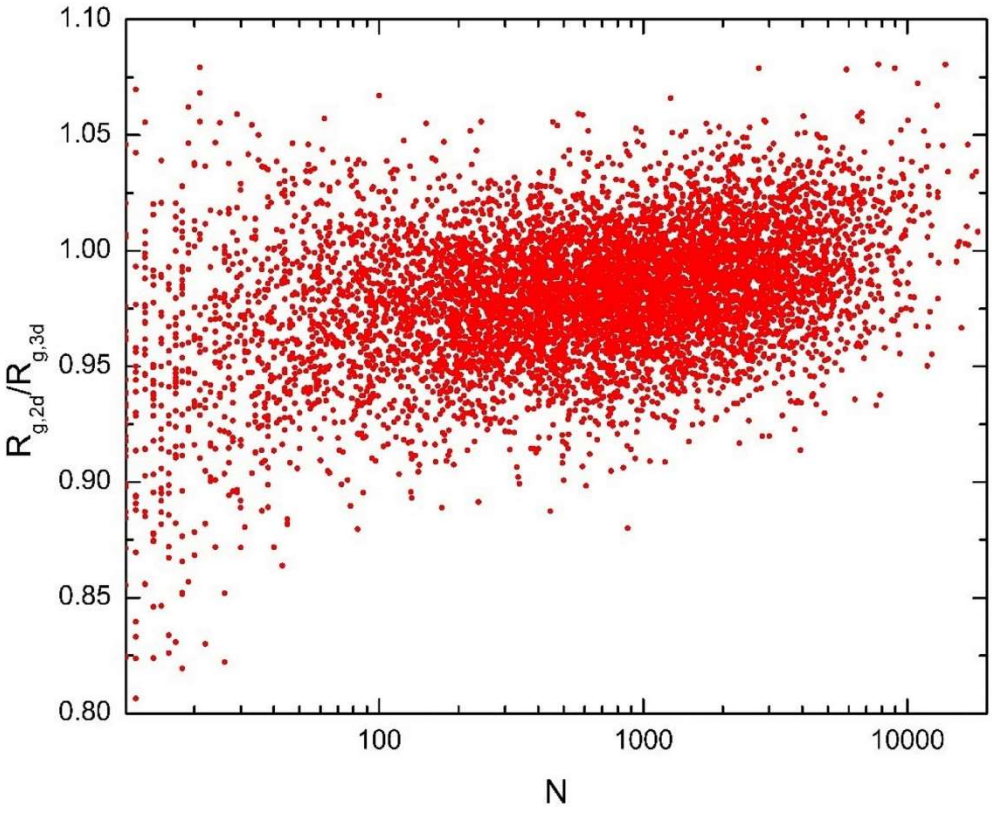

Figure A3.2. Ratio of $R_{g,2d}$ to $R_{g,3d}$ for aggregates simulated using dense DLCA model.

A3.4 Motion of the near millimeter-size soot particles in our ethylene buoyancy-opposed flame

Figure A3.3 shows the trajectories of nine millimeter-size soot particles in the body of our ethylene buoyancy-opposed flame. The Cartesian coordinates were set as following: the origin sits at the center of the burner mouth. The *xy* plane is horizontally set and the *z* axis measures the vertical distance to the surface where the burner mouth resides. The cylindrical coordinates are set up as following: the origin is identical to that of the Cartesian coordinates. $r\theta$ is horizontally set with θ measuring the angle along counterclockwise direction. One could observe that the motion of the particles is restricted to a 3-d annular region close to the flame front. The annular thickness of about 5mm can be roughly estimated from the right panel trajectory diagram of Figure A3.3. This thickness is slightly larger than the size of these particles, which dictates that the binary collisions will take place predominately along the *z* and θ direction. The collisions along *r* direction are still possible albeit with smaller probability. This quasi three dimensional collision arrangement may have led to a value of D_f of these particles to be smaller than that of particles growing via 3-d cluster-cluster aggregation ($D_f \approx 1.8$ - 1.9), but still greater than $D_f \approx 1.4$ value resulting from 2-d cluster-cluster aggregation.

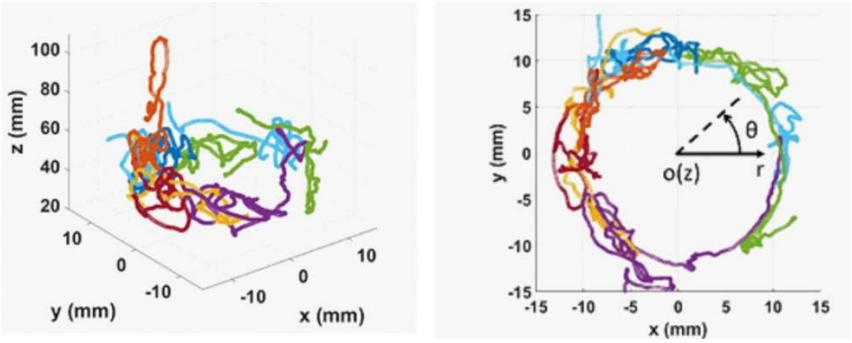

Figure A3.3. Trajectories of 9 particles in the body of our ethylene buoyancy-opposed flame.

A3.5 References

Cross, E. S., et al. (2010). Soot Particle Studies—Instrument Inter-Comparison—Project Overview. *Aerosol Sci. Technol*., 44:592-611.

Sorensen, C. M. (2011). The Mobility of Fractal Aggregates: A Review. *Aerosol Sci. Technol.*, 45:765-779.

Appendix IV. Curriculum Vitae

EDUCATION

- **Washington University in St. Louis,** St. Louis, MO, USA 2014-2019
  - Ph.D. in Energy, Environmental and Chemical Engineering
  - Dissertation: "Contemporary Problems in Aerosol Aggregation and Gelation"
  - Advisor and Chair of Committee: Rajan K. Chakrabarty
- **Washington University in St. Louis,** St. Louis, MO, USA 2013-2014
  - Master Program in Energy, Environmental and Chemical Engineering
- **Dalian University of Technology,** China 2009-2013
  - B.S. in Energy and Power Engineering
  - Thesis: "*In situ* Measurement of the Heat Conductivity of Natural Gas Hydrate during its Thermal Decomposition"
  - Advisor: Yongchen Song

AWARD AND FELLOWSHIP

- **The Forrest and Patricia McGrath Scholarship,** Washington University in St. Louis 2014-2015
- **Travel Grant,** The 34th American Association for Aerosol Research Annual Conference Oct. 2015

PEER-REVIEWED PUBLICATIONS

8. **Liu, P.,** Heinson, W. R., Sorensen, C. M., Chakrabarty R. K. (2019). Kinetics of Sol-to-Gel Transition in Irreversible Particulate Systems. **J. Colloid Interface Sci.,** 550, 57-63.

7. Heinson, W. R., Heinson, Y. W., **Liu, P.,** Chakrabarty, R. K., (2018) Breakdown of Fractal Dimension Invariance in High Monomer-Volume-Fraction Aerosol Gels. **Aerosol Sci. Technol.,** 52, 953-956.

6. **Liu, P.,** Heinson, W. R., Sumlin, B. J., Shen, K.-Y. Chakrabarty, R. K., (2018) Establishing the Kinetics of Ballistic-to-Diffusive Transition using Directional Statistics. **Phys. Rev. E,** 97, 042102.

5. **Liu, P.,** Heinson, W. R., Chakrabarty R. K., (2017) Fractal Scaling of Soot Packing Density across Five Size Decades. **Aerosol Sci. Technol.,** 51, 879-886.

4. Heinson, W. R., **Liu, P.,** Chakrabarty R. K., (2017) Fractal Scaling of Coated Soot Aggregates. **Aerosol Sci. Technol.,** 51, 12-19.

3. **Liu, P.,** Chakrabarty, R. K., (2016) Sensitivity Analysis of Aggregate Morphology on Mass-Mobility Relationship and Improved Parameterizations. **Aerosol Sci. Technol.,** 50, 63-70.

2. **Liu, P.,** Arnold, I. J., Wang, Y., Yu, Y., Fang, J., Biswas, P., Chakrabarty, R. K., (2015) Synthesis of Titanium Dioxide Aerosol Gels in a Buoyancy-Opposed Flame Reactor. **Aerosol Sci. Technol.,** 49, 1232-1241.

1. Wang, Y., **Liu, P.,** Fang, J., Wang, W., Biswas, P., (2015) Kinetics of Sub-2 nm TiO_2

Particle Formation in an Aerosol Reactor during Thermal Decomposition of Titanium Tetraisopropoxide. **J. Nanopart. Res.,** 17, 147.

SELECTED PRESENTATIONS

5. **Liu, P.,** Heinson, W. R., Chakrabarty R. K., September 2018. "The Kinetics of Aerosol Gelation." Saint Louis, Missouri, 10th International Aerosol Conference.

4. **Liu, P.,** Heinson, W. R., Sumlin, B. J., Chakrabarty R. K., October 2017. "Experimental Observation of Ballistic to Brownian Transition in an Aerosol System" Raleigh, North Carolina, American Association for Aerosol Research 36th Annual Conference.

3. **Liu, P.,** Heinson, W. R., Chakrabarty, R. K. December 2016., "Fractal Scaling of Soot Packing Density across Five Size Decades" Boston, Massachusetts, 2016 Material Research Society Fall Meeting.

2. **Liu, P.,** Chakrabarty R. K., October 2015. "Sensitivity Analysis of Aggregate Morphology on Mass-Mobility Relationship and Improved Parametrizations" Minneapolis, Minnesota, American Association for Aerosol Research 34th Annual Conference.

1. **Liu, P.,** Arnold, I. J., Wang, Y., Yu, Y., Fang, J., Biswas, P., Chakrabarty, R. K., October 2015. "Synthesis of Titanium Dioxide Aerosol Gels in a Buoyancy-Opposed Flame Reactor". Minneapolis, Minnesota, American Association for Aerosol Research 34th Annual Conference

TEACHING AND MENTORING EXPERIENCE

- **Student mentor,** Department of Energy, Environmental and Chemical Engineering, Washington University in St. Louis. 2015-2019
    - Mentored five rotating Ph.D. students (Nishit Shetty, Sukrant Dhawan, Bongjin Seo, Chun-Ying Chao, Erfan Asadipour)
    - Three master students (Yang Yu, Ted Cohen, Poom Sittisomwong)
    - Three undergraduate summer interns (Saif Rahaman, Gowtham Kuntumalla, Alice Hsu)
- **Teaching assistant** for Graduate level courses: *Transport Phenomenon*, *Advanced Topics in Aerosol Science and Technology*, and *Environmental Organic Chemistry.* 2015-2019

PROFESSIONAL SERVICES

- **Chair,** Aerosol Modeling Session, the 10th International Aerosol Conference. Sept. 2018
- **Student committee member,** Faculty Search in 2018, Department of Energy, Environmental and Chemical Engineering, Washington University in St. Louis. Jan. 2018
    - Interviewed eight faculty candidates and provided reports to the department
- **Reviewer,** *Material Research Society Advances* Dec. 2016

- **Organizer,** Poster Sessions, the 1st and 2nd Center for Aerosol Science and Engineering Workshop. 2015-2016
- **Student Assistant,** the 34th and 35th American Association for Aerosol Research Annual Conference 2015-2016

MEDIA APPEARANCE

- **Cosmos Magazine,** Mathematics Section, June 14, 2018 issue June 2018